The Propagation Characteristics of the Plate Modes of

Acoustic Emission Waves in Thin Aluminum Plates and Thin

Graphite/Epoxy Composite Plates and Tubes

by

William H. Prosser

A dissertation submitted to The Johns Hopkins University

in conformity with the requirements for the degree of

Doctor of Philosophy

Baltimore, Maryland

1991

Abstract

   Acoustic emission was interpreted as modes of vibration in finite aluminum and graphite/epoxy plates. The 'thin plate' case of classical plate theory was used to predict dispersion curves for the two fundamental modes described by the theory and to calculate the shapes of flexural waveforms produced by a vertical step function loading. There was good agreement between the theoretical and experimental results for the aluminum. Composite materials required the use of a higher order plate theory (Reissner-Mindlin) combined with lamination theory in order to get good agreement with the measured velocities. Plate modes were shown to be useful for determining the direction of motion of a source. Thus, with a knowledge of the material, it may be possible to ascertain the type of the source. For example, particle impact on a plate could be distinguished from a crack growing in the plate.

   A high fidelity transducer was needed to distinguish the plate modes. After evaluating several types of transducers, a broadband ultrasonic transducer was found which satisfied the fidelity requirement and had adequate sensitivity over the 0.1 to 1 MHz range. The waveforms were digitized with a 5 MHz transient recorder. The dispersion curves were determined from the phase spectra of the time dependent waveforms.

   The aluminum plates were loaded by breaking a 0.5 mm. pencil lead against the surface of the plate. By machining slots at various angles to the plane of a plate, the direction in which the force acted was varied. Changing the direction of the source motion produced regular variations in the measured waveforms. Four composite plates with different laminate stacking sequences were studied. To demonstrate applicability beyond simple plates, waveforms produced by lead breaks on a

thin-walled composite tube were also shown to be interpretable as plate
modes. The tube design was based on the type of struts proposed for
Space Station Freedom's trussed structures.

Acknowledgments

The author would like to thank a number of people without whom this work would not have been possible. First and foremost, gratitude is due my wife, Karen, for her love, support, patience, and understanding throughout this endeavor. Our parents and families also provided support and encouragement that was greatly appreciated.

I am grateful to my thesis advisor in the Materials Science and Engineering Department at Johns Hopkins University, Dr. Robert E. Green, Jr. The knowledge of the mechanics of materials and the propagation of elastic waves which he imparted to me during my earlier years at Hopkins served me well throughout the course of this research. His allowance of my participation in the nonresident student research program to carry out the research at NASA Langley Research Center and his assistance in the logistics of this were of tremendous value. Also at Johns Hopkins, Dr. Jim Wagner and his graduate students, Jim Spicer and John Deaton, were of great assistance in providing the optical interferometer and assisting with the measurements presented in the transducer evaluation section. The remaining faculty within this department also contributed greatly to my education as well as provided friendship and support. Thanks is also due to a number of graduate students and former students including Paul Kelley, Lou Phillips, Joe Krynicki, and those listed previously, who provided friendship which made my years at Hopkins most enjoyable.

In the Nondestructive Evaluation Science Branch at NASA Langley Research Center, where most of this research was performed, Dr. Joe Heyman and Dr. Eric Madaras are acknowledged. They provided both technical and financial support and allowed me the freedom needed to pursue this

work. Also, John Dorighi, a visiting summer student from the University of Colorado, provided assistance in the gr/ep tube measurements and in proofreading this thesis. Many other members of the Nondestructive Evaluation Science Branch, too numerous to mention by name, also provided technical and moral support during this research.

Last, but certainly not least, is the acknowledgment of Dr. Mike Gorman of the Department of Aeronautics of the Naval Postgraduate School. As my De Facto advisor during our collaborative research efforts, he provided the initial ideas and motivation for this work and has provided brilliant technical insights throughout its progress. His patience and support through almost daily coast to coast phone conversations were invaluable. His friendship, company, and golf tips during our several meetings made this research most pleasurable as well as lowered my handicap. The collaborative assistance of Steve Ziola, a graduate student of Dr. Gorman, is also acknowledged.

Table of Contents

List of Figures

List of Tables

I. Introduction

Acoustic emission (AE) is defined as the release of transient elastic waves in solids as a result of rapid localized redistributions of stresses which accompany the operation of damage mechanisms. Examples of events which cause AE include micro-cracking in metals and matrix cracking and fiber breakage in composites. These AE sources can be precursors to the ultimate failure of the material. Since the waveforms contain information about the source such as its location, orientation, type, and size, it is desirable to capture these waves. If such information can be obtained by analysis of the waveforms, it can be used to determine the type and amount of damage to the structure. This can be used in models which predict the remaining life of a structure.

According to Liptai et al.[1], the earliest use of acoustic emission analysis occurred in the study of seismology. They report that the first clearly documented investigation of acoustic emission in structural materials was performed by Joseph Kaiser in the 1950's. He studied emission released during loading of polycrystalline metal specimens. It was pointed out by Kaiser that the emission is affected by the previous load history of the specimen in metals. A previously loaded metal specimen did not release AE until the load reached a level higher than the previous maximum load. This effect is now known as the Kaiser Effect and has been used to determine the previous maximum load on a metal structure.

The potential usefulness of AE for structural monitoring was soon recognized. However, the interpretation of AE signals has proven quite difficult because of the complexity of propagation of elastic waves through solids. As discussed by Green [2], in an infinite,

elastic, anisotropic solid, three modes of propagation are allowed along any given direction. One of these will be a longitudinal or quasi-longitudinal mode while the others will be transverse or quasi-transverse modes. These modes will propagate with different velocities and interfere with one another. If boundaries or surfaces on the solid are now considered, the complexity increases. As pointed out by Auld [3], when one of these modes interacts with a boundary, reflected and transmitted waves of all three modes may be generated. Additionally, in bounded media, there are additional modes of propagation available such as surface, plate, or interface waves. Furthermore, the frequency response of the transducer and detection electronics will also alter the acoustic emission waveform.

Another difficulty in AE is the transient and sporadic nature of the emissions. Before digitizers or transient recorders were commonly available, it was difficult to capture individual AE events. Even today, the memory requirements necessary to capture the thousands of events that can occur in a single test are a major obstacle.

In order to avoid these problems, most AE testing does not capture entire waveforms and attempt to directly interpret them to obtain source information. Instead, features of the signals, the so called AE parameters, are measured by analog circuitry which can quickly process the signals. These parameters are plotted against other parameters of the test such as the load, strain, or temperature of the test specimen. After repeated tests on identical specimens, empirical inferences can be made about the sources of the emissions. These inferences allow future AE data to be classified, and then the type and amount of damage in a specimen to be predicted. Typical features or parameters of the AE waveforms used for this pur-

pose include the peak amplitude, rise time, duration, energy, and counts above threshold. A typical AE waveform along with an explanation of these parameters is presented in Figure 1.1.

Peak Amplitude - Maximum voltage level of the AE event.

Duration - The length of time that the event remains above the threshold once detected.

Counts - The number of times that the event crosses the threshold of the system.

Energy - The area under the AE envelope.

Rise Time - The time it takes an AE event to reach its peak amplitude, once detected.
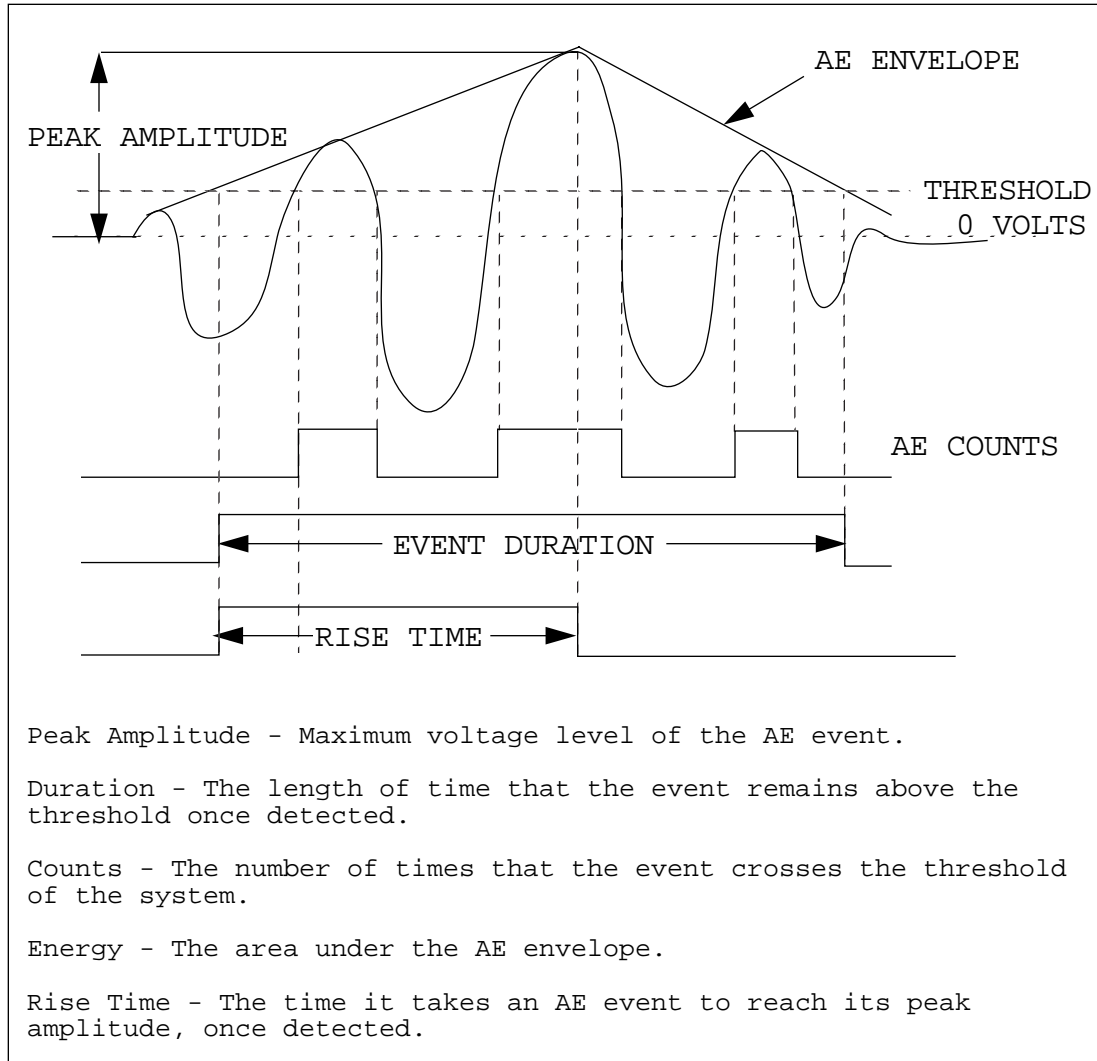
Figure 1.1   AE event definitions.

This approach to interpreting AE data, which will be referred to as conventional AE, has been used successfully in a number of applications. These include structural monitoring, materials testing, and process monitoring. These applications have been in a wide variety of industries including aerospace, nuclear power, and materials

processing and testing. The first documented practical application appears to be that of monitoring the proof testing of Polaris solid rocket motor casings by Green et al. [4] in 1964. Other examples of the use of AE for structural monitoring include the testing of a reactor pressure vessel by Votava and Jax [5] and the detection of failure modes in high pressure storage tanks by Le Floc'h [6]. In the area of process monitoring, Bentley et al. [7] applied acoustic emission to welding process monitoring. Machining processes have been monitored with AE by Lan and Dornfeld [8]. A review of a number of applications of AE is presented by Spanner [9].

The use of conventional AE monitoring during materials testing has been quite extensive, especially for composite materials. Among other things, it has been used to approximately locate damage sites and give real time information on the initiation and progression of damage. This has allowed information to be obtained on the operation of various failure mechanisms under different testing conditions.

One interesting feature of AE in composites is that the Kaiser Effect usually does not hold. Significant AE begins to occur at load levels lower than the previous load maximum in repeated loading tests. The ratio of the load at which the emission begins to the previous maximum load was termed the Felicity Ratio by Fowler and Gray [10]. This effect has been investigated by a number of authors.

As for other work on the use of AE in composite materials, Hamstad [11] has presented an extensive review. In this, it was noted that, at the time, over 500 papers and reports on AE had been published since 1970.

Thus, the conventional approach to interpretation of AE data has seen a number of successful applications. It is, however, not without

its limitations. The most severe of these is that the empirical in-ferences relating the measured AE parameters to the sources are strongly dependent on the geometry and material of the specimen. This is because of the effects that these parameters have on the detected waveforms and thus the measured AE parameters. The relation-ship between, for example, the number of AE counts and the applied load on a steel pressure vessel of a particular size will be entirely different on a pressure vessel of a different size or geometry or on a vessel made of a composite material. Hill and El-Dardiry [12] discussed and demonstrated the effect of specimen geometry on AE pa-rameters. Therefore, the application of the technique has been gener-ally limited to situations where large numbers of identical specimens are available to establish the relationships and large numbers of identical specimens are to be monitored using those relationships. This is why the monitoring of pressure vessels with AE has been such a successful application.

A similar limitation of conventional AE is its sensitivity to the choice of transducer and detection electronics used for signal measurement. If the location of the transducer on the specimen, the bonding of the transducer to the specimen, or the resonant frequency of the transducer are varied, the detected waveforms and thus the measured AE parameters can be entirely different. Changes in the detection electronics such as the amount of signal amplification or filtering bandwidth also produce changes in the mea-sured parameters. Likewise, the measured AE patterns are sensitive to variables such as the detection threshold voltage level. Also, as noted earlier, the release of AE is dependent on the previous load history of the specimen.

Therefore, the conventional approach to AE analysis is affected by a number of factors which severely limit the utilization of the technique. Furthermore, erroneous conclusions can be drawn if strict attention is not paid to all of these factors. These facts have been the motivation for research into the generation, propagation, detection, and interpretation of AE waves. The knowledge gained from this research can lead to wider and more successful applications of the AE technique.

One early approach to obtaining more information about emission sources was to analyze the detected signals in the frequency domain by spectral analysis. This was based on the belief that different source mechanisms should have different source time functions which would, therefore, yield waveforms with different frequency spectra. The early work by Kaiser, discussed by Liptai et al. [1], pointed out that the predominant frequency of AE signals in tensile tests of aluminum and steel specimens shifted as the load increased. Frequency analysis has been explored by a number of other researchers, however, frequency analysis of AE waveforms to differentiate source mechanisms has had very limited success. The primary reason is because the detected signals are colored by the frequency dependent attenuation of the material, the geometry of the specimen, and the frequency response of the transducer and detection electronics. The spectrum of the detected wave will be entirely different from the spectrum of the AE source function and in only a very few cases have true AE source spectra been obtained. However, spectral analysis of signals has been of value in selecting instrumentation to optimize detectability and in isolating background noise (See the review by Eitzen et al. [13] and references contained therein).

In order to circumvent affects of the changes in the waveforms by the material, transducer, and electronics, research has been undertaken in an area commonly referred to as quantitative AE. Much of the research carried out in this area was presented by Eitzen et al. [13] and references contained therein. This research has sought to characterize the source function that created the AE wave which was then altered by the effects of propagation and detection. To accomplish this goal, a transfer function formalism has been used whereby it was assumed that the AE waveform was altered by two effects. The first effect was that caused by the geometry and material in the propagation of the signal from the source to the detection location. The second effect accounts for the transducer and detection electronics. These can be considered as linear transfer functions applied to the original signal. Once these transfer functions are known, the source function can be obtained by a deconvolution procedure which can be accomplished as a division in the frequency domain.

The transfer function for the transducer and electronics is essentially an absolute calibration. This provides the relationship between the input mechanical signal and the resulting output voltage at all frequencies. The foundations for transducer calibration were presented by Breckenridge et al. [14]. This task has been successfully accomplished by researchers at NIST (formerly NBS) and an excellent review of the work is presented by Eitzen et al. [13] and references contained therein. In this work, a waveform was obtained with the sensor to be calibrated from a simulated AE event. This simulated event was caused by a pencil lead break (Hsu-Neilsen source) or a glass capillary break on the surface of a large steel block. The

dimensions of this block were large enough so that the waves could be approximated as propagating in a semi-infinite half space. That is, it was designed so that no reflections from lateral boundaries would arrive at the receiving transducer within the time that the wave was detected. This waveform was then calibrated against one of two other signals. The first was that of a signal obtained by a ca-pacitive transducer positioned at an identical distance from the source. This capacitive sensor was absolutely calibrated. This al-lowed absolute calibration of the unknown sensor.

The second signal used for calibration was that of a theoretically predicted signal. The theory used was that for a semi-infinite half space presented by Lamb [15] and Pekeris [16], which was originally developed for the understanding of seismic wave propagation. The in-put forcing function was assumed to be a step unloading of the sur-face. The magnitude of this input force was measured by sensors attached to the lead or capillary breaking mechanism. Agreement in the results of calibrating against the two different standards was within a few percent and the accuracy of the calibration was estimat-ed at about five percent.

Although the use of calibration and deconvolution offers a signif-icant improvement in the fidelity of the detected signal, there is a limitation. In frequency ranges far away from the resonant band-width of the transducer, there may be zero or near zero sensitivity. In these ranges, signal content will be lost which can-not be recovered by calibration and deconvolution. Thus, in addition to calibration, research efforts have also been spent on de-veloping new transducers that offer broader band frequency responses. Sometimes capacitive sensors have been used, but they lack in sensi-

tivity and can be used only on conductive materials. Proctor [17] has developed an improved piezoelectric AE transducer that has flat frequency response over the 50 kHz to 1 MHz bandwidth. This sensor consists of a conical piezoelectric element mounted on a large cylindrical brass backing. The brass backing eliminates reflections and ringing within the sensor element. More recently, Proctor [18] has developed a high fidelity piezoelectric tangential displacement transducer for acoustic emission. This sensor measures the tangential surface displacement component instead of the component normal to the surface measured by most sensors.

The effect of propagation through the material on the AE signal has been studied using a Green's function approach. A Green's function predicts the displacement of a body resulting from a point source, impulse (delta function) loading at some point in the body. In actuality, a Green's tensor is needed in the most general case due to the vector nature of the displacement and of the applied force. In the case of the application of force couples, spatial derivatives of the Green's tensor are needed.

Assuming linear elasticity so that the law of superposition applies, any source function can be built up from the superposition of delta functions of varying amplitudes. Thus, the Green's tensor can be used to deconvolve the geometrical effects of propagation from the detected signal. The Green's tensor has been calculated for an isotropic, semi-infinite, half space from theory. It has also been calculated for a thick isotropic plate of infinite lateral dimensions using generalized ray theory as demonstrated by Pao et al. [19]. Hsu [20] has developed a computer algorithm which accomplishes these calculations. Generalized ray theory predicts the displacements

by calculating all rays of propagation including those reflected and mode converted which will reach the detection point up to a certain point in time. Thus, the solution by generalized ray theory is valid only for a limited period of time. More complicated geometries cannot be treated directly by theory. However, finite difference methods have been used by Fukunaga and Kishi [21] to determine the Green's function of a compact tension specimen.

This Green's function approach together with calibrated transducer deconvolution has been applied successfully in laboratory experiments to determine the AE source function by a number of authors. An excellent review of the earlier work in this area is presented by Eitzen et al. [13] and references contained therein. Later research in this area includes that of Scruby et al. [22] who characterized acoustic emission from fatigue crack extension and Kim and Sachse [23] who characterized an acoustic emission source from a thermal crack in glass. Others contributing in this area include Enoki and Kishi [24], Ohtsu and Ono [25], and Wadley and Scruby [26] to name but a few.

Most of the previously mentioned work on AE source characterization has neglected the distortion of the elastic wave caused by frequency dependent attenuation in the material. C. P. Hsiao [27] has included this effect in his work on the propagation of acoustic emission signals in polymeric media. Yu and Clapp [28] investigated the effect of frequency dependent attenuation caused by grain scattering on signals in polycrystalline metals.

This research on determining the source function of AE signals has greatly increased the understanding of the generation, propagation, and detection of AE waves. For a number of reasons, however, this

quantitative approach has been limited to laboratory research and has not been useful for applied AE monitoring. One reason is that of the complexity of the analysis and the resulting need for large amounts of computer time to analyze even a single event. Typical AE tests on composites may result in tens of thousands of AE signals. The calculation of a single Green's functions for a thick plate may require several hours of computer time. This makes the quantitative analysis of the large number of events impractical. This problem, however, may be overcome in the future with faster and more powerful computers.

The complexity of the theory also currently limits applications to the geometries of thick plates of infinite lateral extent or semi-infinite half spaces. Furthermore, even in these simple geometries, solutions only have been obtained for isotropic materials. Thus, analysis of AE signals in composite materials in this manner is not yet possible. Also, the deconvolution procedures used to remove the artifacts of the transducer and propagation are sensitive to noise and the need for absolutely calibrated wide band transducers with good sensitivity has been a drawback.

Thus, new approaches to interpreting AE signals to determine source information are being sought. One such approach which has been under study recently involves interpreting the signal in thin plate structures in terms of its plate mode characteristics. Many practical structures for AE monitoring have plate or shell characteristics wherein one dimension is much smaller than the other two. Examples of this include aircraft and spacecraft external skins, pressure vessels, and piping. In materials of such geometry, the elastic waves propagate in modes whose propagation characteristics are dependent on

the plate thickness and boundary conditions in addition to the usual dependence on the elastic properties and density of the material. These modes are commonly called Lamb waves because of the early studies by Lamb [29] into their propagation. Rayleigh [30] was also involved in the early research of these waves.

These waves can be divided into three types. One type causes out-of-plane plate deformations which are symmetric about the midplane of the plate and are called symmetric modes. The other has out-of-plane plate deformations which are antisymmetric about the plate midplane. These are called antisymmetric modes. The third mode has transverse particle vibrations which are horizontal to the plane of the plate and thus are called shear horizontal or SH modes. It was demonstrated theoretically that all three types of these waves have an infinite number of modes. These modes are dispersive which means that the velocity of the mode is dependent on the frequency of the wave. Graff's book [31] contains a large number of the references to the literature on Lamb wave propagation.

As discussed in Graff's book [31], approximations can be made to derive a set of equations of motion which describe the propagation of the lowest order mode of each Lamb wave type at low frequencies. This theory is known as classical plate theory (CPT) and has been shown to be a valid approximation in the regime where the wavelength is large with respect to the plate thickness. The waves predicted by this theory are referred to as plate waves. The symmetric plate wave is often called the extensional wave while the antisymmetric plate wave is called the flexural wave. The horizontal shear wave is called the SH plate wave. This theory will be discussed in much greater detail in a later section.

Although many practical structures monitored by AE have plate or shell geometries in which Lamb modes may propagate, little research has been carried out on the interpretation of transient AE waves as combinations of these modes. Most of the previous research on Lamb waves has been for one of two applications. The first has been for the understanding of low frequency structural vibrations. The second has been related to the generation and propagation of high frequency ultrasonic waves. This includes the vibration of piezoelectric crystal transducers and the propagation of sinusoidal ultrasonic waves. One exception to this was a study by Pollock [32] who has shown the existence of a number of Lamb modes in AE signals in thick walled pressure vessels. He measured the velocity of several modes and found them to be in agreement with predictions from Lamb theory.

Other work not related to AE, but concerning the propagation of transient waves in plates, were studies by Press and Oliver [33] and Medick [34]. In the former, flexural plate waves resulting from a transient spark source near a thin aluminum plate were detected and analyzed. In Medick's work, flexural waves in plates also were detected. The source was the impact of a rifle bullet. Medick compared his results with theoretical predictions from CPT. He demonstrated good agreement between theory and experiment.

In more recent research, Gorman [35] has focussed on interpreting AE signals in thin plates in terms of their plate wave content. Several interesting points were demonstrated in this work. First, in the range of frequencies considered by most AE experiments (20 kHz to 1 MHz), the in-plane shear mode was not observed and the other two modes dominated the detected signals.

These signals were generated by pencil lead breaks (Hsu-Neilsen sources). The most interesting feature of this work, however, was that the amplitudes of the two modes were dependent on the source orientation. Lead break sources on the surface of the plate created a much larger flexural mode while those on the edge of the plate created a much larger extensional mode. This suggested that the relative amplitudes of these two modes contain information about the source orientation.

Additionally, Gorman pointed out how the different velocities of the extensional and flexural modes could cause errors in the location of the source of emission. Most location techniques used in conventional AE assume a single propagation velocity value. In the case of multiple velocities, these techniques may locate erroneously depending on which mode triggers the timing circuitry used for location. One final interesting feature of this work was the use of a conventional high frequency (5 MHz) ultrasonic transducer for the detection of the AE signals in the low kHz to 1 MHz frequency bandwidth. This transducer seemed to provide a much flatter frequency response than a conventional resonant sensor. However, this response was not well characterized.

Gorman and Ziola [36] followed this work by capturing and analyzing AE signals from a real AE source in composite plates. The source mechanism was that of transverse matrix cracking (TMC) which is created in cross ply laminates under tensile load. The waveforms consisted of the plate modes (which sometimes are called the lowest order Lamb modes). However, in this case, the extensional mode had a much larger amplitude. This, they concluded, was consistent with the large in-plane motion of TMC sources. Their understanding of

plate mode propagation allowed much more accurate location of the AE sources. They were able to compare their calculated locations favorably with locations determined by ultrasonic measurements made after the test.

The investigation of plate wave AE in thin plates was continued in this research. First because of the need to use a broad band transducer to accurately measure the plate wave displacements, four different types of acoustic sensors were comparatively evaluated to determine the one which offered the best combination of bandwidth and sensitivity properties. The transducers which were examined included a 3.5 MHz broadband ultrasonic transducer (Panametrics) similar to that used by Gorman [35]. In addition, a conventional 150 kHz resonant AE sensor (Physical Acoustics Corporation R15), a conventional broadband AE sensor (Physical Acoustics Corp. S9208), and a pinducer (Valpey-Fisher Co.) were evaluated. All four types were comparatively tested by comparing their outputs when subjected to three different input stimuli. The first input signals were the vibrations of another nominally identical 3.5 MHz ultrasonic transducer driven by constant amplitude, swept-sine tone bursts over the 20 kHz to 1.5 Mhz frequency range. The transducers were coupled to each other in a face-to-face manner. The second input signals were acoustic waves in a thick aluminum plate generated by pencil lead breaks at an equal distance of propagation for all four sensors. These signals were compared with theoretical predictions using the program by Hsu [20]. The third input signal was that of a simulated AE event in a thin aluminum plate caused by a pencil lead break. This was compared with the output of a laser interferometer located at an identical distance from the source. This interferometer was

known to be sensitive to the normal component of the displacement
of the plate surface. In all three experiments, the ultrasonic trans-
ducer demonstrated the flattest frequency response while offering
sensitivity as good as or better than the conventional broad band
AE sensor. Thus it was chosen for use in the remaining plate wave
measurements.

Having chosen and characterized an acoustic transducer, measure-
ments were made of AE signals propagating in thin aluminum plates
caused by simulated AE sources (lead breaks). Two phenomena were in-
vestigated. The first was a more extensive evaluation of the effect
of source orientation on the relative amplitudes of the two plate
modes. Slots were cut into the surface of the plates which allowed
the lead break to be oriented at other angles with respect to the
plate surface. The previous research by Gorman [35] had only consid-
ered sources normal to the surface (90 degrees) and along the edge of
the plate (0 degrees). In this research, signals were captured for
sources at angles of 30 and 60 degrees with respect to the plane of
the plate. Increasing source angles caused larger amplitude
flexural modes while decreasing source angles caused larger amplitude
extensional modes. This provided further evidence that the relative
amplitudes of plate modes contain information about the source orien-
tation.

The second phenomenon investigated in the aluminum plates was
the propagation of the flexural waves. A normal mode approach was
used to solve the classical flexural equation of motion for the
case of a finite plate. This solution was shown to agree with predic-
tions for propagation in an infinite plate obtained by integral
transform techniques up until the time at which reflections begin

to appear. The normal mode approach, however, predicted the reflections of the flexural mode from the boundaries of the plate. Good agreement was exhibited between theory and experimental measurements over the frequency range in which the assumptions used to derive the classical equation remained valid.

The propagation of plate waves was also investigated in several gr/ep composite laminates of different ply layups. In this case, the material was no longer isotropic. The extensional and flexural velocities were measured as a function of frequency for several directions of propagation. Comparison of the measured flexural dispersion with theoretical predictions based on CPT using material properties obtained from the composite manufacturer showed a lack of agreement. It was determined that the effects of shear deformation and rotatory inertia which are neglected in CPT were the cause for the discrepancy. These effects were shown to be much larger in the composite than in the aluminum. A higher order plate theory (HOPT) which includes these effects was used and it yielded much better agreement.

However, a small difference between theory and experiment remained wherein the measured velocities were consistently slightly less than those predicted. This was also true for the extensional velocities which were measured and predicted. This discrepancy was attributed to variability in the actual composite elastic properties from those obtained by the manufacturer.

An attempt to predict the shape of the flexural mode was carried out for a unidirectional gr/ep composite laminate. The CPT flexural equation of motion for an orthotropic material was used and again a normal mode solution was obtained. Experiment and theory were com-

pared for propagation at different angles of propagation with respect to the fiber axes. Agreement between theory and experiment for the composites was not nearly as good as that for the aluminum. The deviation of the material properties from those predicted was one culprit in the disagreement between theory and experiment. The major source of error was the limitations of CPT which had been demonstrated by the dispersion measurements. HOPT calculations of the flexural mode wave shape are being considered, but are not discussed in this thesis.

Additional measurements were carried out on a thin-walled gr/ep composite tube of the design and layup designated to be used on the structural struts holding together NASA's Space Station Freedom (SSF). The layup of this tube was $[10,-10,30,-30,10,-10]_s$. Even though the geometry of this tube was not the same as that of a simple flat plate, similar extensional and flexural modes were observed in AE signals from simulated sources. The velocities of the extensional mode and the flexural mode at very low frequency were measured and compared with predictions from the simple classical plate theory. Good agreement was obtained.

This work further demonstrated the importance of plate waves in the interpretation of AE signals in plate or plate-like materials. The effect of source orientation on the plate modes was documented. This demonstrated the potential for obtaining source information from the observation of these modes. Classical plate theory was shown to adequately predict the flexural plate mode displacements in a finite aluminum plate. In composite plates, it was proven that a higher order plate theory was needed to account for the effects of shear and rotator inertia. However, in either case, the advantage

of these theories over the exact theory used in previous quantitative AE studies is its relative simplicity. This allows its implementation on finite plates and for anisotropic materials such as composites which has not been previously possible. Furthermore, although the restriction to thin plates or shells might seem to be a limitation, it is pointed out that many structures of practical testing interest can be approximated as thin plates or shells. An example given by the SSF strut tube was examined.

II. Transducer Evaluation

II.1 Introduction

As discussed in the introduction, previous research by Gorman [35] indicated that a conventional damped, thickness gauging, ultrasonic transducer with a nominal resonance peak of 5 MHz provided broad band response to AE signals in the low kHz to 1 MHz frequency bandwidth. In this research, experiments were carried out to better characterize a similar ultrasonic transducer which had a nominal resonance of 3.5 MHz. These experiments were performed for several reasons. The first was to demonstrate that the voltage output of the ultrasonic transducer was proportional to the normal surface displacement over the range of frequencies contained within AE signals in thin plates. The second was to obtain a relative calibration of variations in the amplitude response of the ultrasonic transducer as a function of frequency. The final motivation was to compare the response of this transducer to those of several conventional AE sensors.

The demonstration of the displacement sensitivity of the ultrasonic transducer was necessary so that comparisons of experimental waveforms detected by this sensor could be made with theoretical predictions of the surface displacement of the flexural plate mode in later work. It was accomplished by comparing the voltage output of this transducer to that of a displacement sensitive optical interferometer when both were detecting simulated AE signals in a thin aluminum plate. These simulated AE signals were generated by pencil lead breaks (Hsu-Neilsen sources) and were detected by both sensors at equal distances of propagation from the source. Good agreement was

obtained which demonstrated that the ultrasonic transducer was indeed displacement sensitive over the range of frequencies contained in the plate modes of the AE waveforms.

The displacement sensitivity of the ultrasonic transducer was further demonstrated by comparing its output to theoretical displacement predictions for a waveform in a thick aluminum plate which was again generated by a pencil lead break. These theoretical predictions were obtained using the computer program by Hsu [20].

Additional research by Gorman [37] has since demonstrated the displacement sensitivity of the 5 MHz ultrasonic transducer that was used in his experiments. He compared the voltage output of his ultrasonic transducer to that of the NIST conical transducer which was reported by Proctor [17] to be displacement sensitive. The signals used to compare the transducers were flexural mode plate waves caused by lead breaks on the surface of a thin aluminum plate.

The amplitude response as a function of frequency of the 3.5 MHz ultrasonic transducer was needed to allow better comparisons with theoretical predictions of flexural mode waves in thin plates. This was accomplished by driving the transducer with a nominally identical ultrasonic transducer which was excited by a swept sine tone burst electrical signal which had constant amplitude from 20 kHz to 1.5 Mhz. The sensors were coupled together in a face-to-face manner as described by Dunegan [38]. The output response of the driving transducer was deconvolved from the measured frequency response. Although this technique does not provide an absolute calibration of the transducer in terms of volts of output per unit displacement at each frequency, it yields a relative calibration of how the amplitude of the output of the transducer varies with frequency for a

constant level of input. This was all that was needed in the later work on predicting the flexural mode waveform to allow good comparisons between theory and experiment. Furthermore, this calibration method was used on the conventional AE sensors and showed the superior frequency response of the ultrasonic transducer. A comparison of the calibration obtained with this technique was shown to be in good agreement with that of one of the conventional AE sensors which was obtained from the manufacturer.

In all, four different transducers were evaluated. The first was a conventional ultrasonic transducer (Panametrics). This sensor was designed to be used as an ultrasonic generator or receiver and has a broad band frequency response centered at 3.5 MHz. As an AE detector, it was used to detect signals at much lower frequencies. The diameter of this transducer was 1.27 cm.

The second sensor evaluated was a conventional resonant AE sensor (Physical Acoustics Corporation model R15). The R15 was reported by the manufacturer to have a primary resonant frequency near 150 kHz. Typical application of this transducer pairs it with a 100-300 kHz bandpass filter in the preamplifier. The diameter of this transducer was also 1.27 cm. The R15 and transducers made by other manufacturers with similar frequency characteristics are probably the most widely used AE transducers in conventional AE testing.

The third sensor was an AE sensor (Physical Acoustics Corporation model S9208) which was designed to have a broad band frequency response over the 100 kHz to 1Mhz range. Over this range, the S9208 was reported to be a displacement sensor providing a voltage output proportional to the surface displacement. The overall diameter of the sensor was 2.54 cm. However, the active area in contact

with the specimen had a diameter of only 1.27 cm.

The final sensor studied was a Pinducer (Valpey-Fisher model VP-1093). This sensor was also designed to be broad band with a reported frequency range from near DC to 1.2 MHz. However, this sensor was sensitive to the velocity of the surface instead of the displacement according to the manufacturers literature and as demonstrated by these experiments. Additionally, it offered essentially point detection capability because of its very small diameter. The diameter of the active element was 0.135 cm.

II.2 Frequency response determination by constant amplitude, swept-sine input

In this experiment the input signal for evaluating the frequency response of the transducers was the vibration of another 3.5 MHz ultrasonic transducer (Panametrics). It was coupled face-to-face to the transducer under evaluation using a silicone grease compound. The driving ultrasonic transducer was excited by a constant amplitude, swept-sine, tone burst electrical signal. This signal was generated with a function generator (Krohn-Hite Model 5300). The outputs of the transducers were digitized at a 5 MHz sampling frequency (0.2 μsec. sampling rate) with a transient recorder (Lecroy Model 6810). No preamplification or filtering of the transducer outputs was used. The waveforms were recorded on a personal computer (IBM AT) for future analysis and display. A block diagram of the experimental apparatus is shown in Figure 2.1.

The frequency range of the driving electrical signal was approximately 20 kHz to 1.5 MHz with a linear increase in frequency over the duration of the pulse. The pulse duration was 92 μsec and its ampli-
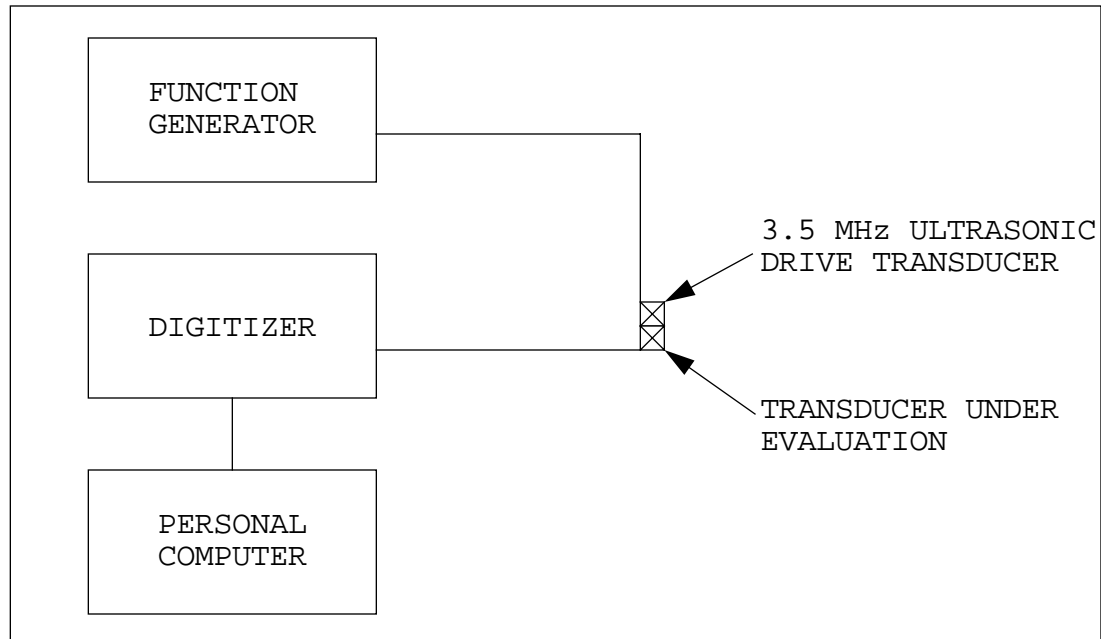
Figure 2.1   Experimental apparatus for constant amplitude,
              swept-sine input for AE transducer evaluation.

tude was 17 volts peak to peak. A plot of the digitized time record

of this input signal is presented in Figure 2.2. Apparent

variations in the peak amplitude of the signal occur in this plot

during later times of the pulse. This was an artifact of insufficient

digital sampling at the higher frequencies of the pulse. These higher

frequencies arrived during later times of the pulse due to the swept-

sine nature of the pulse. Although the digitized waveform did not

yield a truly accurate representation of the peak amplitude of the

signal at these high frequencies, the maximum frequency content of

the input signal (1.5 MHz) was below the Nyquist cutoff frequency

of 2.5 MHz for the 5 MHz sampling frequency. Thus aliasing of the

signal should not have occurred.

The frequency response of this signal was computed by means of a

digital Fast Fourier Transform (FFT) using a wave analysis software
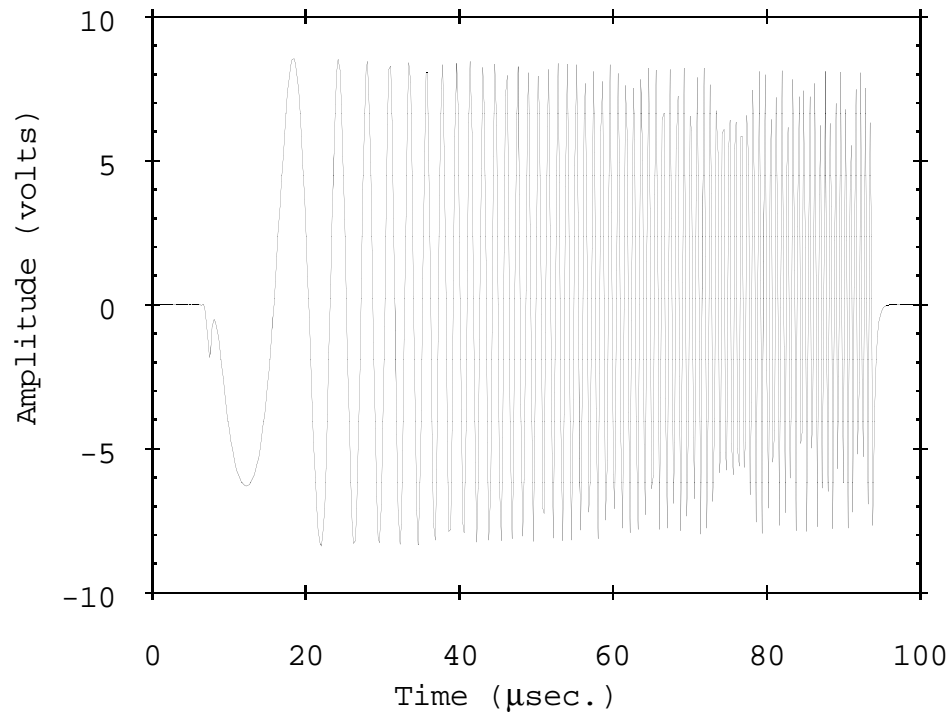
Figure 2.2   Constant amplitude, swept-sine, tone burst input
signal used for transducer evaluation.

package (Keithley Asyst 2.1) on the personal computer. The

magnitude of the spectrum of this signal is plotted in Figure 2.3. In

this figure, the magnitude of the spectrum was presented on a loga-

rithmic scale where the decibel (dB) was referenced to one μvolt.

The spectrum exhibited the expected constant amplitude of the input

excitation signal over the 20 kHz to 1.5 MHz frequency range.

The output signals of each of the four transducers when

subjected to this input were recorded and are depicted in Figure

2.4 to Figure 2.7. The sensitivities of the transducers, which are

the ratios of the output voltage to the input mechanical vibration

are all different. Because of this variation in sensitivity and the

linear amplitude scales used in the plots, the amplitude scales of

these four plots are different. This allows the details of each wave-

form to be clearly seen.
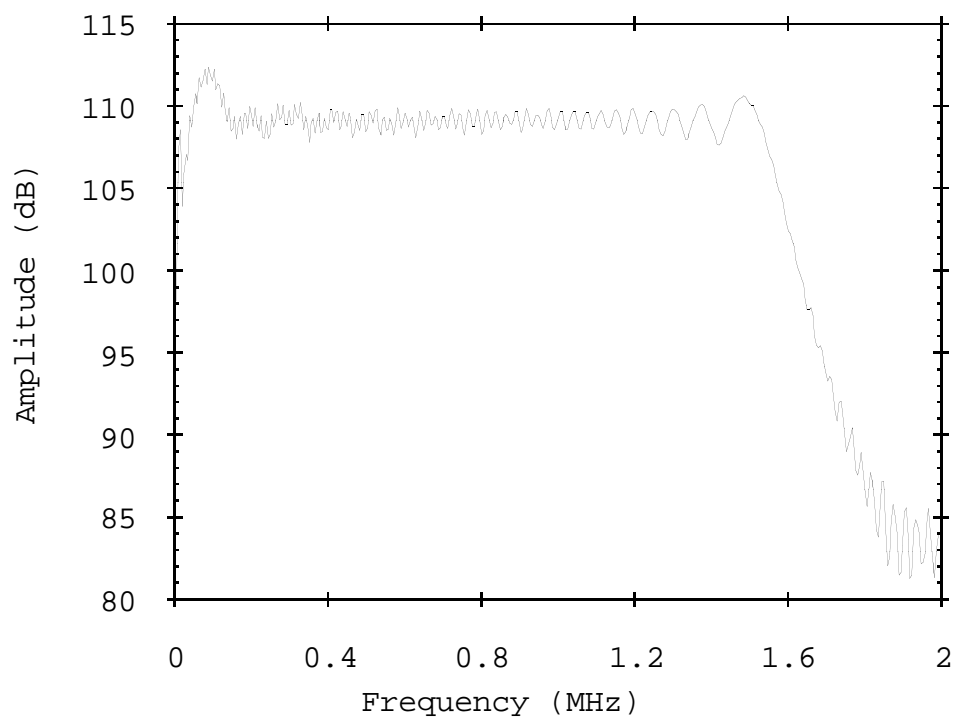
Figure 2.3   Magnitude of frequency spectrum of transducer
drive input signal (Figure 2.2).
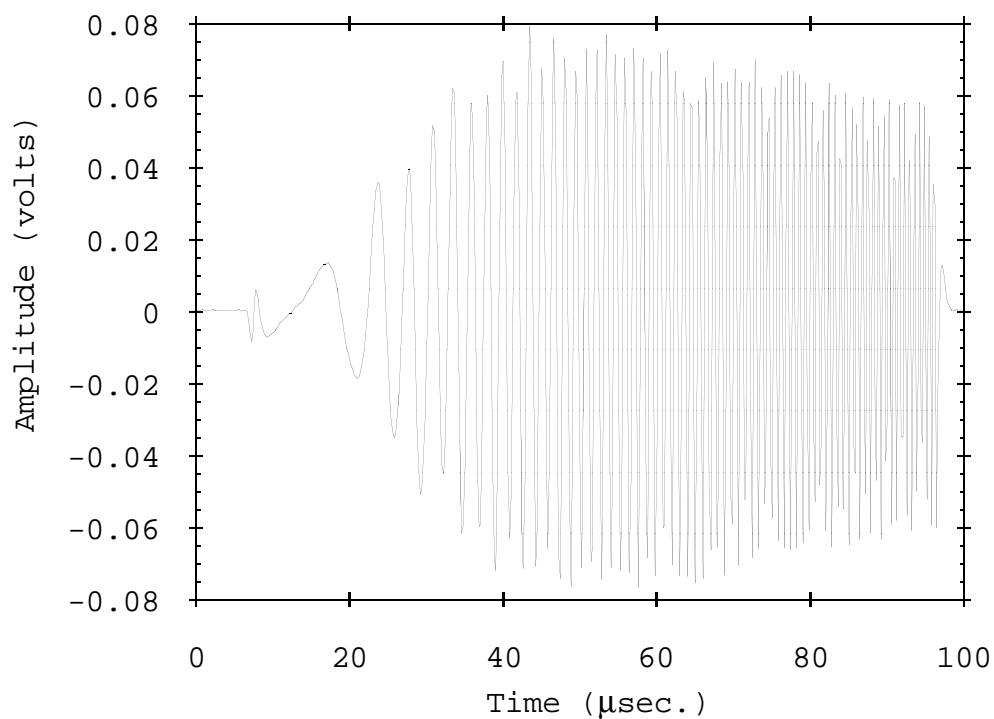
Figure 2.4   Output of 3.5 MHz ultrasonic transducer subject-
ed to constant amplitude, swept-sine input.
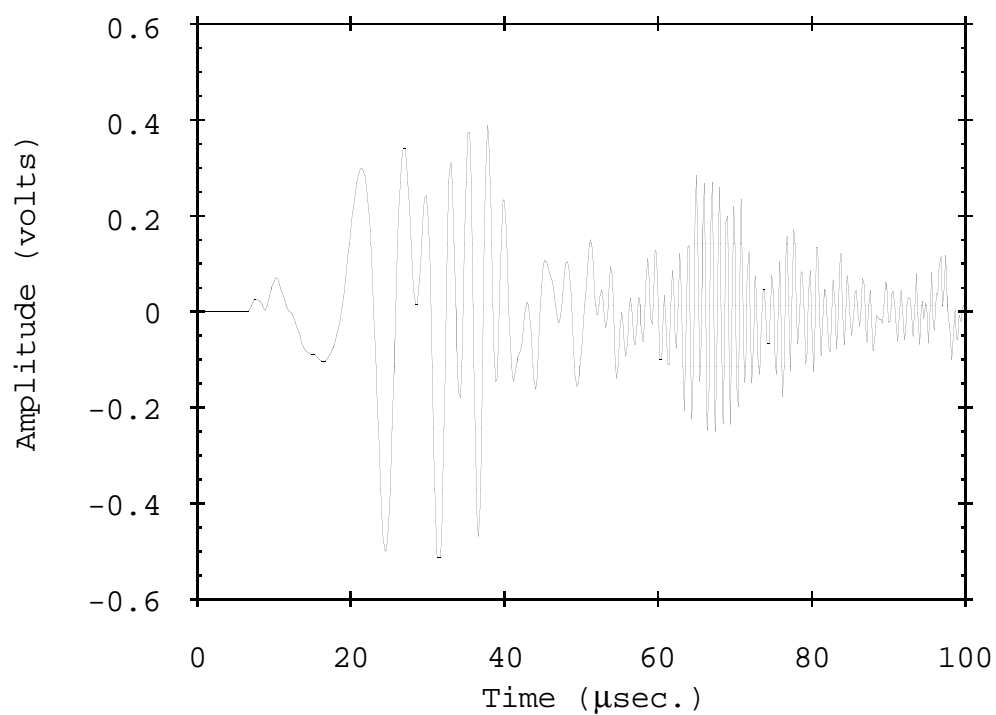
Figure 2.5   Output of R15 transducer subjected to constant
amplitude, swept-sine input.
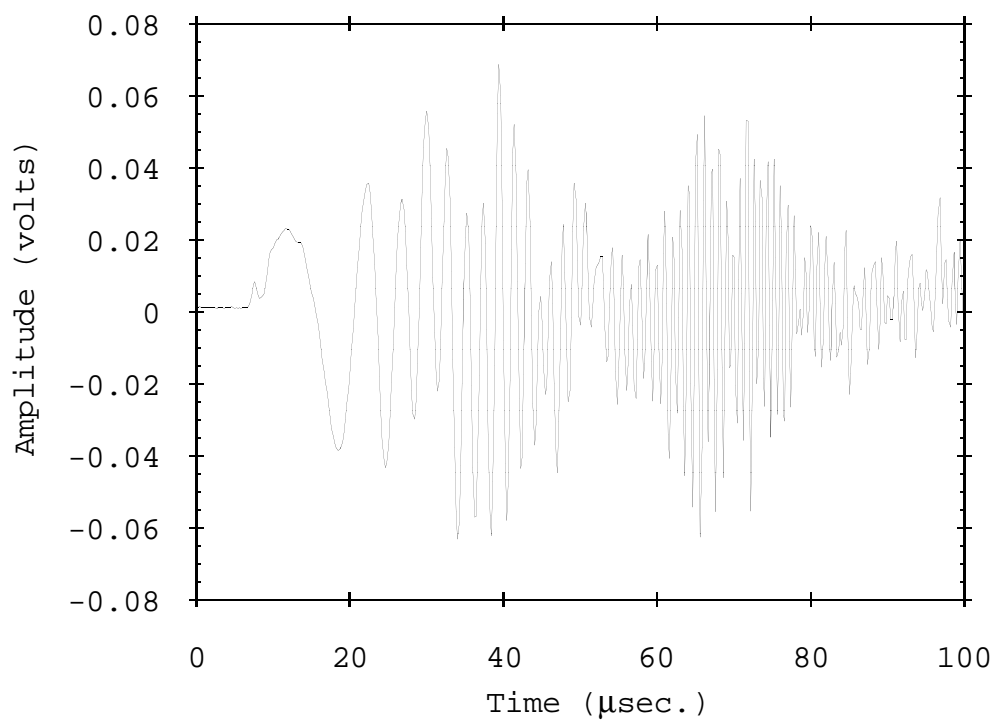
Figure 2.6   Output of S9208 transducer subjected to constant
amplitude, swept-sine input.
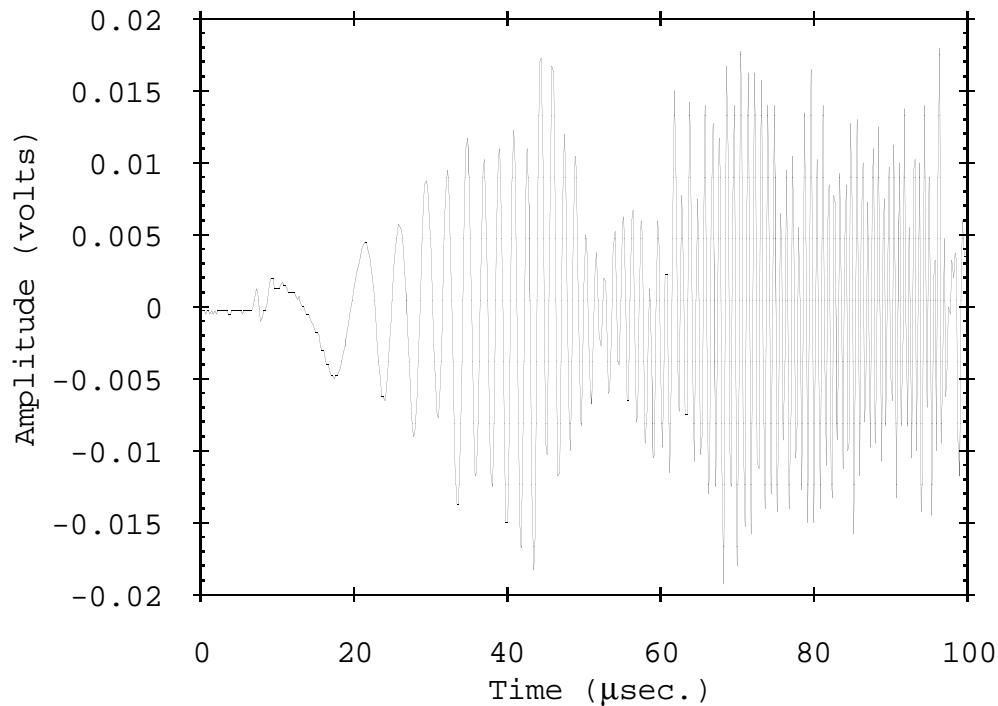
Figure 2.7   Output of Pinducer transducer subjected to con-
stant amplitude, swept-sine input.

The R15 exhibited the highest peak sensitivity over this frequency

range as demonstrated by the largest peak amplitude output voltage

for the constant amplitude input vibration. The ultrasonic transducer

and the S9208 were next in order of decreasing peak sensitivities

with similar peak amplitudes. The peak amplitudes of these two trans-

ducers were only about a factor of six less than that of the R15

which on a logarithmic scale was a reduction of about sixteen dB. The

Pinducer had the smallest peak voltage output.

The high peak sensitivity of the R15 was expected because of its

narrow band resonant design. This resonant frequency response was

demonstrated in Figure 2.5 by the large variations in amplitude of

the waveform as the frequency increases with time. This behavior will

be more clearly demonstrated in the frequency spectrum plots to fol-

low. The output of the ultrasonic transducer was much flatter indi-

cating a better frequency response while the amplitude fluctuations of the S9208 and the Pinducer indicated some resonant structure.

Although, the frequency responses of the transducers were observed in the time domain signals because of the linear swept-sine constant amplitude nature of the input, it was more clearly revealed by examining the magnitude of the spectrum of the signals. Again, FFT's were performed on the signals and converted to a logarithmic scale referenced to one μvolt. Plots of the spectrums are presented in Figure 2.8 to Figure 2.11 where the logarithmic ampli-
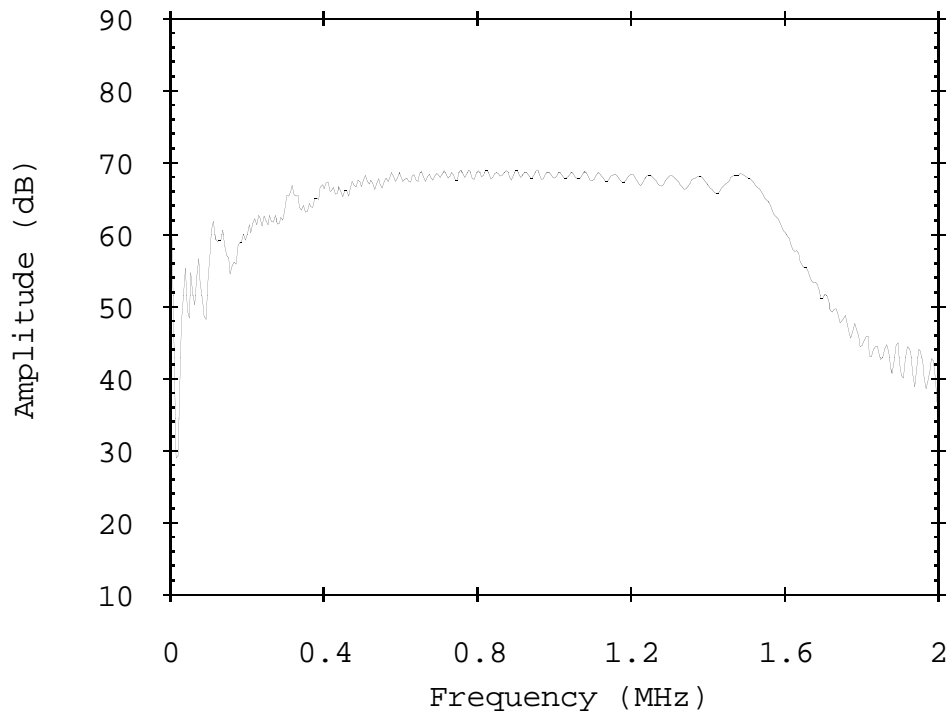
Figure 2.8   Spectrum of 3.5 MHz ultrasonic transducer sub-
             jected to constant amplitude, swept-sine input.

tude scale allows the plots from all of the transducers to be shown on the same scale.

Although the input electrical signal applied to the driving ultra-sonic transducer was of constant amplitude, the output of this trans-ducer most likely, was not. This was because the output response of
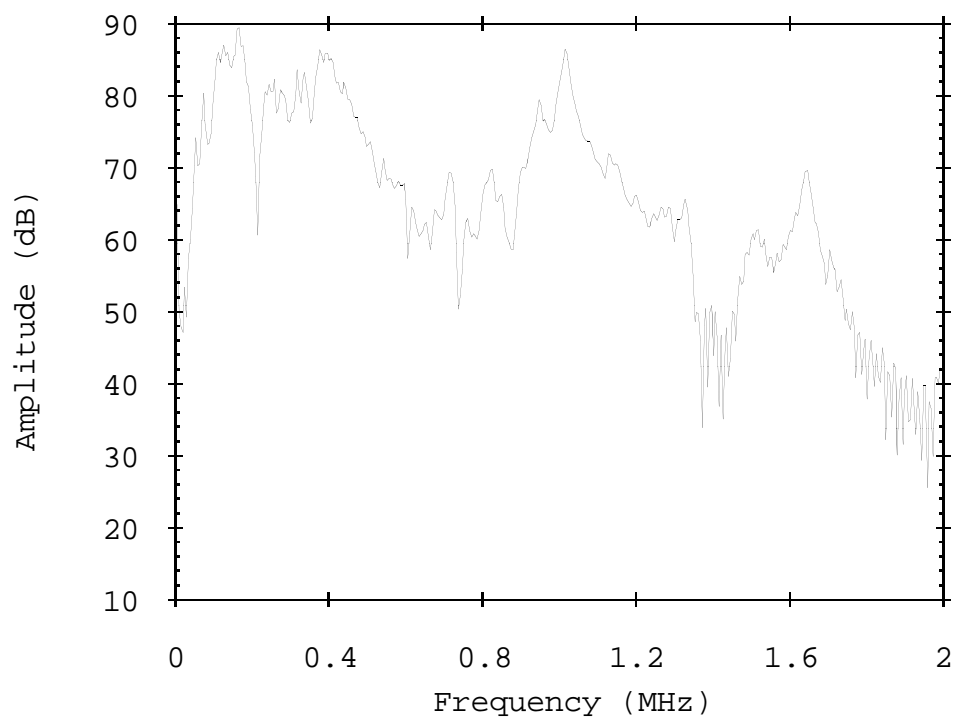
Figure 2.9   Spectrum of R15 transducer subjected to constant
              amplitude, swept-sine input.
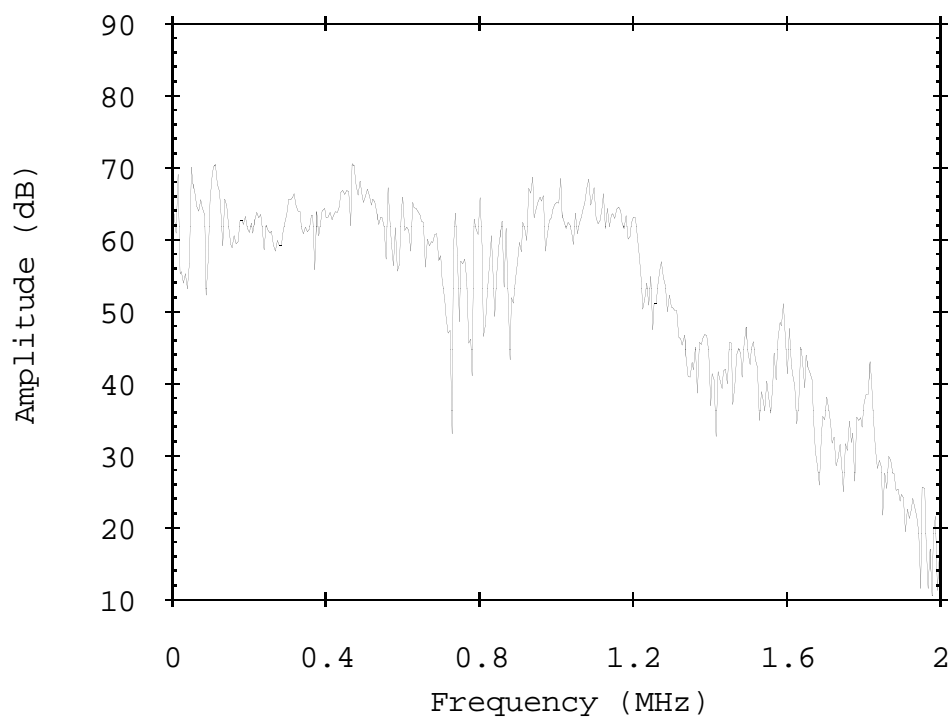
Figure 2.10   Spectrum of S9208 transducer subjected to con-
              stant amplitude, swept-sine input.
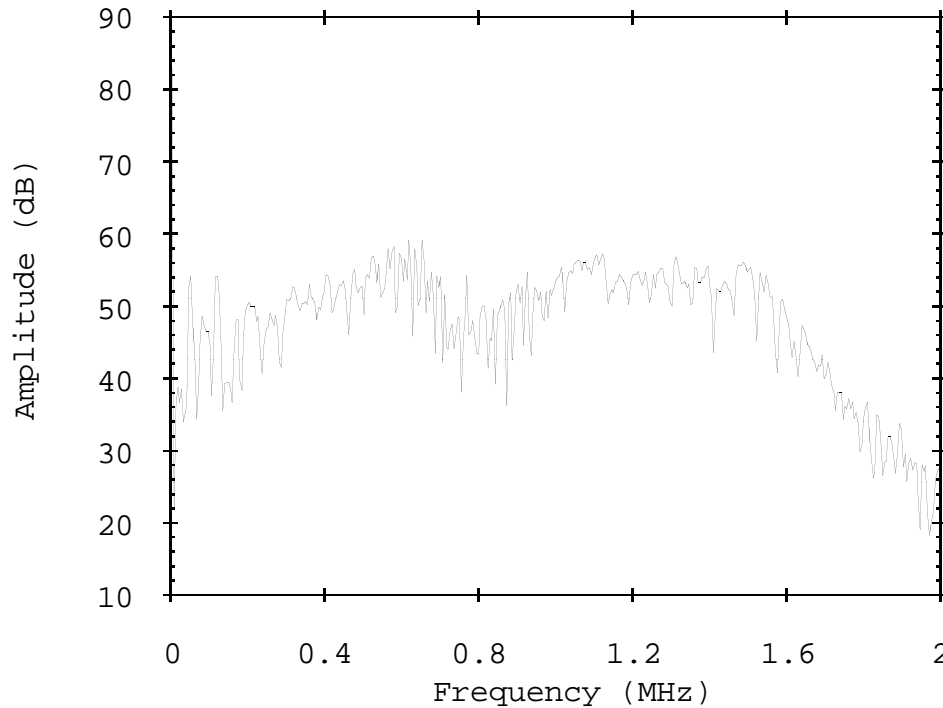
Figure 2.11   Spectrum of Pinducer transducer subjected to con-
stant amplitude, swept-sine input.

this transducer changed this signal and caused the actual input to

the transducers under evaluation not to be of constant amplitude.

Thus, the previous spectrum plots provided only a relative comparison

of the outputs to this common input and are not truly the frequency

responses of the transducers. To determine this, the effect of the

output response of the driving transducer was deconvolved from the

output signals.

   To accomplish this deconvolution, several assumptions were made.

First, the coupling layer and impedance mismatches between the dif-

ferent transducer faces were neglected. Next, it was assumed that the

input and output electronics as well as the input and output trans-

ducers all behaved in a linear fashion. This allowed linear

transfer function formalism to be applied. In linear transfer func-

tion formalism, the output of a device is the convolution of the in-

put signal with the response function of the device. Thus, the output
of the transducer under evaluation (TO) can be expressed as

$$TO \,=\, EI \otimes DR \otimes TR \otimes DE \qquad\qquad \text{Eq. 2.1}$$

where EI is the electrical input drive signal, DR is the output re-
sponse of the driving transducer, TR is the actual response of the
transducer under evaluation, DE is the response of detection elec-
tronics, and $\otimes$ represents convolution. This convolution can be ac-
complished in the frequency domain as a simple multiplication of
the frequency responses while deconvolution is carried out as a divi-
sion in the frequency domain.

The frequency responses of the electrical input signal (EI(f)) and
of the output of the transducer under evaluation (TO(f)) were known
from the FFT's of these two signals. Additionally, it was assumed
that the response of the detection electronics (the transient record-
er) was flat and equal to unity. Thus, Eq. 2.1 was rewritten as

$$TO(f) \,=\, EI(f) \times DR(f) \times TR(f) \qquad\qquad \text{Eq. 2.2}$$

where only the desired TR(f) and the output response of the driving
transducer (DR(f)) remain unknown. To evaluate DR(f), one further as-
sumption was made. It was assumed that the output response of the
driving ultrasonic transducer was equal to its input response.
Thus, in the case where the two nominally identical ultrasonic trans-
ducers are coupled together for evaluation,

$$TO(f) \,=\, EI(f) \times DR(f)^2 \qquad . \qquad\qquad \text{Eq. 2.3}$$

This enables DR(f) to be evaluated from the expression

$$DR(f) = \sqrt{\frac{TO(f)}{EI(f)}}$$

when TO(f) was the response obtained when the ultrasonic transducer was under evaluation. After DR(f) was determined, the response function of each transducer TR(f) was evaluated by

$$TR(f) = \frac{TO(f)}{EI(f) \times DR(f)} \qquad .$$

The resulting output response function of the ultrasonic drive transducer was plotted in Figure 2.12. This is also the deconvolved
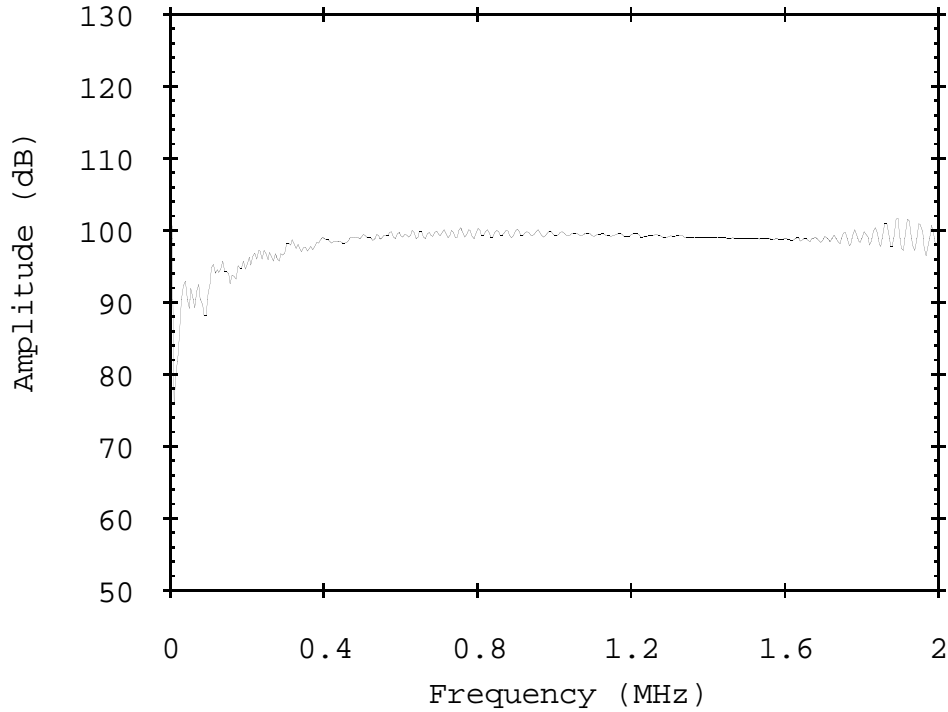
Figure 2.12   Deconvolved output and input response function
              of 3.5 MHz ultrasonic transducer.

input response function for this transducer. The deconvolved input response functions of the remaining three transducers are presented in Figure 2.13, Figure 2.15, and Figure 2.16. These were also all
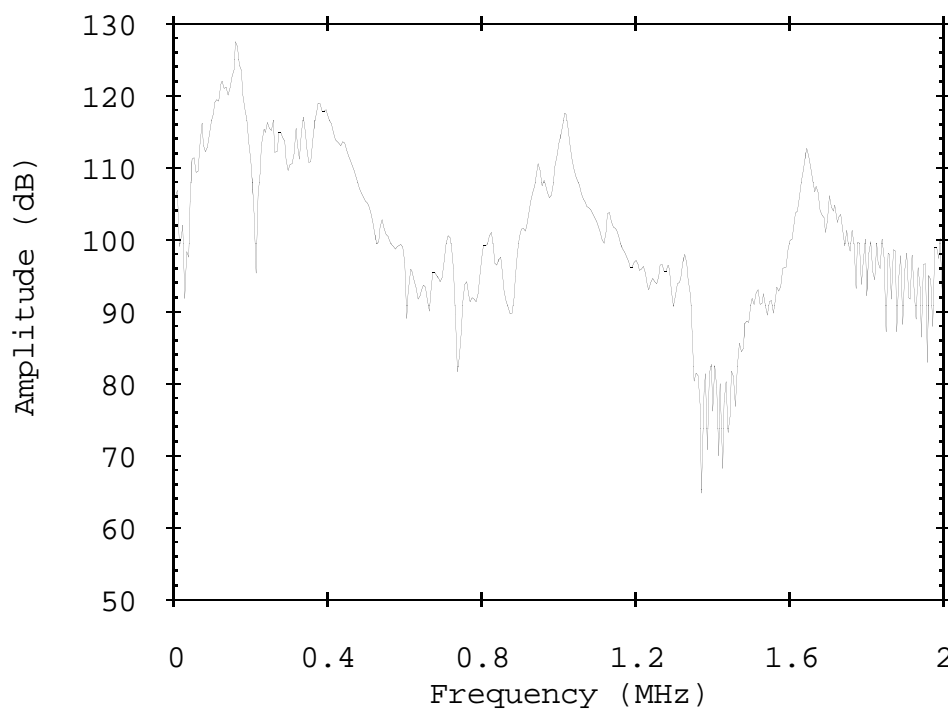
Figure 2.13 Deconvolved response function of R15 transducer.
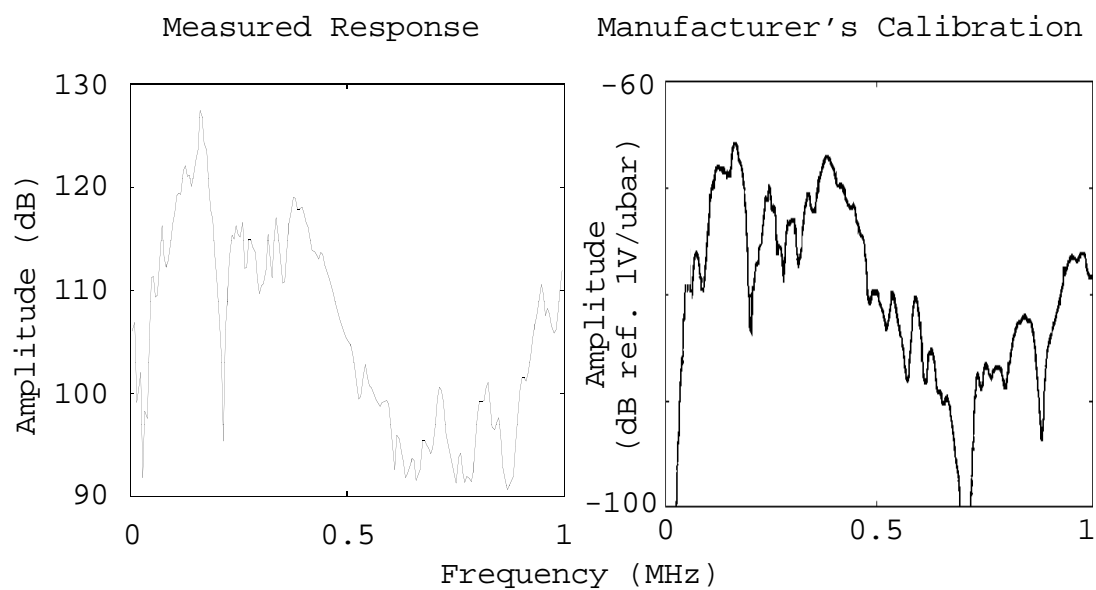
Figure 2.14 Measured frequency response and manufacturer's calibration for R15 transducer.
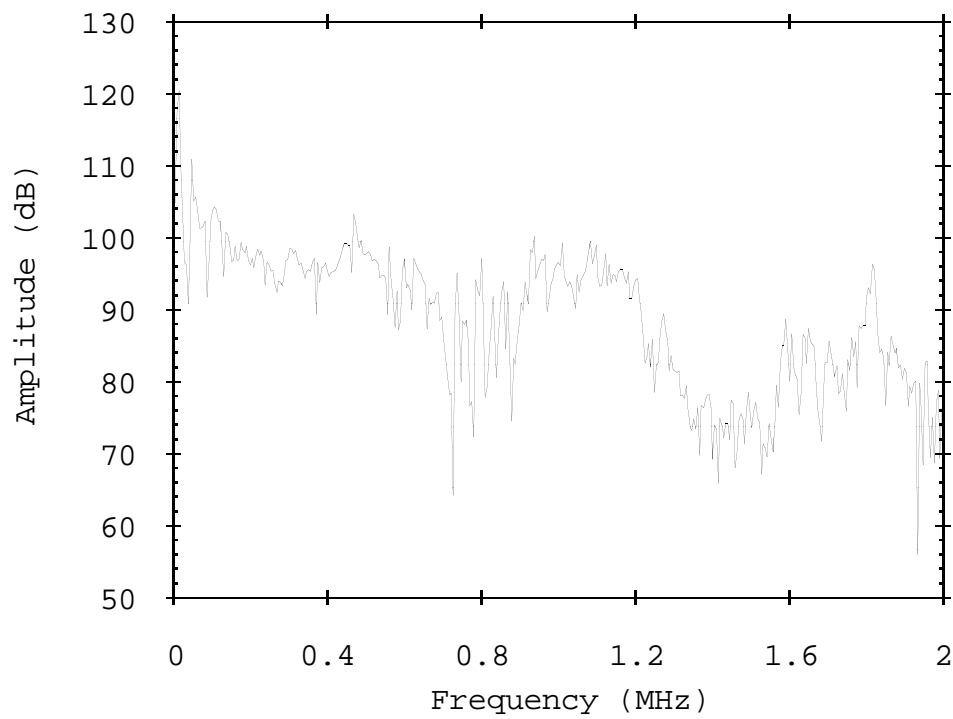
Figure 2.15   Deconvolved response function of S9208 transducer.
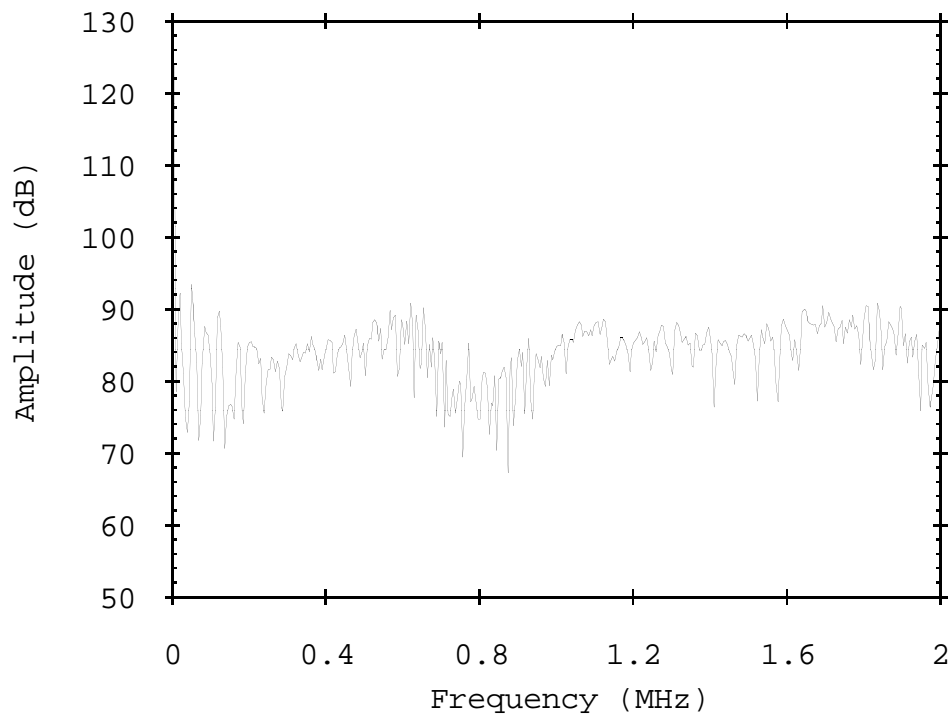
Figure 2.16   Deconvolved response function of Pinducer transducer.

plotted on identical logarithmic amplitude scales for comparison. As expected from the previous time domain plots, the R15 had the largest peak amplitude, but large resonant structure was present. The largest resonant peak was at 158 kHz which was near the reported resonant frequency of 150 kHz for this sensor. Other peaks were also present at 375 kHz and 1 MHz. A calibration for this sensor which was obtained from the manufacturer is shown in Figure 2.14 along with the measured frequency response. Good agreement is seen between the two curves.

The ultrasonic transducer demonstrated a very flat response above 400 kHz. Below this frequency, the response dropped off in a roughly linear fashion with frequency except for a couple of small resonant peaks. The plots for the S9208 and the Pinducer demonstrated resonant behaviors, although they were not as severe as that of the R15.

These figures again demonstrate the superior flat frequency response of the 3.5 MHz ultrasonic transducer and the resonant structures of the other sensors. In the deconvolved responses, the difference in peak amplitudes between the R15 and the ultrasonic transducer was approximately 25 dB.

Thus, from this analysis, it was clear that the 3.5 MHz ultrasonic transducer offered a much flatter frequency response and therefore better fidelity than any of the sensors tested. Not only were its frequency characteristics better, it had a sensitivity in terms of peak amplitude equal to that of a conventional broad band AE transducer. Its peak amplitude output was approximately 25 dB less than that of the R15, which had a severe resonant structure. However, it is again pointed out that this was only a relative comparison of

the behavior of the different sensors and not an absolute calibration. A number of assumptions were made such as neglecting the coupling layer, any impedance mismatches between the different sensor faces, as well as the assumptions stated in the deconvolution analysis.

II.3 Acoustic wave input generated by pencil lead break on thick aluminum plate and comparison with theory

In these experiments, the outputs of the four different transducers were compared when the common input stimulus was an acoustic wave generated in a large, thick aluminum plate by a pencil lead break (Hsu-Neilsen source). This source is commonly used to simulate an AE event because the transient nature of the breaking of the lead is similar to the transient nature of many real AE sources such as crack growth. This simulated source is often modeled as a point source, step function unloading of the surface.

The plate used for these experiments was 2024 aluminum. Its thickness was 2.54 cm. while the lateral dimensions were 122 by 61 cm. Large lateral dimensions were necessary in order to avoid reflections of the acoustic wave from the lateral boundaries within the time period of observation. The source and detector were also positioned near the center of the plate to minimize reflections. Using the measured velocity of the fastest wave, the longitudinal wave, of 6540 m/s., the first reflection from a lateral boundary should not occur until 186 μsec. after the source motion. Only the first 60 μsec. of the signal were compared with theory. Since no reflections from the lateral boundaries took place during this period, the plate was approximated as being infinite in lateral extent. Thus, comparisons

with theoretical predictions for an infinite plate could be used.

Generalized ray theory, which was discussed briefly in the intro-
duction [Chapter I, p. 9], was used for these calculations. This the-
ory also required that the plate be at least ten times thicker than
the distance of propagation. A distance of propagation of 7.62 cm.
was chosen which easily met this requirement. The source and receiver
were both on the same side of the plate. The source-receiver configu-
ration is shown in Figure 2.17. One further assumption was made in
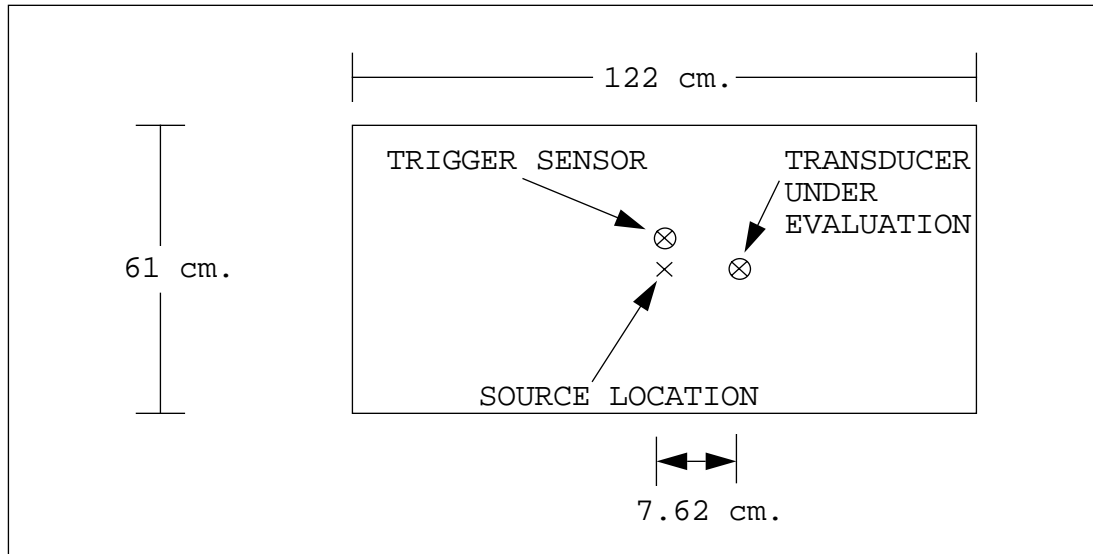
Figure 2.17   Source, trigger sensor, and transducer position-
ing for evaluation of transducers with simulated
AE source in thick aluminum plate.

these calculations. That is, both the source and the detector are
points or have very small spatial extent. In the case of the lead
break source, this assumption was valid because of the small diameter
of the lead. However, the area of the receivers were much larger.
This was a source of disagreement between the measured waveforms
and theoretical predictions.

The transducers evaluated were the same as those in the previous

section. An additional R15 sensor was placed next to the source loca-
tion. Its output was used to trigger the recording of the waveform by
the transient recorder. Again a 5 MHz sampling frequency was used
in the digitization of the signals and the recorded signals were
stored on the personal computer for later display and analysis.

Because of the small voltage output of these sensors for this in-
put, the signals were first preamplified. The preamplifier
(Physical Acoustics Corporation model 1220A) amplified the signal
by 40 dB. The internal filter of this preamp was removed and replaced
with a 1 μF capacitor as per the manufacturers instructions. This al-
lowed the preamp to perform with the broadest bandwidth possible. The
frequency response of the preamplifier was characterized with tone
burst input signals of various frequencies from a function generator.
It was found to be essentially flat from near D.C. to 1.5 MHz.

One problem in examining the signal output of this preamp was that
the input 28 volt D.C. power supply and the output of the preamp
traveled over the same BNC cable in a so-called phantom power ar-
rangement. This was overcome by A.C. coupling the output/power supply
signal to the transient recorder which removed the 28 volt D.C. level
from the signal. The 28 volt power was provided by a conventional
AE system (Physical Acoustics Corporation model Locan-AT). A block
diagram of the experimental apparatus is presented in Figure 2.18.

In addition to simply comparing the outputs of the different
transducers to each other, the outputs were compared to that predict-
ed by theory. This was accomplished using a computer program by Hsu
[20] which calculated the components of the Green's tensor, G_{ij}
($\bar{\xi}, \bar{x}, t$), for an isotropic, thick plate of infinite lateral extent.
The components of this tensor are the i'th component of the displace-
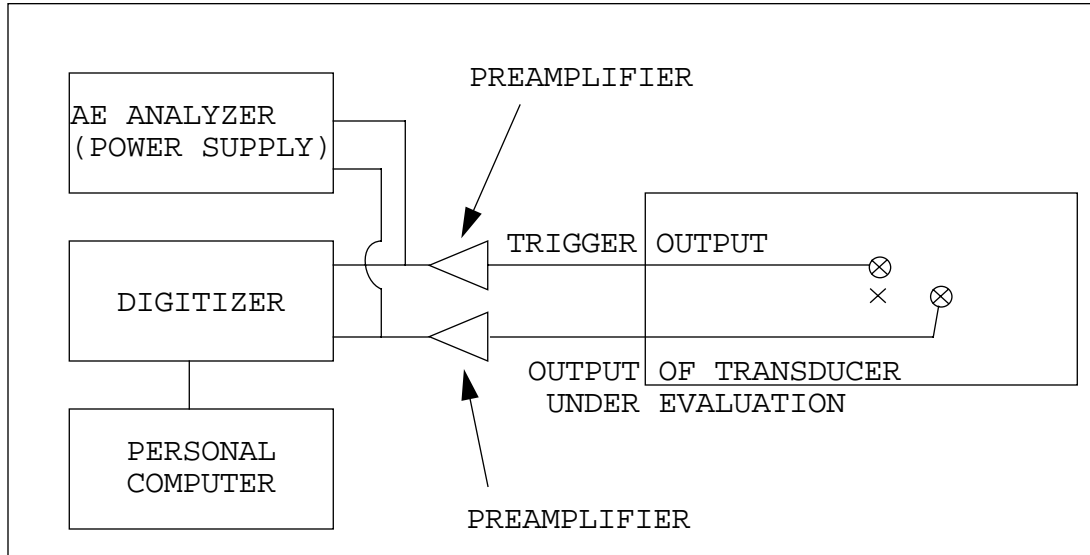
Figure 2.18 Experimental apparatus for evaluation of trans-
ducers with simulated AE source in thick alumi-
num plate.

ment at $\bar{x}$ due to a point force of step-function time dependency oc-

curring at $\bar{\xi}$ in the j'th direction. An overbar is used to designate

vector quantities. The force was assumed to be initiated at t=0.

   The theoretical basis of this program was an approach known as

generalized ray theory. A detailed explanation of this approach was

presented by Eitzen et al. [13]. Another detailed presentation of the

generalized ray approach to the solution of problems involving

waves propagating in thick plates was put forth by Pao and Gajewski

[39] and is reviewed by Pao et al. [19]. A detailed analysis of gen-

eralized ray theory is well beyond the scope of this work. However,

the basic concepts of linear elasticity on which it is based and a

brief discussion of the concept of generalized ray theory are pre-

sented below.

   The plate is assumed to behave in a linear elastic fashion.

Thus, the stresses (σ_{ij}) are related to the strains (ε_{kl}) through

Hooke's law,

$$\sigma_{ij} = c_{ijkl}\varepsilon_{kl} \qquad \text{Eq. 2.6}$$

where c_{ijkl} is the elastic stiffness tensor. The Einstein summation convention regarding repeated indices applies here and throughout the remainder of this work. Because the deformation of the material is assumed to be small, the small strain definition of the strain tensor is used which is given by

$$\varepsilon_{ij} = \frac{1}{2}\left(\frac{\partial u_i}{\partial x_j} + \frac{\partial u_j}{\partial x_i}\right) \qquad \text{Eq. 2.7}$$

where u_i are the displacements and x_i are the coordinate axes of the body. Furthermore, the material of the plate is assumed to be isotropic. Thus, only two independent elastic coefficients are needed to describe the behavior of the material. The Lame' coefficients λ and μ are used. This allows the rewriting of Eq. 2.6 as

$$\sigma_{ij} = \lambda\varepsilon_{kk}\delta_{ij} + 2\mu\varepsilon_{ij} \qquad \text{Eq. 2.8}$$

where δ_{ij} is the Kronecker delta.

The governing equations of motion are given by

$$\frac{\partial\sigma_{ij}}{\partial x_j} + \rho f_i = \rho\frac{\partial^2 u_i}{\partial t^2} \qquad \text{Eq. 2.9}$$

where ρ is the mass density and f_i are the components of the body force per unit mass of material. Using Hooke's law for an isotropic

material to substitute for the stress, the definition of strain, and assuming the material to be homogeneous, these governing equations can be rewritten in terms of the displacements as

$$(\lambda + \mu)\,\nabla\,(\nabla \cdot \bar{u}) + \mu \nabla^2 \bar{u} + \rho \dot{\bar{f}} = \rho \frac{\partial^2 \bar{u}}{\partial t^2} \quad .$$

Eq. 2.10

The forcing function for a lead break is assumed to have a time dependence of the Heaviside step function, $H(t)$, which is equal to 0 for $t<0$ and 1 for $t \geq 0$. The spatial dependence is assumed to be that of a point source.

Solutions to these equations of motion with this type of forcing function for an infinite isotropic body have been determined. An example is given by Pao [40]. These solutions show that two waves are generated that propagate outward from the source. The first is a longitudinal wave that has a velocity, (c_1), given by

$$c_1 = \sqrt{\frac{\lambda + 2\mu}{\rho}} \quad .$$

Eq. 2.11

The second is a shear wave which travels with a slower velocity, (c_s), given by

$$c_s = \sqrt{\frac{\mu}{\rho}} \quad .$$

Eq. 2.12

In the case of propagation in a plate, these same waves are emitted from the source. However, as the waves propagate away from the

source, they will interact with the boundaries. Each wave may reflect and mode convert or generate surface waves depending on the angle of incidence and the boundary conditions on the surface of the plate. In the generalized ray approach, a calculation of the displacement contribution of each generalized ray that will reach the detection location from the source is made for a certain length of time. This generalized ray may be a direct traveling wave or a wave that has undergone reflections and mode conversions. The contributions of all of these generalized rays are summed up to give the displacement at the detector position. Thus, the solution is exact for the length of time evaluated. For later times, it is incorrect because additional waves will arrive whose displacement contributions have not been taken into account. The difficulty in this approach is that the number of reflections grows exponentially with time. This causes limitations on the length of time and distance of propagation for which the solution can practically be calculated.

A computer program was written by Hsu [20] to evaluate the displacement of a thick plate for the case when the input forcing function was a Heaviside step function (H(t)). This code was written in Fortran and in this case was run on a VAX 780 (Digital Equipment Corp.) computer. The inputs required by the program were the distance from the source to the detector (assumed to be on the upper surface of the plate), the location along the z axis of the source, the thickness of the plate, the shear and longitudinal wave speeds of the plate, the shear modulus of the plate, the number of points to evaluate, the time step between each point, and the amplitude of the source. Additionally, the direction of the applied force and the direction of the motion to be predicted had to be input as indices into

the program since it could evaluate any component of the Green's tensor, G_{ij}.

The source to receiver distance was set equal to 0.0762 m. and the source was positioned on the same surface as the receiver. This matched the theoretical assumptions to the experimental conditions. The longitudinal and shear wave speeds were measured ultrasonically by a pulse-echo technique using longitudinal and shear wave transducers to generate and detect the respective longitudinal and shear waves. The values determined were c_l= 6540 m/s. and c_s= 3210 m/s. The shear modulus was calculated using the measured shear wave velocity and an assumed density of 2690 kg/m^3. Its value was determined to be 27.7 GPa. The plate thickness was input as 0.0254 m. Since the source amplitude was not experimentally measured, it was set equal to 1. The program output was then normalized for each transducer to allow relative comparisons. The indices of G_{ij} used were 33 to evaluate the displacement normal to the surface (z direction) caused by a force also normal to the surface. 256 points were calculated with a time spacing between points of 0.2 μsec.

The output of the program was the absolute amplitude of the normal component of the surface displacement in m. which is plotted in Figure 2.19. The largest peak in the displacement shown in this Figure is caused by the Rayleigh wave. A number of other waves arrive before this peak including the direct longitudinal wave, the once and twice reflected longitudinal waves, and a shear wave that was created by the mode conversion of a longitudinal wave upon reflection. These all have much smaller amplitudes than that of the Rayleigh wave. The next larger peak after the Rayleigh wave coincides with the predicted arrival of the once reflected shear wave.
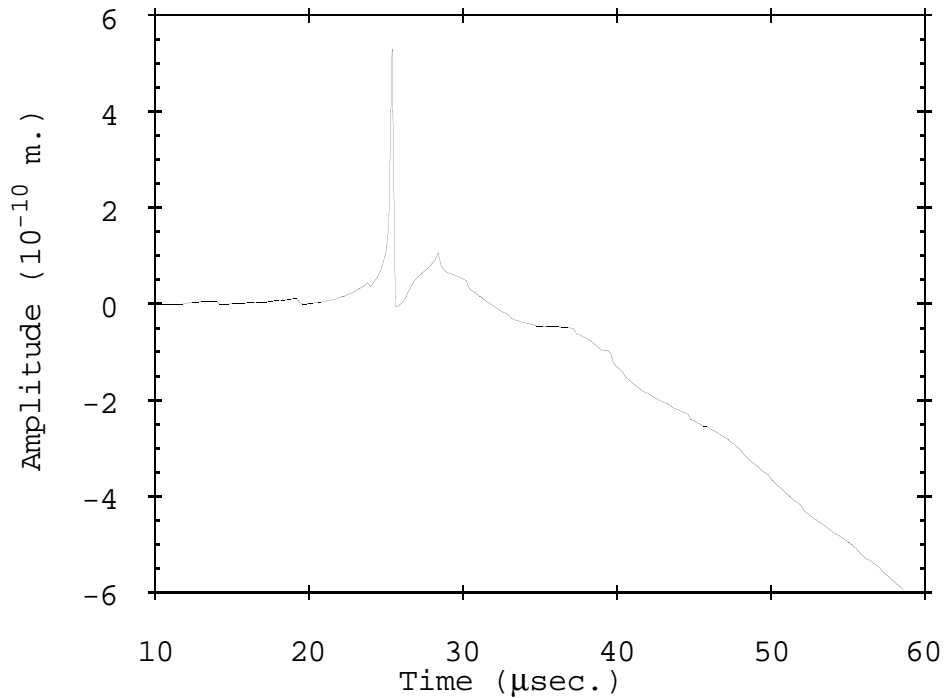
Figure 2.19   Theoretical plate surface displacement due to
point source step function loading at a distance
of 0.0762 m. on the same surface of the plate.

In order to compare the theoretical displacement with the
outputs of the transducers, the output of the program had to be nor-
malized in time and amplitude. The time shifting was necessary be-
cause of the small delay (several μsec.) in triggering the digitizer
in the experimental measurements. The computed signal was
normalized in time by shifting it until the peak of the Rayleigh wave
arrival coincided with the same peak on the experimental waveforms.
This peak was the largest of both of the signals and was thus
easily recognizable. The Rayleigh wave peak was not used in the am-
plitude normalizing, however. This was because of the sharp
risetime and thus high frequency components in the theoretical sig-
nal. This peak was not tracked well by any of the transducers. If
this peak were used, the details of the other arrivals could not eas-

ily be seen in the theoretical signal. The amplitude of the theoreti-
cal signal was scaled so that the first longitudinal arrival was
the same as that for the experimental signal.

In the case of the pinducer, the derivative of the theoretical
displacement was used for comparison. This was because of the veloci-
ty sensitivity of this sensor. The derivative was evaluated numeri-
cally with the Asyst software package. The theoretical velocity was
scaled to the experimental pinducer output in the same manner as that
used for the displacement comparisons of the other transducers.

The experimental outputs of the four sensors along with the nor-
malized theoretical outputs are exhibited in Figure 2.20 to Figure
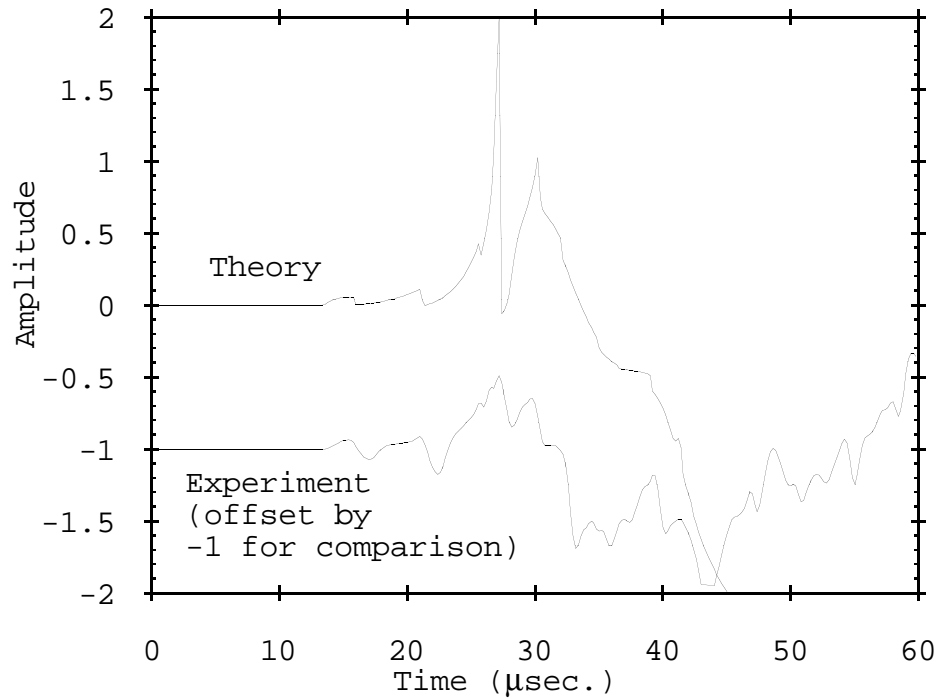
Figure 2.20   Theoretical prediction and experimental signal
              detected by ultrasonic sensor for lead break
              source on thick aluminum plate.

2.23. Since none of the transducers were able to reproduce accurately
the amplitude of the Rayleigh wave because of its impulsive nature,
all four plots are shown with an expanded amplitude scale in which
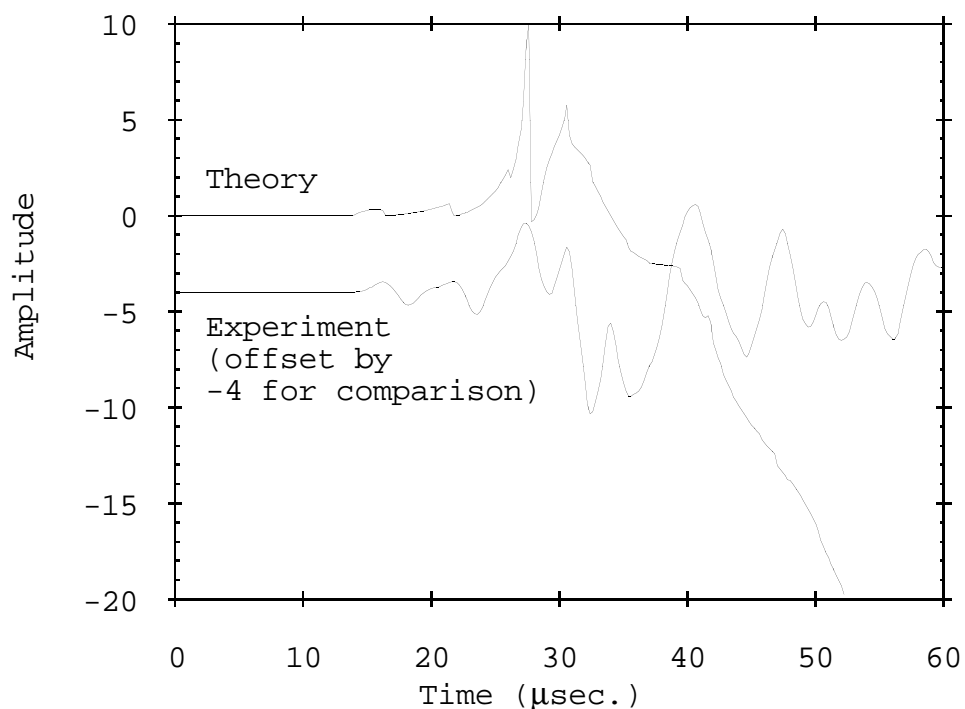
Figure 2.21   Theoretical prediction and experimental signal
              detected by R15 sensor for lead break source on
              thick aluminum plate.
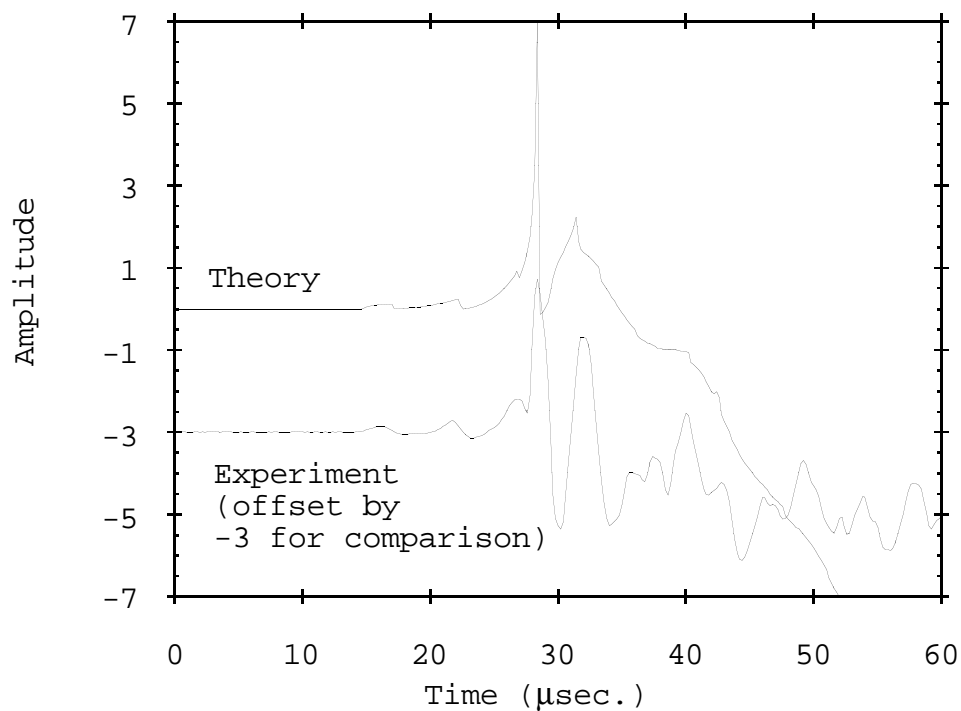
Figure 2.22   Theoretical prediction and experimental signal
              detected by S9208 sensor for lead break source
              on thick aluminum plate.
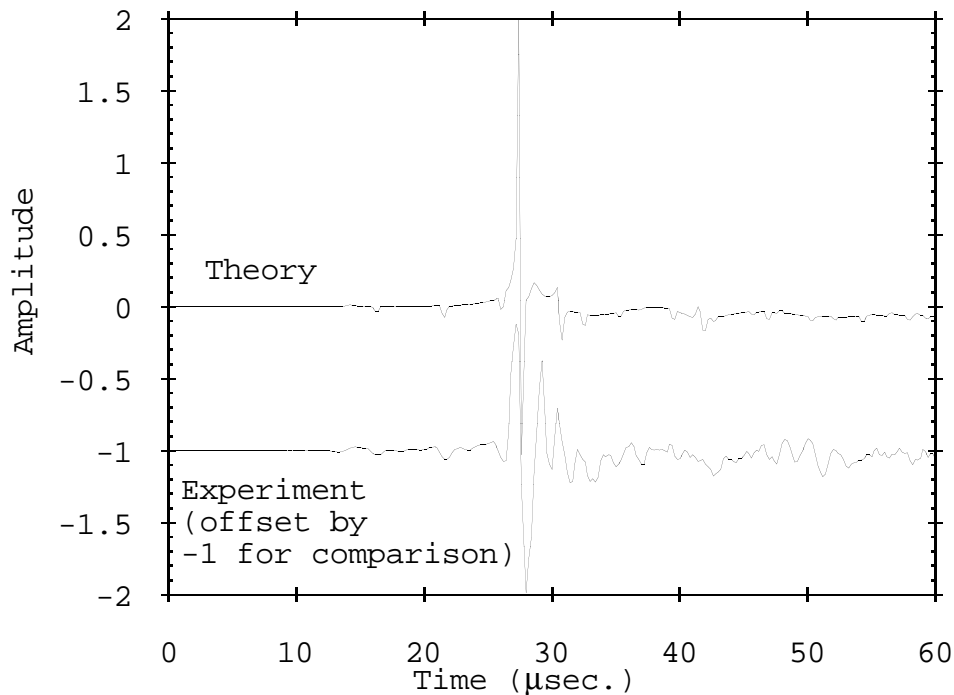
Figure 2.23   Theoretical prediction and experimental signal
detected by Pinducer for lead break source on
thick aluminum plate.

the peak of the Rayleigh wave is off scale and not shown. This allows

for a better comparison of the theory and experiment for the other

arrivals.

In the cases of the ultrasonic sensor, the R15, and the S9208, the

timing of the arrivals of the different waves seem to agree reason-

ably well with theory up until the arrival of the once reflected

shear wave (2S wave). The impulse nature of the Rayleigh wave and the

large 2S wave induce ringing in the sensors, particularly in the R15.

Additionally, theory predicts a long low frequency ramp downward af-

ter this 2S arrival caused by the interference of numerous other re-

flected and mode converted waves. This low frequency response is also

not captured by any of the sensors. These features cause the lack

of agreement between the theory and experiment after this point.

One further factor that causes the experiment not to agree with the

theory, particularly for the high frequency Rayleigh wave, is that the theoretical prediction is for a point detector. Except for the pinducer, all of the sensors have large areas of detection which cause phase cancellation across the face of the transducer for signals with wavelengths less than the diameter of the transducer. In the case of the low frequency plate waves that are studied later, this is less of a concern since the wavelengths are much larger.

The output of the pinducer also agrees reasonably well with the theoretical velocity prediction up until the arrival of the 2s wave. This demonstrated that it was indeed sensitive to velocity while the other three sensors were sensitive to the displacement.

As for a comparison of the different sensors, the R15 again gives the largest output and thus highest sensitivity. However, it shows the most ringing and the least accurate reproduction of theory. The S9208 and the ultrasonic sensor were comparable. The S9208 reproduced the Rayleigh wave slightly better, but demonstrated slightly less sharp details of the smaller earlier arrivals. The pinducer again yielded the smallest output.

In summary, these measurements demonstrated the velocity sensitivity of the Pinducer and the displacement sensitivity of the other three sensors. They allowed a relative comparison of the sensitivities and fidelities of the different sensors. This comparison again showed that the R15 provides the highest sensitivity at the expense of fidelity. The broad band S9208 and the ultrasonic sensor provided a more accurate reproduction of the theoretical signal. However, it is again stressed that these are only relative comparisons and not absolute calibrations.

II.4 Acoustic wave input generated by pencil lead break on thin aluminum plate and comparison with output from optical interferometer

The final transducer evaluation method was to compare the ouputs of the different sensors when the input was that of an acoustic wave in a thin aluminum plate generated by a pencil lead fracture. This input was similar to that investigated in the remainder of the research. The responses of the transducers were also compared to that of an optical interferometer which was known to be sensitive to the normal component of the surface displacement. This allowed a further demonstration of the displacement sensitivity and flat frequency response of the ultrasonic transducer. Similar comparisons of piezoelectric transducer outputs against that of an optical interferometer have been performed by Majerowicz [41] who investigated the effect of specimen geometry as well as detecting transducer on the measured waveforms.

Again, the same transducers were evaluated. The plate to which they were coupled was aluminum 2024 and again a silicone grease couplant was used. The plate was 0.635 cm. in thickness and had lateral dimensions of 38.1 cm. by 50.8 cm. The lead break source was positioned at the center of the plate. An R15 sensor was positioned next to the source and used to trigger the digitizer. The transducer and interferometer beam were positioned at a distance of 7.62 cm. from the source as shown in Figure 2.24. A preamplifier was again used to amplify the output of the transducers. The gain was 40 dB and no internal filter was used. The signals were digitized at a 5 MHz sampling frequency with the transient recorder and stored on the personal computer. A block diagram of the
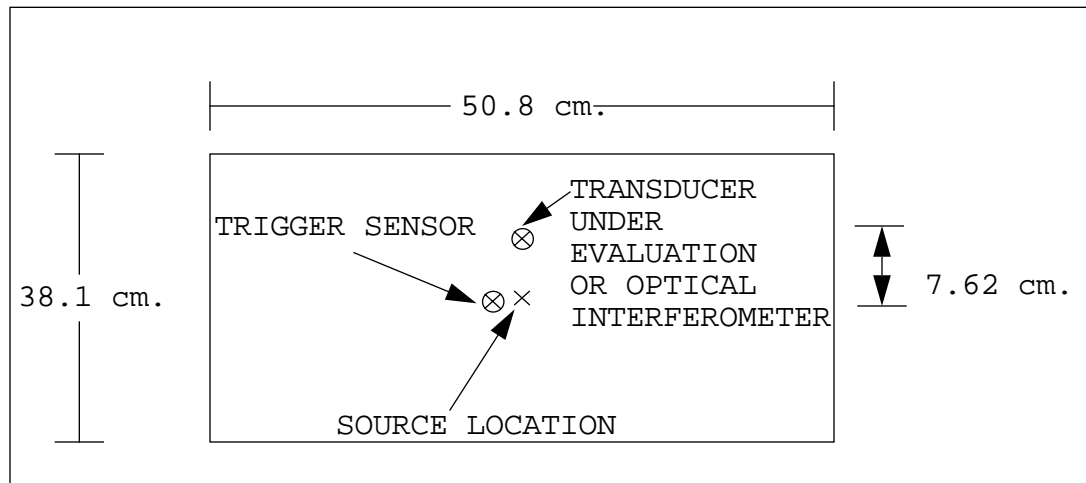
Figure 2.24   Source, trigger sensor, and transducer position-
ing for evaluation of transducer with simulated
AE source in thin aluminum plate.
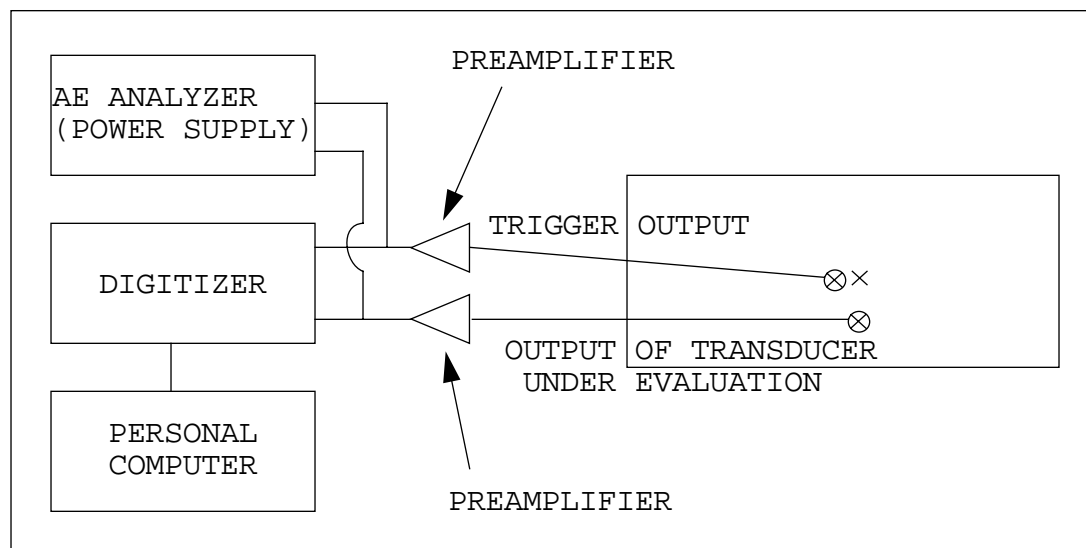
Figure 2.25   Experimental apparatus for evaluation of trans-
ducers with simulated AE source in thin aluminum
plate.

experimental apparatus is presented in Figure 2.25

The optical interferometer used was a prototype path stabilized

Michelson interferometer designed and built by Spicer et al. [42].

The design was based on that of Dewhurst et al. [43] for which the

basic elements are shown in a block diagram in Figure 2.26. Path sta-
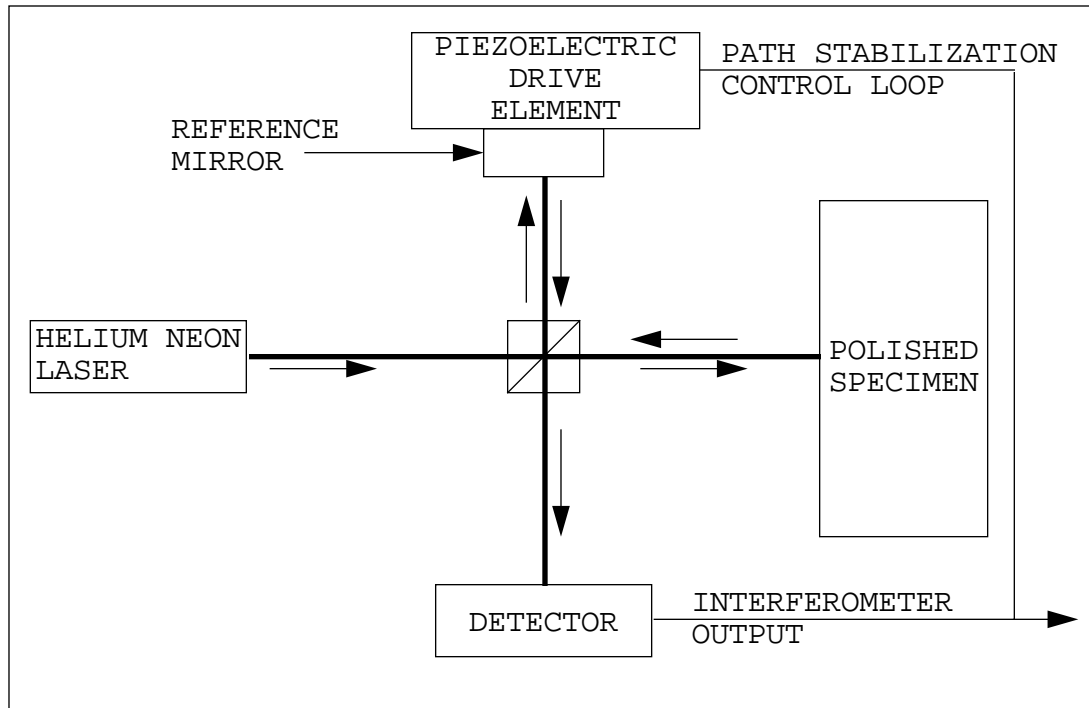
Figure 2.26   Block diagram of optical interferometer.

bilization was used to eliminate large low frequency optical path

length changes in the reference arm of the interferometer. These

low frequency effects are often much larger than the desired tran-

sient acoustic signals and are a result of environmental disturbances

such as building vibrations and refractive index variations. They are

generally less than 1 kHz in frequency. Path stabilization was accom-

plished by using the output signal from the interferometer to drive a

piezoelectric element mounted behind the reference mirror in a low

frequency feedback loop. This eliminated the low frequency environ-

mental effects. Above the low frequency used in the feedback loop

(about 1 kHz), the interferometer was reported to have a flat fre-

quency response to 50 MHz.

Displacement of the surface of the specimen by $\frac{1}{2}\lambda$ caused a

change in the optical path of 1λ which resulted in a shift of the

fringe pattern by 1 fringe. This shift of 1 fringe corresponded to a certain peak-to-peak voltage output from the interferometer depending on a number of factors including the input power of the laser, the sensitivity of the detector, and the reflectivity of the surface of the specimen. In practice, however, it was measured by examining the output of the interferometer when the specimen was subjected to large amplitude vibrations such as by lightly tapping it with a finger. Knowing the wavelength of the laser light, which was 633 nm. for the Helium-Neon laser used in this research, an absolute calibration factor in terms of volts/meter was determined. This calibration factor could, in theory, be used to convert the output of the interferometer into absolute surface displacement provided the amplitude of vibration is small enough for the interferometer to remain in its linear operating range.

Although a calibration factor was obtained, the method of inducing the acoustic wave used in this experiment prevented its application. In breaking the lead to generate the acoustic wave, the pencil was held by hand and the load was gradually increased until the lead fractured. The large vibrations of the unsteady hand loading the pencil caused the interferometer to jump several fringes. These vibrations were at frequencies higher than that corrected for by the path stabilization, but much lower than that of the acoustic transients caused by the lead breaks.

In previous absolute calibration experiments described by Eitzen et al. [13], a mechanical fixture was used to circumvent this problem. In this fixture, a screw was gradually tightened which applied load to the lead until it fractured. Such a fixture would have been useful in these measurements to eliminate these low frequency,

large amplitude vibrations created by the unsteady hand. However,

since such a fixture was not available, the low frequency

vibrations were eliminated from the signal by filtering the interfer-

ometer output with a 10 kHz high pass filter (Allen Avionics model

F2072). The insertion loss due to the filter would have had to be de-

termined and corrected for in order to apply the absolute calibration

factor. Also, there was uncertainty as to whether the

interferometer was always within its linear operating range due to

these large amplitude vibrations.

A plot of the wave detected by the ultrasonic transducer and the

interferometer is shown in Figure 2.27. In the signal from the ultra-
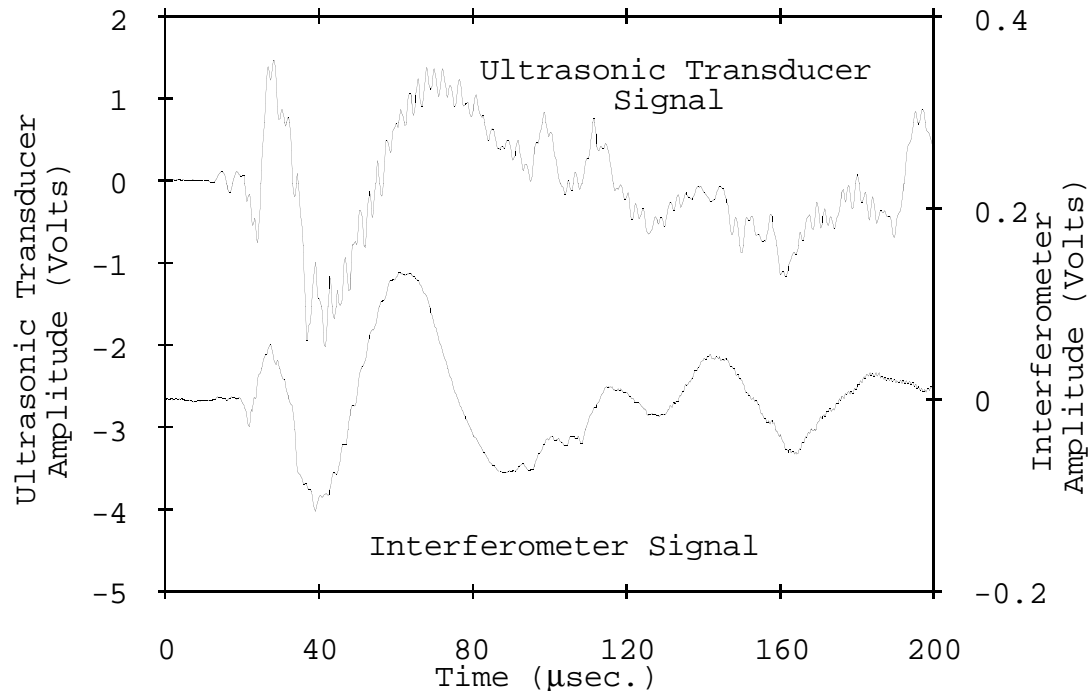
Figure 2.27   Simulated AE signal in thin aluminum plate de-
tected by ultrasonic transducer and optical in-
terferometer.

sonic transducer in this figure, the earliest wave arrival was that

due to the extensional plate mode. It is the small amplitude motion

seen arriving at about 10 μsec. The extensional mode was also visi-

ble in the interferometric signal although it was down in the noise

level. A view of these signals with an expanded amplitude and time

scale to more clearly show the extensional wave is presented in Fig-
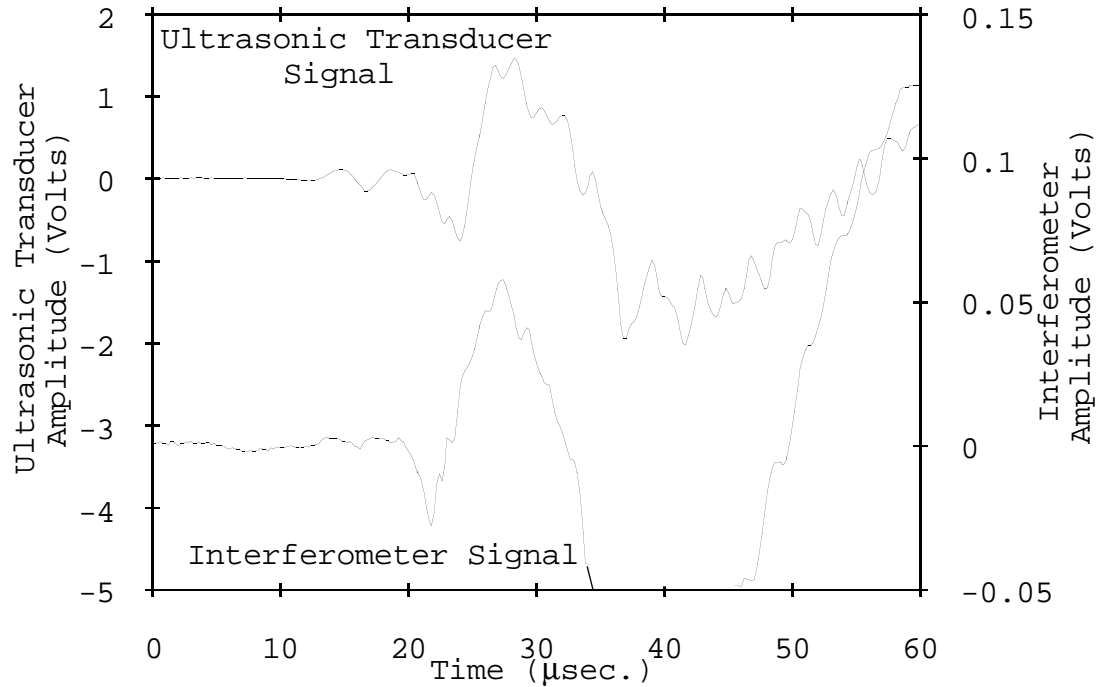
Figure 2.28   Simulated AE signal in thin aluminum plate de-
                  tected by ultrasonic transducer and optical in-
                  terferometer with expanded time and amplitude

ure 2.28. The large amplitude signal arriving after the extensional

mode at about 20 μsec. is that caused by the flexural plate mode.

This mode is dispersive with the higher frequencies traveling with

higher velocities. This is clearly seen in Figure 2.27. The in-

plane shear mode wave is not seen in the output of either sensor. The

first reflection of the flexural mode from a lateral boundary appears

to arrive at about 90 μsec. in both signals of this figure. The high

frequency, small amplitude ripple seen, particularly on the ultrason-

ic transducer output, is of undetermined origin. It may be the result

of higher order plate modes.

A detailed analysis of the propagation of these plate modes is

presented in a later section of this work. For the present, it was only of interest to compare the outputs of the sensors with that of the displacement sensitive interferometer. The ultrasonic transducer reproduced the output of the interferometer very well up to about 80 μsec. with the exception of its increased sensitivity to the high frequency ripple. The discrepancy between the two signals for the low frequencies arriving after this time is believed to have been caused by phase shifting and filtering by the 10 kHz high pass filter on the interferometric signal. Supporting this conclusion was the fact that the higher frequency signals caused by the reflection of the flexural wave that occurred during this same time period were in agreement in both signals. There were two additional factors that may have caused any discrepancy between the observed waveforms. The first was that of positioning errors in placing the sensors. The other was that of the point detection of the interferometer as opposed to the large sensing area of the transducer. However, at the large wavelengths of these low frequency plate waves, the latter factor was not a concern.

The output of the R15 transducer along with that of the interferometer are plotted in Figure 2.29. This figure clearly demonstrates the resonant behavior of the R15 sensor. Except for the small extensional wave and the first half cycle of the flexural wave, no agreement is seen between the output of this sensor and that of the interferometer. The output of the R15 is, of course, higher indicating its better sensitivity, but the reproduction of the actual signal is quite poor.

The signals from the S9208 and the interferometer are presented in Figure 2.30. Again, up until about 60 μsec., the output of the S9208
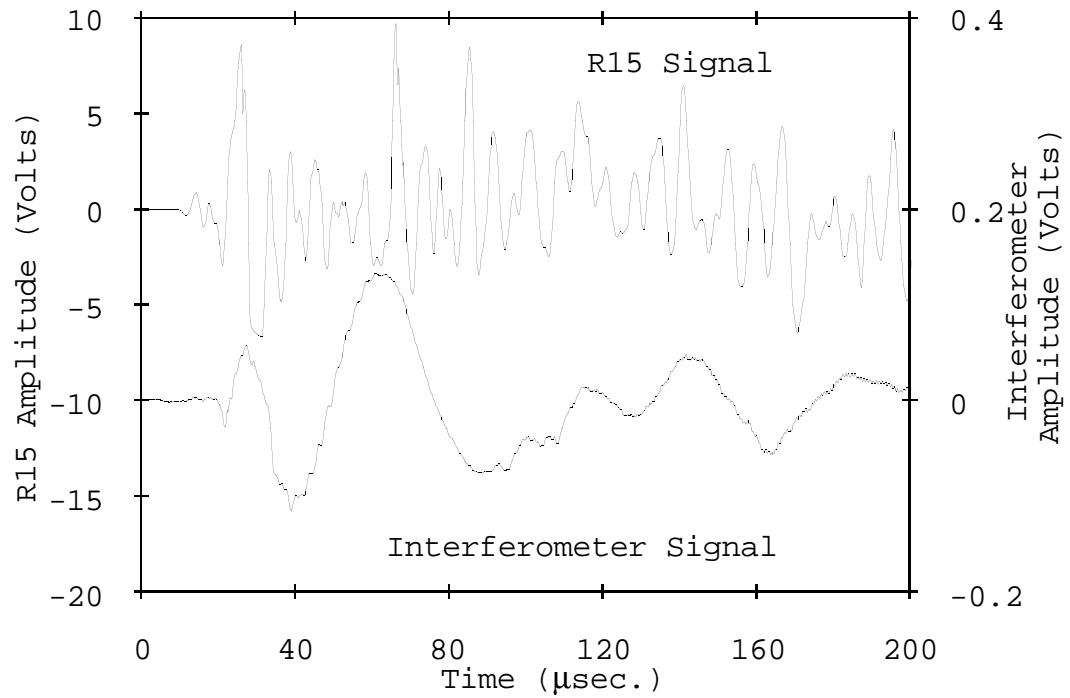
Figure 2.29   Simulated AE signal in thin aluminum plate detected by R15 transducer and optical interferometer.
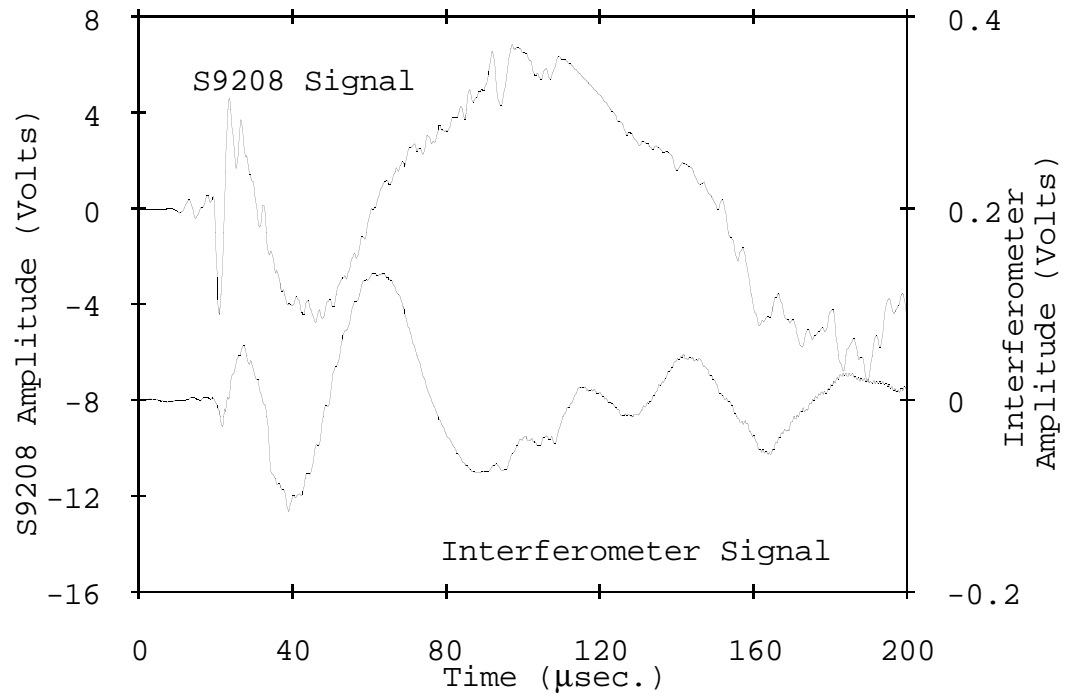
Figure 2.30   Simulated AE signal in thin aluminum plate detected by S9208 transducer and optical interferometer.

corresponds well with that of the interferometer. Beyond this time,

the same problem occurs as was discussed when comparing the results

of the interferometer to the ultrasonic transducer. That is, the ef-

fects of the 10 kHz high pass filter alter the interferometer signal.

In this case, however, the reflection of the flexural wave is some-

what obscured in the S9208 signal because of its higher sensitivity

to low frequencies. The output of the pinducer is shown in Figure
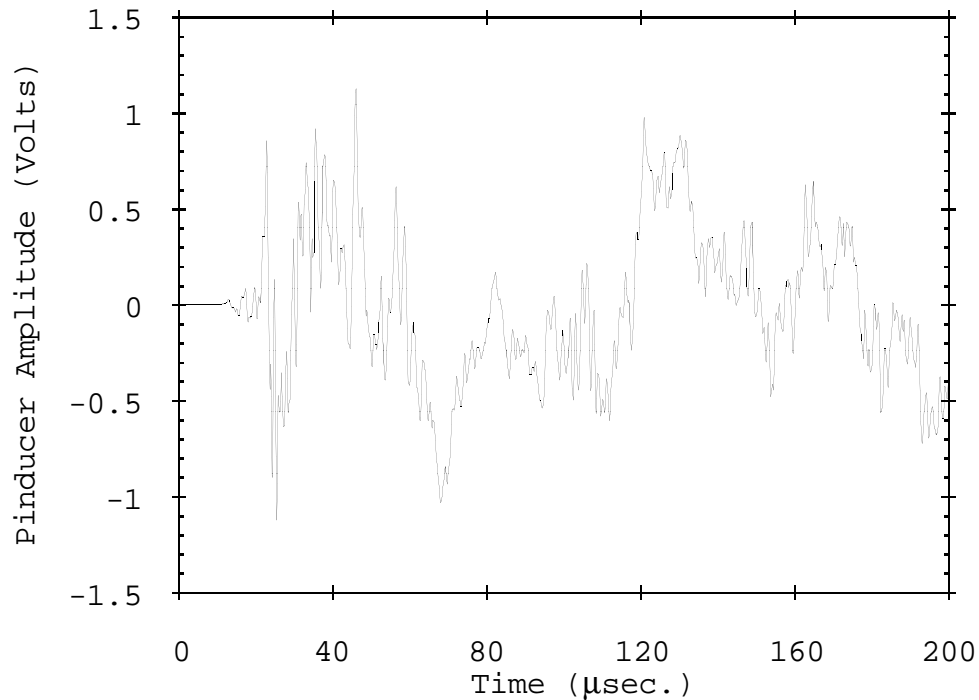
Figure 2.31   Simulated AE signal in thin aluminum plate de-
tected by Pinducer transducer.

2.31. It was not compared to the signal from the interferometer as no

agreement was expected because of its velocity sensitivity.

   In summary, these measurements provided additional relative evalu-

ations of the performance of the different transducers. The ultrason-

ic transducer was shown to provide an output consistent with that

of a displacement sensitive optical interferometer when both were ex-

cited by the plate mode acoustic waves. The drastic resonant behavior

of the R15 sensor was again clearly demonstrated.

II.5 Summary and Conclusions.

This set of experiments provided a means to evaluate the performance of four types of acoustic transducers and yielded relative comparisons of their behavior. The 3.5 MHz broad band ultrasonic transducer demonstrated superior frequency response over the bandwidth of interest (20 kHz to 1.5 MHz) and thus should provide higher fidelity reproductions of AE signals. Its response was demonstrated to be proportional to the displacement in this frequency range. The S9208 was also displacement sensitive and its peak sensitivity was slightly higher than that of the ultrasonic transducer. However, it was shown to have more resonant behavior than the ultrasonic transducer.

The resonant R15 sensor had a significantly higher peak sensitivity, but it was achieved at the expense of its frequency response. The pinducer offered much lower sensitivity which was probably due to its smaller active area. In addition, it was shown to be sensitive to the velocity of the surface.

In applications such as simple, conventional AE testing where high output sensitivity is necessary, the R15 sensor is ideal. However, for quantitative signal analysis and interpretation, the ultrasonic transducer seems to be a better choice. Thus, it was used in the investigations of plate mode propagation that are discussed next.

III. Plate Wave Propagation in Aluminum Plates

III.1 Introduction

The next area of investigation in this research was that of plate wave propagation in isotropic 2024 aluminum plates. Numerous references to this subject are given in Chapter I. This work was performed in order to better understand the propagation of AE pulses in isotropic media before attacking the more formidable problem of plate waves in highly anisotropic composite materials. The investigation of plate waves in aluminum focussed on two areas. The first was a further evaluation of the effect of source orientation on plate modes to include sources other than those normal to the plate surface or plate edge. The in-plane displacement component was also measured for the sources at different angles. This component of displacement was not reported in the previous study demonstrating the effects of source orientation by Gorman [35].

The second area of investigation of plate modes in isotropic materials centered on the calculation of the shape of the flexural mode wave. The classical plate theory bending equation of motion was solved for the case of a normal point force, step function unloading on a finite plate. A normal mode approach was used for this solution and the results of these theoretical predictions were compared with signals generated by a pencil lead break. The lead break provided a source similar to a step function. These theoretical predictions are the first known attempts to predict the AE response in a finite plate with an analytical solution. All previous work in quantitative predictions of AE signals in plates has been for the case of plates of infinite lateral extent.

III.2 Classical plate theory

The theory for the propagation of plate waves is based on the ex-
act elasticity equations which were used to predict the response of a
thick, infinite plate in the last chapter, but a number of assump-
tions about the geometry and the type of deformation are made which
allow much more simplified equations of motion to be derived. These
equations describe the lowest order symmetric or extensional mode and
the lowest order antisymmetric or flexural mode as well as the in-
plane shear mode. This theory is known as classical plate theory.
In this section, only the case of a homogeneous, isotropic plate is
considered. In the next section on composites, the plate equations of
motion will be extended to the case of a homogeneous, orthotropic ma-
terial.

The coordinate axes of the plate are chosen such that the x and
y axes are in the midplane of the plate. The z axis is normal to
the plate with its origin at the center of the plate as shown in Fig-
ure 3.1. The displacements are u, v, and w which are along the x,
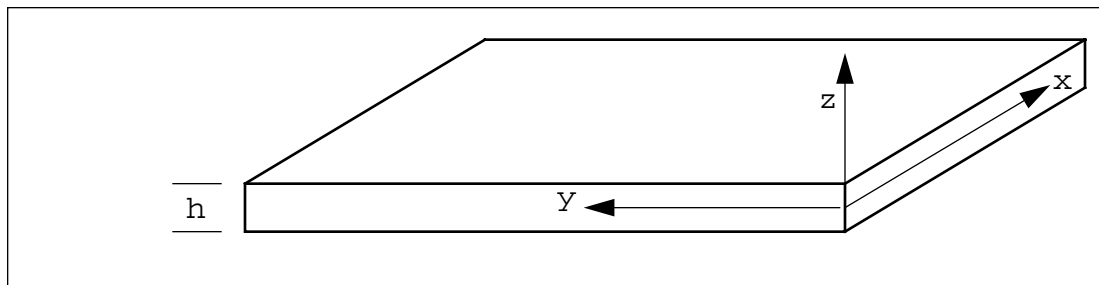
Figure 3.1   Coordinate axes of plate.

y, and z axes respectively. The deformation of the material is
again assumed to be small so that the definition of strain given in

Eq. 2.7 remains valid. The plate is assumed to be very thin and under the condition of plane stress. For the case of plane stress, $\sigma_{xz} = \sigma_{zx} = \sigma_{yz} = \sigma_{zy} = \sigma_{zz} = 0$. These conditions are substituted into the first two equations of motion given in Eq. 2.9 to yield the equations of motion for the in-plane stresses. These equations are

$$\frac{\partial \sigma_{xx}}{\partial x} + \frac{\partial \sigma_{xy}}{\partial y} + \rho f_x = \rho \frac{\partial^2 u}{\partial t^2} \qquad \text{Eq. 3.1}$$

and

$$\frac{\partial \sigma_{xy}}{\partial x} + \frac{\partial \sigma_{yy}}{\partial y} + \rho f_y = \rho \frac{\partial^2 v}{\partial t^2} \quad . \qquad \text{Eq. 3.2}$$

For an isotropic material under the condition of plane stress, the generalized Hooke's law relations are given by

$$\sigma_{xx} = \frac{E}{(1 - v^2)} \varepsilon_{xx} + \frac{Ev}{(1 - v^2)} \varepsilon_{yy} \quad , \qquad \text{Eq. 3.3}$$

$$\sigma_{yy} = \frac{Ev}{(1 - v^2)} \varepsilon_{xx} + \frac{E}{(1 - v^2)} \varepsilon_{yy} \quad , \qquad \text{Eq. 3.4}$$

and

$$\sigma_{xy} = \sigma_{yx} = \frac{E}{(1 + v)} \varepsilon_{xy} \qquad \text{Eq. 3.5}$$

where E is the Young's modulus of elasticity and v is the Poisson's ratio. These are a different set of elasticity coefficients for iso-

tropic materials and are related to the previously used Lame' coeffi-
cients by

$$E = \frac{\mu\,(3\lambda + 2\mu)}{(\lambda + \mu)}$$

Eq. 3.6

and

$$\nu = \frac{\lambda}{2\,(\lambda + \mu)} \quad .$$

Eq. 3.7

Substituting the definition of stress, followed by the
definition of strain into the equations of motion and simplifying
yields the equations of motion for in-plane displacements for a thin,
isotropic, homogeneous, linear elastic plate under plane stress.
These are

$$\frac{E}{(1 - \nu^2)}\left(\frac{\partial^2 u}{\partial x^2} + (1 + \nu)\frac{\partial^2 v}{\partial x \partial y} + \left(\frac{1 - \nu}{2}\right)\frac{\partial^2 u}{\partial y^2}\right) + \rho f_x = \rho\frac{\partial^2 u}{\partial t^2}$$

Eq. 3.8

and

$$\frac{E}{(1 - \nu^2)}\left(\frac{\partial^2 v}{\partial y^2} + (1 + \nu)\frac{\partial^2 u}{\partial x \partial y} + \left(\frac{1 - \nu}{2}\right)\frac{\partial^2 v}{\partial x^2}\right) + \rho f_y = \rho\frac{\partial^2 v}{\partial t^2} \quad .$$

Eq. 3.9

These equations govern the propagation of the extensional and
the in-plane shear (SH) plate waves. Since the in-plane shear mode
wave has not been observed in the AE signals of interest in this
work, it is not discussed further. In order to gain insight into

how an extensional wave propagates, it is next assumed that the body forces, f_x and f_y, are zero and that a sinusoidal plane wave is propagating along the x axis with particle displacement in the x direction. Its displacement is given by

$$u = A_0 e^{i(\omega t - kx)}$$
<div align="right">Eq. 3.10</div>

and

$$v = 0$$
<div align="right">Eq. 3.11</div>

where A_0 is the amplitude, ω is the angular frequency in radians/ sec., k is the wave number, and i is the imaginary number which is equal to $\sqrt{-1}$. The wave number is related to the wavelength, λ, by $k = \dfrac{2\pi}{\lambda}$. Also, the angular frequency, ω, is related to the frequency (f in Hz) by $\omega = 2\pi f$. The phase velocity, c, can be expressed in terms of k and ω as

$$c = \frac{\omega}{k} \; .$$
<div align="right">Eq. 3.12</div>

After substituting Eq. 3.10 and Eq. 3.11 into the equations of motion, Eq. 3.8 and Eq. 3.9, and solving for the phase velocity, the following expression is derived,

$$c_e = \sqrt{\frac{E}{\rho(1-v^2)}}$$
<div align="right">Eq. 3.13</div>

where c_e is used to designate the extensional plate mode velocity.

Eq. 3.13 is the velocity equation or dispersion relation for exten-
sional mode waves. It predicts that this mode of propagation
travels with a constant velocity that is independent of frequency.

It is demonstrated later that the velocity of the flexural mode
does suffer dispersion. In other words, the velocity of each frequen-
cy component is dependent on frequency. Furthermore, it is noted here
that the exact theory of elasticity predicts that the lowest order
symmetric mode also suffers dispersion. Remember, however, that the
previously presented equations for extensional plate modes were not
those of exact elasticity theory, but assumptions were made concern-
ing the displacements. The assumption that the material was thin
was used so that the condition of plane stress could be applied. In
the range of plate thicknesses for which this assumption is valid,
these equations do agree with the exact theory and provide a valid
description of the extensional or in-plane motion of the plate.

The thin plate criterion is often expressed in terms that the
wavelength must be greater than some number of plate thicknesses.
Medick [34] used the criterion that the wavelength must be sixteen
times the plate thickness in his study of flexural wave
propagation. However, this number was arbitrarily chosen based on the
agreement of classical plate theory predictions and his
experimental data. Using the relationship between velocity, frequen-
cy, and wavelength, the thin plate criterion can also be expressed as
a maximum frequency at which the classical plate theory is valid.

The derivation of the classical plate theory equation of motion
for the flexural mode of propagation for an isotropic plate is well
known and widely documented. For this reason, the derivation is not
reproduced here, but the reader is referenced to an excellent presen-

tation of this derivation by Graff [31]. The derivation of the flex-
ural equation of motion for an orthotropic plate is presented in
the next chapter on composite materials.

The assumptions used to derive this equation of motion include all
of those used to derive the extensional equations of motion. Further-
more, the plate is assumed to be under a state of pure bending in
which plane sections of the plate remain plane and perpendicular to
the midplane of the plate. The effects of rotary inertia are also ne-
glected. Based on these assumptions, the equation of motion for the
flexural mode in terms of the displacement, w, and the bending stiff-
ness, D which is given by,

$$D = \frac{Eh^3}{12\,(1 - v^2)}$$

<div align="right">Eq. 3.14</div>

is found to be

$$D\nabla^4 w\,(x,y,t) + \rho h\frac{\partial^2 w\,(x,y,t)}{\partial t^2} = q\,(x,y,t)$$

<div align="right">Eq. 3.15</div>

where q(x,y,t) is the normal component of the body forces or a con-
centrated normal surface load, h is the plate thickness, and ∇^4 is
the Laplacian of the Laplacian or the biharmonic operator. In Carte-
sian coordinates, this is

$$\nabla^4 w = \nabla^2\nabla^2 w = \left(\frac{\partial^2}{\partial x^2} + \frac{\partial^2}{\partial y^2}\right)\left(\frac{\partial^2 w}{\partial x^2} + \frac{\partial^2 w}{\partial y^2}\right)$$

<div align="right">Eq. 3.16</div>

which can be simplified to

$$\nabla^4 w = \frac{\partial^4 w}{\partial x^4} + 2\frac{\partial^4 w}{\partial x^2 \partial y^2} + \frac{\partial^4 w}{\partial y^4} \quad . \qquad \text{Eq. 3.17}$$

To examine the dispersion behavior, it is again assumed that there are no body forces present and that a harmonic plane wave is propagating along the x direction. The displacement is given by

$$w = A_0 e^{i(\omega t - kx)} \quad . \qquad \text{Eq. 3.18}$$

Substituting this into the equation of motion (Eq. 3.15) and reducing terms yields the dispersion relation

$$c_f = \sqrt[4]{\frac{D}{\rho h}}\sqrt{\omega} \qquad \text{Eq. 3.19}$$

in which c_f is used to denote the flexural velocity. This equation demonstrates that the flexural mode is dispersive with a square root dependence on the frequency of the wave.

According to this dispersion relation, the velocity of the flexural mode increases with increasing frequency. One problem is immediately noticed. That is, the velocity increases without bound. This, of course, is not physically possible. It is caused by the assumptions made in deriving the classical equation of motion. Again, for thin plates and low frequencies where these assumptions are valid, the predicted flexural behavior is valid and would agree with that predicted by the exact theory.

III.3 Source orientation effects

In the previous investigation of plate waves in aluminum and composite plates by Gorman [35], measurements were made of the out-of-plane displacement component of plate wave AE signals produced by lead break sources. The source orientations investigated were those with the source normal to the plate surface and with the source normal to one edge of the plate. It was discovered that the out-of-plane displacement component for the case of a lead break normal to the plate surface contained a large flexural mode signal and a small extensional mode signal. When the source was normal to the plate edge, the out-of-plane displacement component of the extensional mode was large while that of the flexural mode was almost nonexistent.

These results make intuitive sense when the direction of the source motion is considered. When the lead break is normal to the surface of the plate, the majority of the displacement due to the source motion is also normal to the plane of the plate resulting in flexural motion. However, because of the Poisson effect, there is still a small in-plane deformation caused by this source which generates the small extensional component observed. The reverse should be true when the source is normal to the edge of the plate. Based on these results, it was proposed that characterization of actual AE signals in terms of plate waves may be useful in determination of the source type or orientation.

To investigate this effect further, signals were generated by lead break sources in aluminum plates at angles in addition to normal to the plate surface (90 degrees) and normal to the plate edge (0 degrees). Sources were excited at the intermediate angles of 30 and

60 degrees. This was accomplished by breaking the lead on specially machined slots in the plate which were described by Gorman and Prosser [44] and are detailed below. Additionally, the in-plane displacement component was measured by placing a transducer on the opposite edge of the plate.

Four plates were used in this study, all of which were aluminum 2024. The dimensions of the first three plates were 0.508 m. in width, 0.381 m. in length, and 0.00635 m. in thickness. The fourth plate had the same thickness, but was only 0.254 m. in length and width. The first of the three plates which were identical in size, contained no slot and was used in the study of sources at 90 degrees. The second and third plates contained slots that allowed the lead break source to be at 30 and 60 degrees respectively, with respect to the plane of the plate. For the 30, 60, and 90 degree breaks, the source was located at the center width of the plate and at a length of 0.127 m. from the plate edge. A R15 sensor was positioned next to the source location and used to trigger the transient recorder. The out-of-plane displacement sensor which was a 3.5 MHz ultrasonic transducer was positioned on the surface of the plate at the center width at a distance of 0.127 m. from the source location. The in-plane sensor which was another 3.5 MHz ultrasonic transducer, was coupled to the opposite edge of the plate at the center width. Thus, it was 0.254 m. from the source location. The positioning of the source, slot, and transducers relative to the plate are illustrated in Figure 3.2.

For the 0 degree source break, the lead was broken on one edge of the fourth plate at the center width. The out-of-plane sensor was positioned at the center width at a distance of 0.127 m. from the

IN-PLANE
DISPLACEMENT
SENSOR

OUT-OF-PLANE
DISPLACEMENT
SENSOR

TRIGGER
SENSOR

SOURCE AND SLOT
LOCATION

0.127 m.

0.127 m.

0.127 m.

0.254 m.

0.508 m.
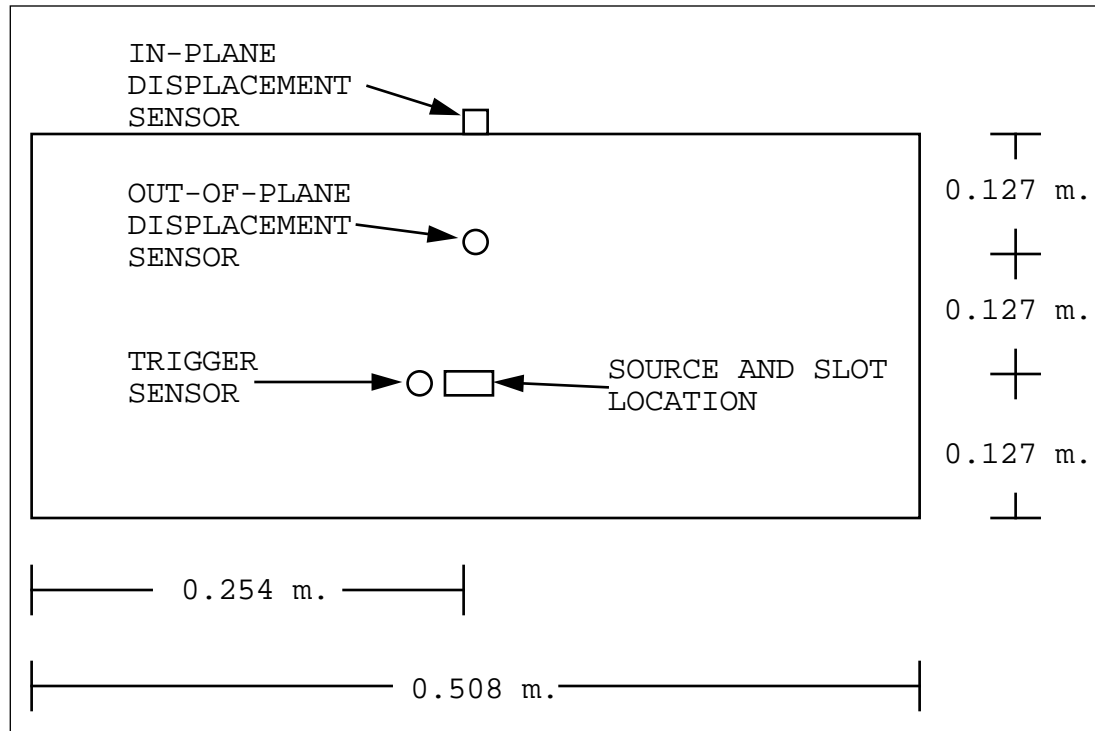
Figure 3.2   Plate dimensions and positioning of sensors and
source.

source. The in-plane displacement sensor was placed at the center
width on the opposite edge of the plate and was thus 0.254 m. from
the source. This smaller plate allowed the distance of propagation
for the in-plane displacement component of the wave created by the
0 degree source to be the same as used for the other source angles.

The 30 and 60 degree slots were 0.0127 m. in width and were ma-
chined to a depth of half of the plate thickness (0.003175 m.). The
length of the slot was then determined by the desired angle of the
slot with respect to the plane of the plate. A cross sectional view
along the center of the plate illustrating the slot and transducer
positions is shown in Figure 3.3.

The resulting signals from the in-plane and out-of-plane displace-
ment sensors were preamplified by 40 dB. The preamplifier contained a
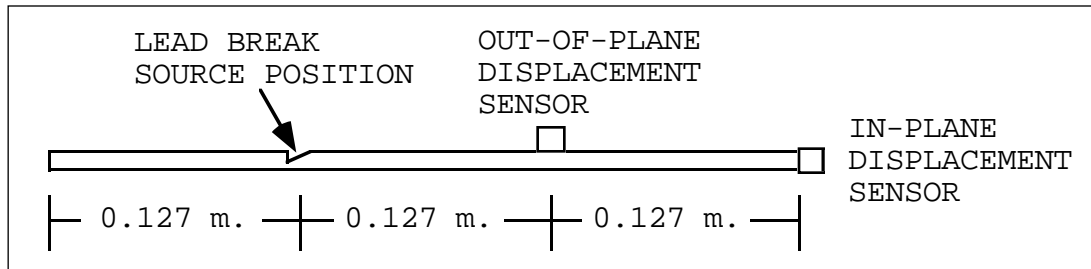
Figure 3.3   Cross sectional view of plate and slot illustrat-
ing transducer positions.

20 kHz high pass filter for these measurements. The amplified signals

were digitized at a 5 MHz sampling frequency on the transient record-

er. The digitized waveforms were stored on the personal computer

for later analysis and display. A block diagram of the experimental

apparatus is presented in Figure 3.4. At each source angle, the break
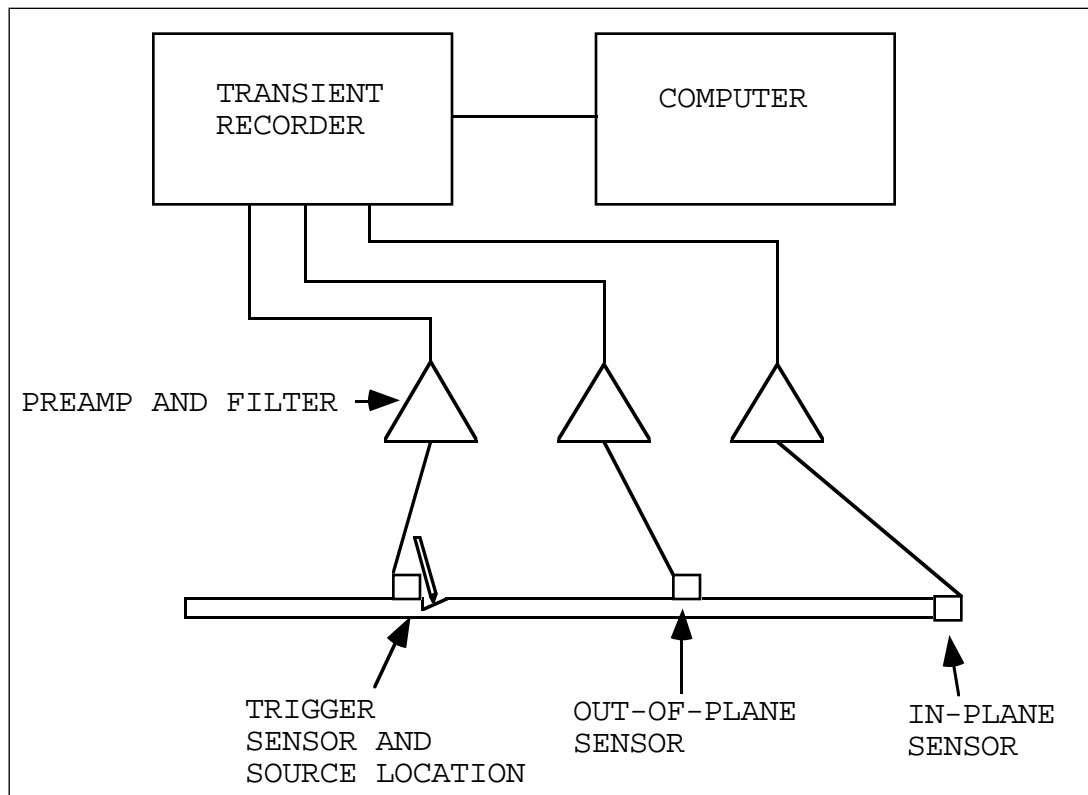
Figure 3.4   Experimental apparatus for measurements of the
effects of source orientation on plate waves.

was repeated ten times to determine the variability of the

magnitude of the step unloading force applied to the plate.

A typical out-of-plane displacement waveform due to a lead break

source on an aluminum plate is shown in Figure 3.5. The extensional
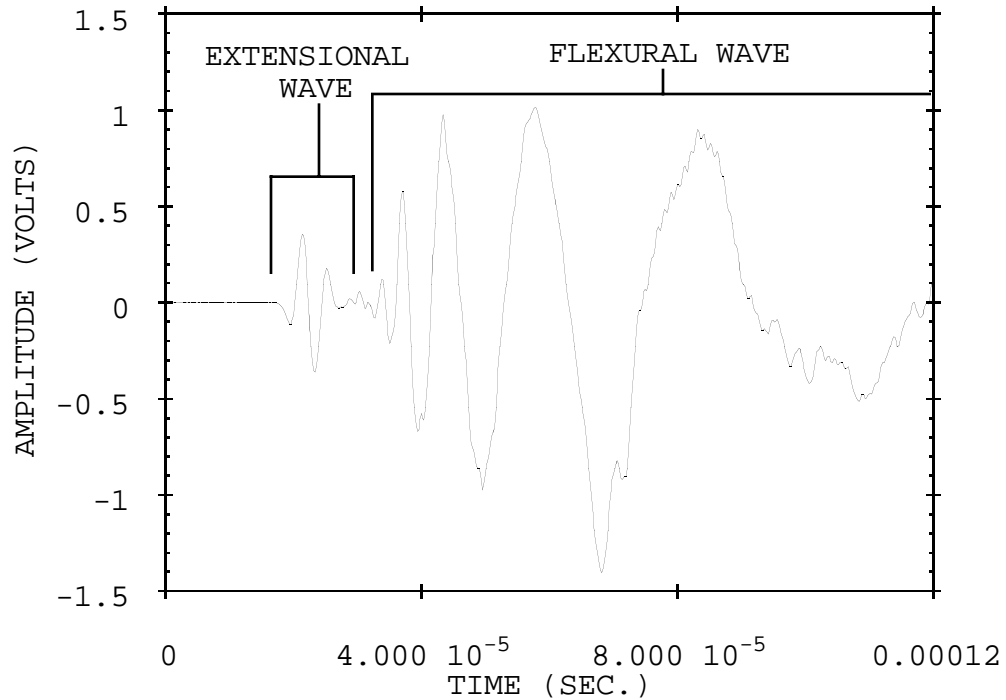
Figure 3.5   Typical out-of-plane displacement component for
a lead break source in an aluminum plate indicat-
ing the flexural and extensional plate modes.

and flexural modes are identified in this figure. The velocities of

the two modes were determined previously by measuring the arrival

times at different distances. The measured velocities agree with

those predicted by theory which confirms that these are indeed the

plate modes. This waveform was detected by the broad band

ultrasonic transducer. When a typical narrow band resonant AE trans-

ducer such as the R15 is used, the two modes are indistinguishable

because of the ringing in the transducer.

The out-of-plane displacement components of the waves created by

lead breaks at the four source angles are plotted in Figure 3.6.
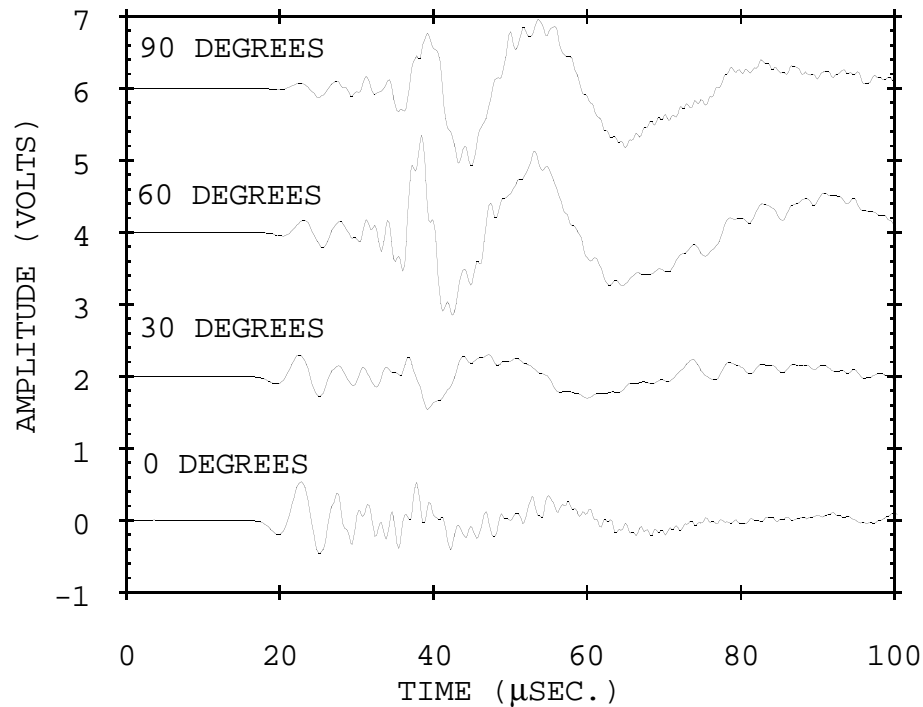
Figure 3.6   Out-of-plane displacement components for waves
generated at different source angles. Each wave-
form is offset by two volts to allow comparison.

The waveform shown at each angle was from a lead break that

produced a signal with a peak amplitude nearest the average peak am-

plitude for the ten breaks. For the source motion in the plane of the

plate (0 degree or edge break), it can be seen that the extensional

mode has its largest peak amplitude while the flexural mode has its

minimum. As the source angle increases, the extensional mode peak am-

plitude decreases. For increases in source angle toward normal to the

plate, the flexural peak amplitude increases except for the 60 to

90 degree cases where the 60 degree flexural amplitude is slightly

larger than that of the 90 degree break. At present it is unknown why

this anomaly occurred but, it is being investigated further.

   The average peak amplitudes of the out-of-plane displacement com-

ponents of the flexural and extensional modes are plotted versus

source angle in Figure 3.7. The standard deviations of the ten mea-
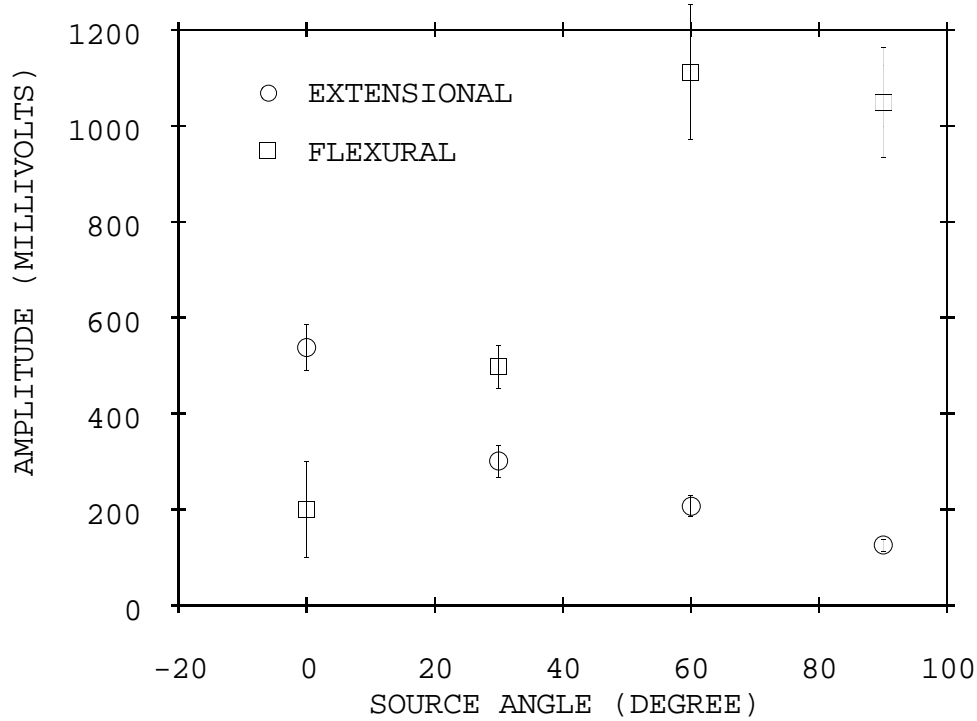
Figure 3.7   Average peak amplitudes of out-of-plane exten-
sional and flexural modes for sources at differ-
ent angles. The error bars are +/- one standard
deviation.

surements are plotted as the error bars in this figure. The increas-

ing amplitudes of the flexural mode and decreasing amplitudes of

the extensional mode with increasing source angle are as expected ac-

cording to the argument used previously regarding the direction of

source motion. At the intermediate angles of 30 and 60 degrees, the

amount of source motion in the plane and out of the plane of the

plate is proportional to the appropriate vector component of the

source force. Thus as the angle increases, there should be an in-

creasing flexural mode and decreasing extensional mode which is as

observed.

Examples of the in-plane displacement components for the four

source angles are shown in Figure 3.8. Again, it is pointed out

that the 0 degree measurement was made on a separate plate with a
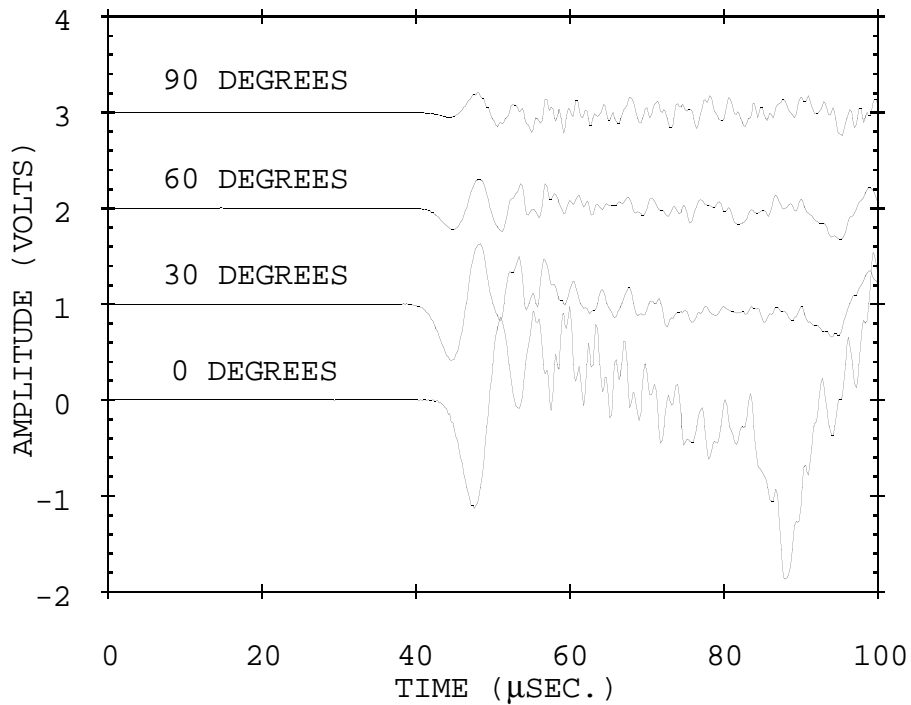
Figure 3.8   In-plane displacement components for waves gener-
               ated at different source angles. Each waveform
               is offset by one volt to allow comparison.

length of 0.254 m. to maintain a constant source to receiver dis-

tance. In these waveforms, the extensional amplitude again

decreases with increasing source angle. However, it is interesting

that the in-plane component of the flexural mode is not detected even

for large source angles where it should be largest. Recall that the

out-of-plane component of the extensional mode is observed for all

source angles. The average in-plane peak amplitudes of the extension-

al mode versus source angle is plotted in Figure 3.9. The standard

deviation is again indicated by error bars.

    These measurements confirmed the previous results by Gorman [35]

that the orientation of an AE source has an effect on plate modes

in thin plates. Furthermore, it was demonstrated that this effect oc-

curred at source angles other than normal to the plate (90 degrees)

and normal to the plate edge (0 degrees). The effect of source orien-
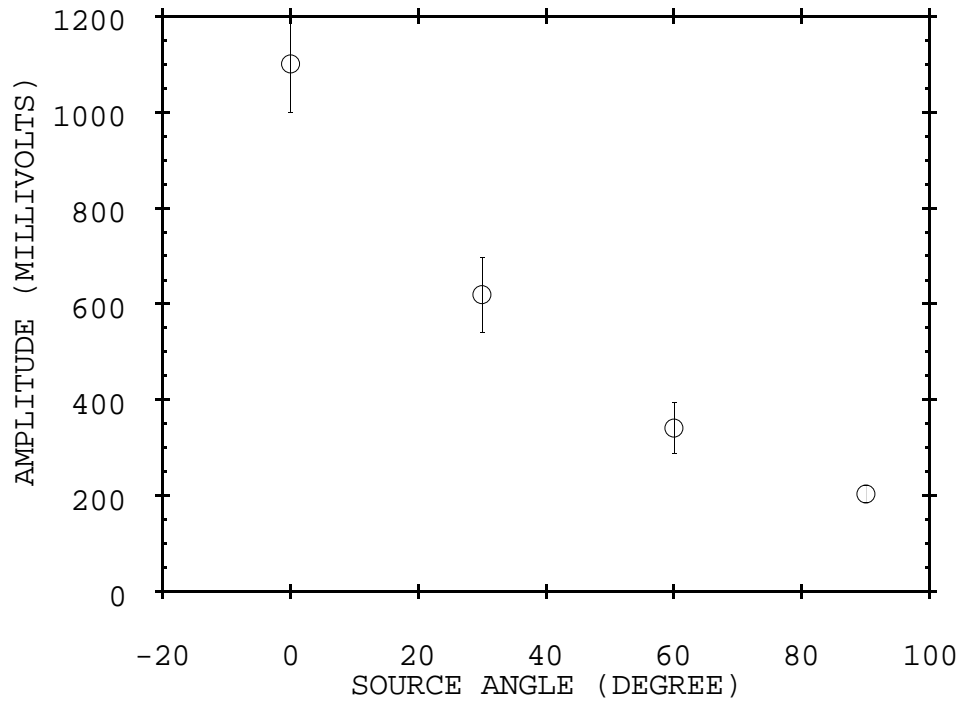
Figure 3.9   Average peak amplitudes of the in-plane exten-
              sional mode for sources at different angles. The
              error bars are +/- one standard deviation.

tation was also observed on the in-plane component of the displace-

ment of the plate modes.

Thus, it is expected that quantitative source information can be

obtained by the measurement of the amplitudes of the components of

the plate modes due to real sources. One example of interest will

be the case of impacts, particularly hypervelocity impacts which

are a concern to spacecraft such as the proposed space station. Mea-

surements of the amplitudes of the plate modes should allow determi-

nation of the angle of the impact and the energy of the impact

which will allow a better estimate of damage.

III.4 Prediction of the flexural mode by a normal mode solution

In order to better understand the propagation of AE plate wave

signals and the applicability of classical plate theory, theoretical predictions of the displacement of the flexural mode were made. The predictions were based on a normal mode expansion technique which was described by Gorman and Prosser [45] and is presented below. This solution technique was applied to the classical flexural equation of motion. The advantages of this approach are that it allows the solution to be obtained for the case of finite plates and is easily adaptable to the case of anisotropic media which is demonstrated in the next chapter. Furthermore, it is computationally much less intensive than solutions based on exact theory which are available only for infinite plates.

The results obtained by this approach were compared with predictions for an infinite plate based on an integral transform solution to the same classical flexural equation of motion. This comparison should demonstrate agreement up until the point at which reflections begin to occur in the normal mode solution. The predictions for the finite plate were also compared with experimental measurements. The experimental waveforms were generated by pencil lead breaks normal to the surface of the aluminum plate.

The normal mode expansion technique has been used widely on a number of problems including free and forced vibrations of strings and rods. The derivations of the solutions for strings and rods were presented by Graff [31] and that for the plate is presented below. This approach has previously not been applied to the problem of AE signals because of the much higher frequency content of these transient signals. The higher the frequency, the more terms that must be summed to obtain a good approximation. However, with the speed of modern computers, this approach is now feasible for AE signals.

In deriving the normal mode solution for the flexural wave, it was assumed that the flexural motion was governed by the classical equation of motion given in Eq. 3.15. All of the assumptions used to derive this equation are again implied; the plate is homogeneous, isotropic, thin, and under the condition of plane stress. The deformations are also assumed to be small and the coordinate axes and displacements are the same as those used in the earlier section on classical plate theory.

Before the solution for the case of forced motion can be solved, the normal modes for free vibration of the plate must be determined. Thus, solutions to the homogeneous equation of motion,

$$D\nabla^4 w\,(x,y,t) + \rho h \frac{\partial^2 w\,(x,y,t)}{\partial t^2} = 0 \qquad\qquad \text{Eq. 3.20}$$

are sought, in which, the forcing term q(x,y,t) has been set equal to zero. In order to solve this equation for the displacement, w, a separation of variables approach was used. The vertical displacement was assumed to have a form with harmonic time dependence given by

$$w\,(x,\,y,t) = X\,(x)\,Y\,(y)\,e^{-i\omega t} \qquad\qquad \text{Eq. 3.21}$$

where X(x) and Y(y) are functions (complex, in general) depending only on x and y respectively. Substituting Eq. 3.21 into Eq. 3.20 and reducing terms yields

$$X^{IV}Y + 2X^{II}Y^{II} + XY^{IV} - \beta^4 XY = 0 \qquad\qquad \text{Eq. 3.22}$$

where the Roman superscripts indicate differentiation and β is de-
fined as

$$\beta^4 = \frac{\omega^2 \rho h}{D} \quad .$$

<div align="right">Eq. 3.23</div>

In order for separation of variables to occur, it must be true that
either

$$Y^{II} = -\gamma^2 Y \quad \text{and} \quad Y^{IV} = \gamma^4 Y$$

<div align="right">Eq. 3.24</div>

or

$$X^{II} = -\alpha^2 X \quad \text{and} \quad X^{IV} = \alpha^4 X \quad .$$

<div align="right">Eq. 3.25</div>

Assuming the latter, then X must have a form of combinations of sines
and cosines.

The exact form is dependent on the boundary conditions chosen.
It is shown by Graff [31] that for this choice only the condition
of simply supported boundaries can be satisfied. That is, at least
one pair of opposite sides of the plate must have simply supported
boundary conditions. Other boundary conditions including clamped
and free boundaries are possible for the other plate edges.
However, the least difficult case to consider is that in which all
four edges are simply supported.

Assuming the origin of the coordinate axes is at one corner of the
plate and the length of the plate along x is a and that along y is b,
then the plate edges are at x=0, x=a, y=0, and y=b. Simply

supported boundary conditions at x=0 and x=a imply that the displacement, w, and the bending moment per unit length, M_x, are equal to zero at the plate edges. In terms of the displacement, these boundary conditions are

$$w = \frac{\partial^2 w}{\partial x^2} + \nu\frac{\partial^2 w}{\partial y^2} = 0 \qquad \text{Eq. 3.26}$$

at x=0 and x=a. The expressions for the bending moments and their relations to the displacements are discussed in more detail in the derivation of the classical flexural equation of motion for anisotropic materials in the next chapter. Substitution yields that Eq. 3.26 can only be satisfied if

$$X_n = \sin(\alpha_n x) \qquad \text{Eq. 3.27}$$

where

$$\alpha_n = \frac{n\pi}{a} \quad \text{for n = (1, 2, 3, ...).} \qquad \text{Eq. 3.28}$$

Likewise, applying the simply supported boundary conditions at y=0 and y=b yields that

$$Y_m = \sin(\gamma_m y) \qquad \text{Eq. 3.29}$$

where

$$\gamma_m = \frac{m\pi}{b} \quad \text{for m = (1, 2, 3, ...).} \qquad \text{Eq. 3.30}$$

Thus, the spatial dependence of the solution for the problem of free vibration of a rectangular plate is given by an infinite number of modes described by

$$W_{nm} = X_n Y_m = \sin(\alpha_n x) \sin(\gamma_m y) \ .$$
Eq. 3.31

The frequency of each mode, ω_{nm} , is determined by substituting the modes back into Eq. 3.22 which yields

$$(\alpha_n^4 + 2\alpha_n^2 \gamma_m^2 + \gamma_m^4 - \beta_{nm}^4) X_n Y_m = 0$$
Eq. 3.32

where

$$\beta_{nm}^4 = \frac{\omega_{nm}^2 \rho h}{D} \ .$$
Eq. 3.33

Solving for ω_{nm} yields

$$\omega_{nm} = \pi^2 \left(\frac{n^2}{a^2} + \frac{m^2}{b^2} \right) \sqrt{\frac{D}{\rho h}} \ .$$
Eq. 3.34

The solution for free vibrations in a rectangular isotropic plate is then expressed as a double series of an infinite number of modes as

$$w(x,y,t) = \sum_{n=1}^{\infty} \sum_{m=1}^{\infty} X_n(x) Y_m(y) e^{-i\omega_{nm}t}$$
Eq. 3.35

or

$$w(x,y,t) = \sum_{n=1}^{\infty} \sum_{m=1}^{\infty} W_{nm}(x,y) e^{-i\omega_{nm}t} \qquad . \qquad \text{Eq. 3.36}$$

The solution to the inhomogeneous equation of motion in which the forcing function q(x,y,t) is not equal to zero, can be expressed as

$$w(x,y,t) = \sum_{n=1}^{\infty} \sum_{m=1}^{\infty} W_{nm}(x,y) q_{nm}(t) \qquad \text{Eq. 3.37}$$

where the $q_{nm}(t)$ are determined from the forcing function. Substituting this solution into the equation of motion, Eq. 3.15, yields

$$\sum_{n=1}^{\infty} \sum_{m=1}^{\infty} \left(\frac{\partial^2 q_{nm}(t)}{\partial t^2} + \frac{D}{\rho h} \beta_{nm}^4 q_{nm}(t) \right) W_{nm}(x,y) = \frac{q(x,y,t)}{\rho h} \qquad \text{Eq. 3.38}$$

Next, both sides of this equation are multiplied by $W_{ij}(x,y)$ and integrated from x=0 to a and y=0 to b. This allows the property of orthogonality of the normal modes to be applied which means that

$$\int_{x=0}^{a} \int_{y=0}^{b} W_{nm}(x,y) W_{ij}(x,y) \, dx \, dy = 0 \qquad \text{Eq. 3.39}$$

except when n=i and m=j. For the case of simply supported edges, when n=i and m=j this expression is equal to $\frac{ab}{4}$. Eq. 3.38 is then reduced to

$$\frac{\partial^2 q_{nm}(t)}{\partial t^2} + \frac{D}{\rho h}\beta_{nm}^4 q_{nm}(t)$$

$$= \frac{4}{\rho hab}\int_{x=0}^{a}\int_{y=0}^{b} W_{nm}(x,y)\, q(x,y,t)\, dxdy \qquad . \qquad \text{Eq. 3.40}$$

The solution to this equation for zero initial conditions is given by

$$q_{nm}(t) = \frac{1}{\rho h\omega_{nm}}\int_{0}^{t} Q_{nm}(\tau)\sin\omega_{nm}(t-\tau)\, d\tau \qquad \text{Eq. 3.41}$$

where

$$Q_{nm}(t) = \frac{4}{ab}\int_{x=0}^{a}\int_{y=0}^{b} W_{nm}(x,y)\, q(x,y,t)\, dxdy \qquad . \qquad \text{Eq. 3.42}$$

The shape of the input forcing function must now be considered. An impulse loading at x=ξ and y=ζ is chosen. The form of this input is

$$q(x,y,t) = P\delta(x-\xi)\delta(y-\zeta)\delta(t) \qquad \text{Eq. 3.43}$$

where P is the amplitude of the impulse. Substituting this and carrying out the integrations yields the solution for the displacement as

$$w(x,y,t) = \frac{4P}{\rho hab}\sum_{n=1}^{\infty}\sum_{m=1}^{\infty}\frac{\sin\alpha_n x \sin\gamma_m y \sin\alpha_n \xi \sin\gamma_m \zeta \sin\omega_{nm}t}{\omega_{nm}}$$

$$\text{Eq. 3.44}$$

The solution for the case of the desired step function input can be

obtained by integrating this solution with respect to time. The result is

$$w(x,y,t) \quad =$$

$$\frac{4P}{\rho hab} \sum_{n=1}^{\infty} \sum_{m=1}^{\infty} \frac{\sin\alpha_n x \sin\gamma_m y \sin\alpha_n \xi \sin\gamma_m \zeta \, (1 - \cos\omega_{nm}t)}{\omega_{nm}^2} \quad . \text{ Eq. 3.45}$$

Because this solution is of the form of an infinite double sum, it is impossible to evaluate the result exactly. However, if enough terms are evaluated as to include all of those which have a frequency within the frequency range of interest, the resulting approximate solution will be valid.

Two programs were written to evaluate this expression numerically. The first version evaluated the solution as expressed above. The second version imposed filtering which approximated the receiving transducers response on the solution so that the theoretical and experimental data could be compared. It was easier to apply the filtering response on the theoretical data than it was to deconvolve the transducer response from the experimental data. The filtering procedure and the filter coefficients are discussed later.

Both programs were written in the Pascal computer language and compiled and executed on a personal computer (Macintosh IIfx). The input parameters for the program included the length, width, and thickness of the plate, as well as its density, Poisson's ratio, and Young's modulus. Also, the position of the source and receiver were needed along with the number of modes to be summed, the number of points in time and the time spacing between points.

The values used for the input parameters were chosen to match ex-

perimental measurements made on a 0.003175 m. thick aluminum 2024 plate. The width of this plate was 0.508 m. and its length was 0.381 m. The value for the Poisson's ratio was 0.3, the density was 2770 kg/m^3, and the Young's modulus was 73.0 GPa. The source position was the same for all of the calculations at the center width (0.254 m.) and at a length of 0.127 m. from one edge. The calculations were repeated with the receiver positions always along the center width (0.254 m.) but at a distance of from 0.0762 m. to 0.1778 m. from the source at intervals of 0.0254 m. The positioning of the sensors relative to the plate is shown in Figure 3.10.
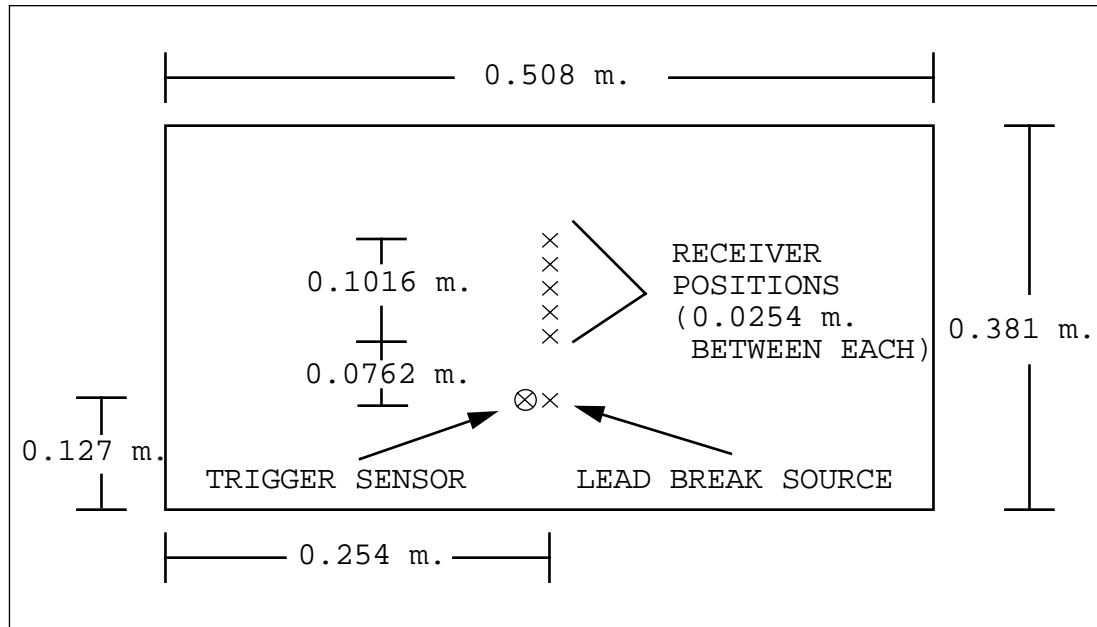
Figure 3.10   Positioning of sensors used for experimental measurements and theoretical calculations for AE signals in thin aluminum plate.

The number of modes summed was from n=1 to 100 and m=1 to 100 for a total of 10,000 modes. Calculating ω_{nm} for n=100 and m=100 using Eq. 3.34 and then using the relation

$$f_{nm} = \frac{\omega_{nm}}{2\pi} \qquad \text{Eq. 3.46}$$

reveals that the maximum frequency content of the calculated signal is 834 kHz. The maximum frequency for which all of the possible modes of frequency equal to or less have been included in the summation is given by the minimum of $f_{1,100}$ and $f_{100,1}$. This frequency is 300 kHz for $f_{1,100}$ which is above the maximum frequency content of about 200 kHz observed in the experimental flexural signal.

The number of points evaluated was either 512 or 1024 with a spacing of 0.2 μsec. between points. This was consistent with the 5 MHz sampling frequency used in the experimental measurements. The time to complete a theoretical calculation for a 1024 point waveform was 480 seconds for the model without filtering and 633 seconds with filtering.

The results of the theoretical calculation without filtering were compared to those from a calculation for an infinite plate. The solution for the infinite plate was obtained by integral transform techniques and was presented by Medick [34]. It is given by

$$w(r,t) = \frac{P}{4\pi (\rho h D)^{1/2}} tH\left(\frac{\frac{1}{4}\left(\sqrt{\frac{\rho h}{D}}\right)r^2}{t}\right) \qquad \text{Eq. 3.47}$$

where

$$H(x) = \frac{\pi}{2} - Si(x) + xCi(x) - \sin(x) \qquad \text{Eq. 3.48}$$

with Si(x) and Ci(x) being the sine and cosine integrals, respective-
ly. In this equation, r is the distance from the source to the re-
ceiver. This solution was evaluated on a personal computer (Macintosh
IIfx) with Mathematica (Wolfram Research Inc.).

The normal mode solution and that for the infinite plate should be
the same up until the point of the arrival of the reflections in
the normal mode predictions. Thus, the calculations for the compari-
son were carried out for a large enough plate and short enough time
period that reflections were avoided. For these calculations, the
plate dimensions and transducer positions were the same as those dis-
cussed earlier with the source to receiver distance being 0.127 m.
A plot of the normal mode solution and that obtained for the infinite
plate are shown in Figure 3.11. Excellent agreement between the two
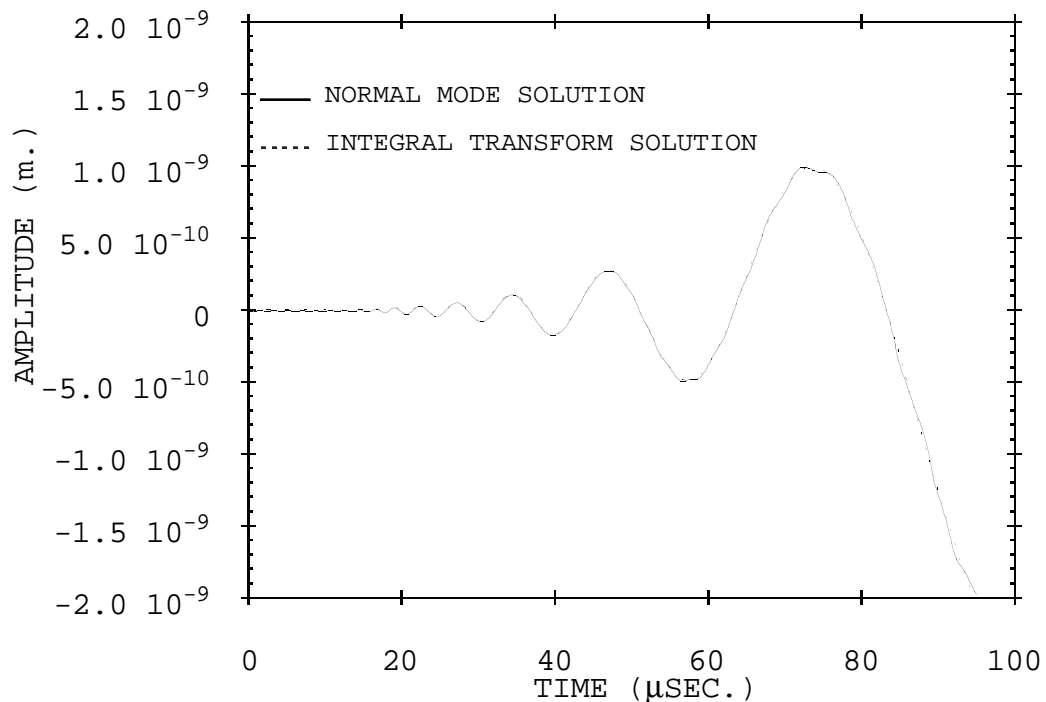
Figure 3.11   Predicted flexural response for source to receiv-
er distance of 0.127 m. evaluated by normal mode
and integral transform techniques.

solutions is demonstrated.

In order to compare the theoretical solution obtained by the normal mode approach to the experimental waveforms, it was first necessary to correct for the filtering on the signal induced by the transducer response. As mentioned previously, it was easier to implement the filtering on the theoretical signal than to deconvolve the transducer response from the experimental signal. The process of filtering the theoretical signal was accomplished by multiplying the amplitude contribution of each mode by a filter coefficient which was dependent on the frequency, ω_{nm}, of that mode. The filter coefficients were determined by fitting the frequency response of the ultrasonic transducer used in the measurements as determined from the face-to-face swept sine evaluation to a second order polynomial (quadratic) fit. This fit worked well for higher frequencies but did not agree below 30 kHz where the transducer response declined more rapidly than the fit. Thus, an additional linear roll off filter was implemented in this frequency regime. The value of the filter coefficient was equal to 1.0 if ω_{nm} was greater than 4.928 X 10^6 rad./ sec. (f_{nm} > 784 kHz). Between 1.885 X 10^5 rad./sec. (30 kHz) and 4.928 X 10^6 rad./sec., the filter coefficient (fc) was given by

$$\text{fc} = 0.052 + 3.82{\times}10^{-7}\omega_{nm} - 3.876{\times}10^{-14}\omega_{nm}^2 \qquad \text{Eq. 3.49}$$

and below 1.885 X 10^5 rad./sec. (30 kHz), fc was given by

$$\text{fc} = (0.052 + 3.82{\times}10^{-7}\omega_{nm} - 3.876{\times}10^{-14}\omega_{nm}^2)$$

$$* (-0.275 + 6.812{\times}10^{-6}\omega_{nm}) \quad . \qquad \text{Eq. 3.50}$$

A plot of the filter coefficient values versus frequency is shown

in Figure 3.12. Because of the y-intercept values determined in the
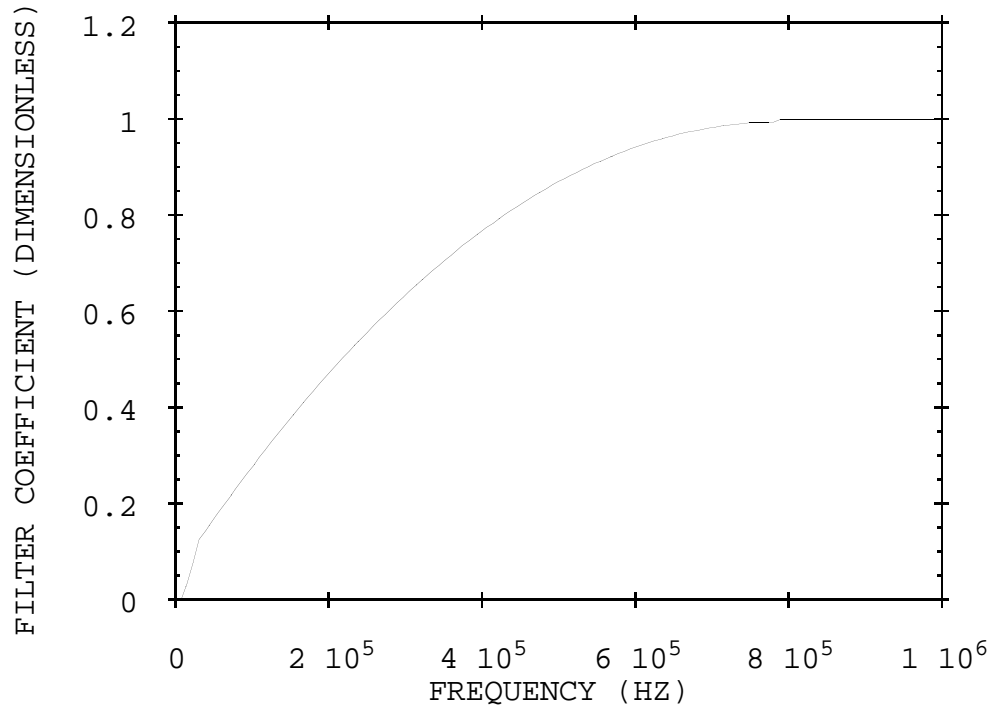
Figure 3.12   Filter coefficient used in normal mode solution
to account for transducer response.

fit of the transducer response, the filter coefficient is predicted

to be negative for frequencies less than approximately 6 kHz. Thus,

in the program, the filter coefficient was set equal to zero for

the 0 to 6 kHz frequency range.

It is noted that this filtering procedure provides a way of rela-

tively, not absolutely, comparing the theoretical and experimental

wave shapes. This is because the filtering coefficients were not

based on an absolute calibration of the transducer output in terms of

volts per meter. They only provided a relative value of the signal at

each particular frequency as compared to the value at frequencies

above 784 kHz where the filter coefficient was arbitrarily assigned

the value 1.0. Thus, the amplitudes of the theoretical waveforms

are in meters while those of the experimental waveforms are in volts. These could easily be made absolute, if needed, with the use of an "absolute" transducer such as a capacitive or optical sensor.

The experimental waveforms were acquired from a plate of aluminum 2024 of thickness 0.003175 m. As discussed previously, the dimensions were 0.508 m. in width and 0.381 m. in length. The source was a pencil lead break (Hsu-Neilsen source) which has a time dependence which can be approximated by a step function. The position of the source was at the center width of the plate and at a length of 0.127 m. from one edge. An R15 AE transducer was positioned next to the source point. It provided a trigger signal for the transient recorder which was used to digitize the waveform detected by the 3.5 MHz ultrasonic sensor. The sampling frequency of the transient recorder was 5 MHz and the captured waveforms were stored on the personal computer for later display and analysis.

The receiver positions were the same as those used in the model calculations. These were at the center width of the plate at distances of 0.0762 m. to 0.1778 m. from the source in 0.0254 m. intervals as shown in Figure 3.10. The detected signals from the ultrasonic sensors were amplified by a preamplifier in which no filter was used. A block diagram of the experimental apparatus is presented in Figure 3.13.

In order to compare the theoretical and experimental waveforms, it was necessary to correct for timing delays in the triggering of the transient recorder. This was analyzed by measuring the arrival time of the extensional wave at each distance of propagation. The distance was then plotted versus the arrival time and fit to a line using a least squares fit. The y-intercept yields the time of any delay in
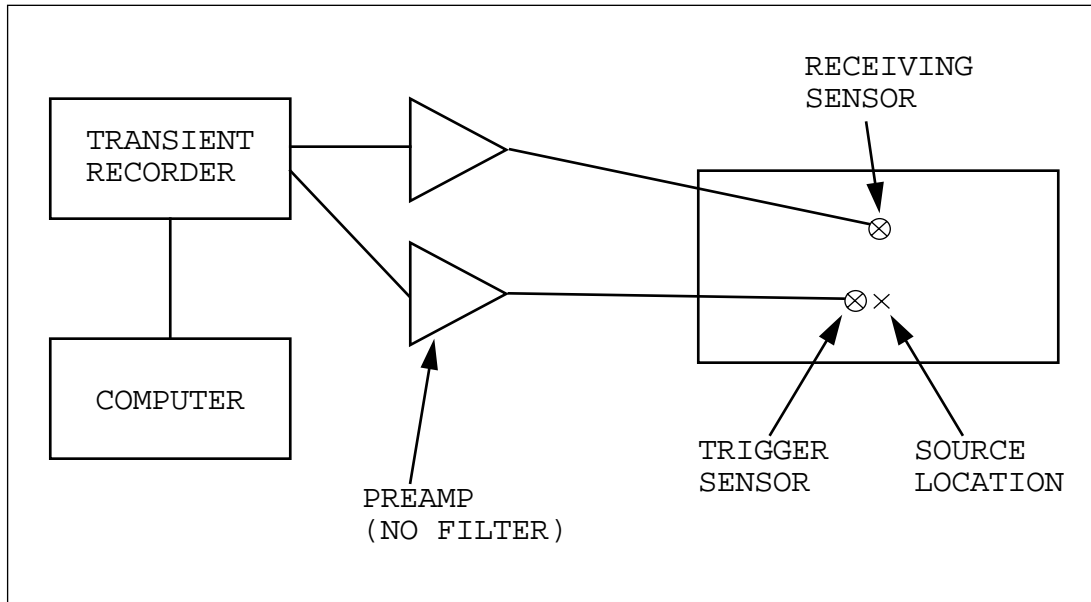
Figure 3.13   Apparatus used to measure AE signals generated
by pencil lead breaks in thin aluminum plate.

triggering, while the inverse of the slope is the extensional plate

wave velocity. Figure 3.14 shows this plot and the linear fit. The

trigger delay was determined to be 6.64 μsec. while the extensional

velocity was predicted to be 5427 m/sec. Based on this analysis, each

experimental waveform was shifted back 6.6 μsec. to account for this

trigger delay.

The experimental and theoretical waveforms for the first 100

μsec. are compared in the plots of Figure 3.15 to Figure 3.19. On

the time axes of these plots, the time beyond which theory and exper-

iment should agree based on the criterion expressed by Medick [34] is

indicated by τ_c. This is the time at which the wavelength is equal

to sixteen times the plate thickness. It can be seen that there is

good agreement between theory and experiment beyond this initial

critical time. Before τ_c, the higher frequencies in the predicted

normal mode solution arrive much earlier than those in the experimen-
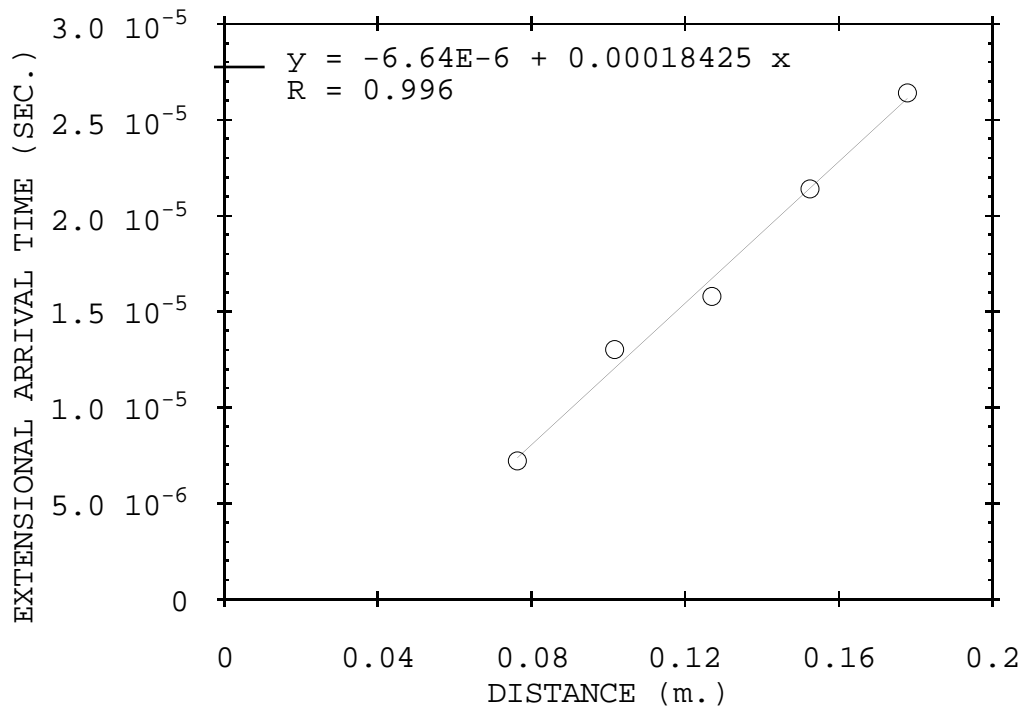
Figure 3.14 Distance of propagation versus extensional wave
arrival time and linear fit used to determine
trigger time delay.
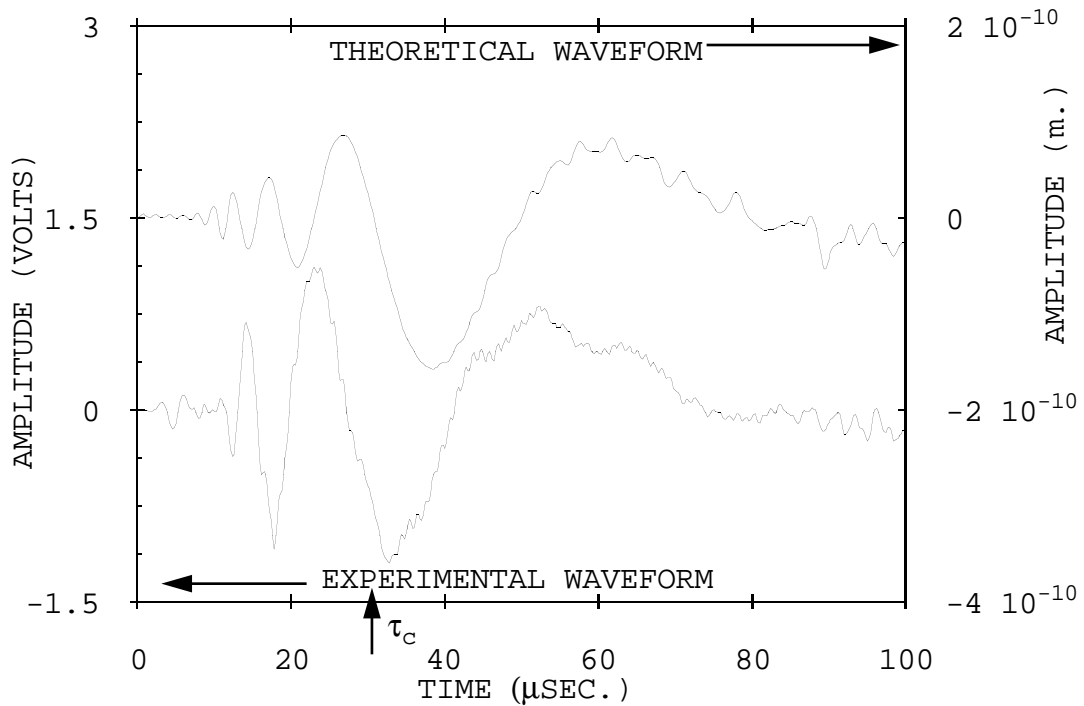
Figure 3.15 Theoretical normal mode and experimental wave-
forms for distance of propagation of 0.0762 m.
in thin plate aluminum.
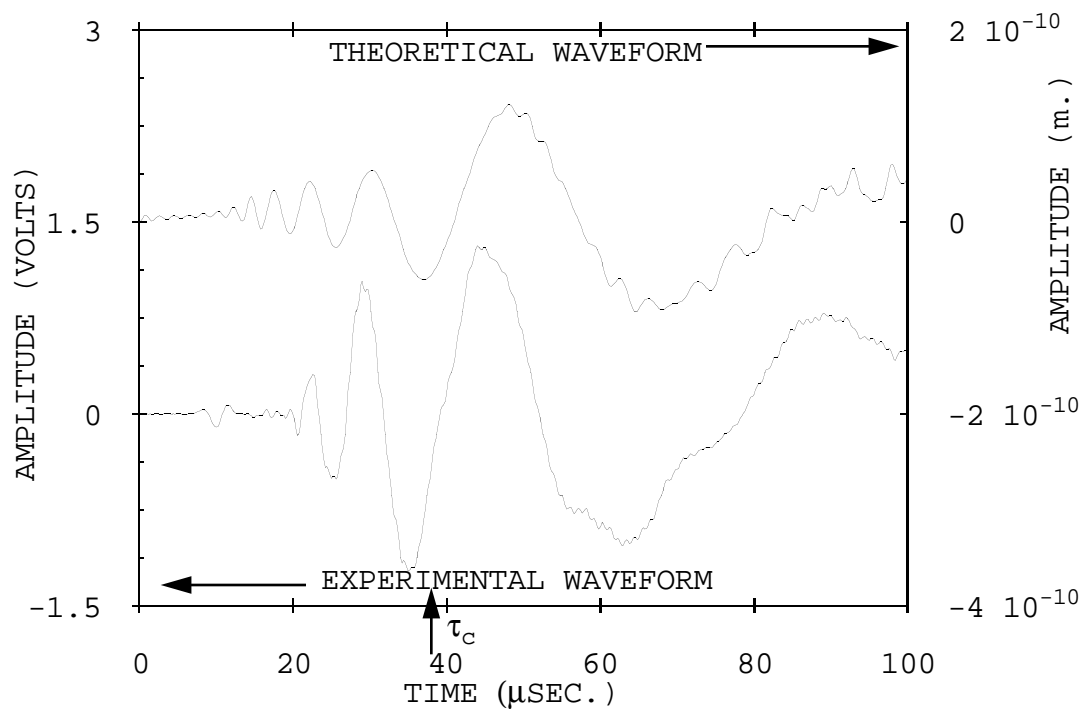
Figure 3.16   Theoretical normal mode and experimental wave-
forms for distance of propagation of 0.1016 m.
in thin plate aluminum.
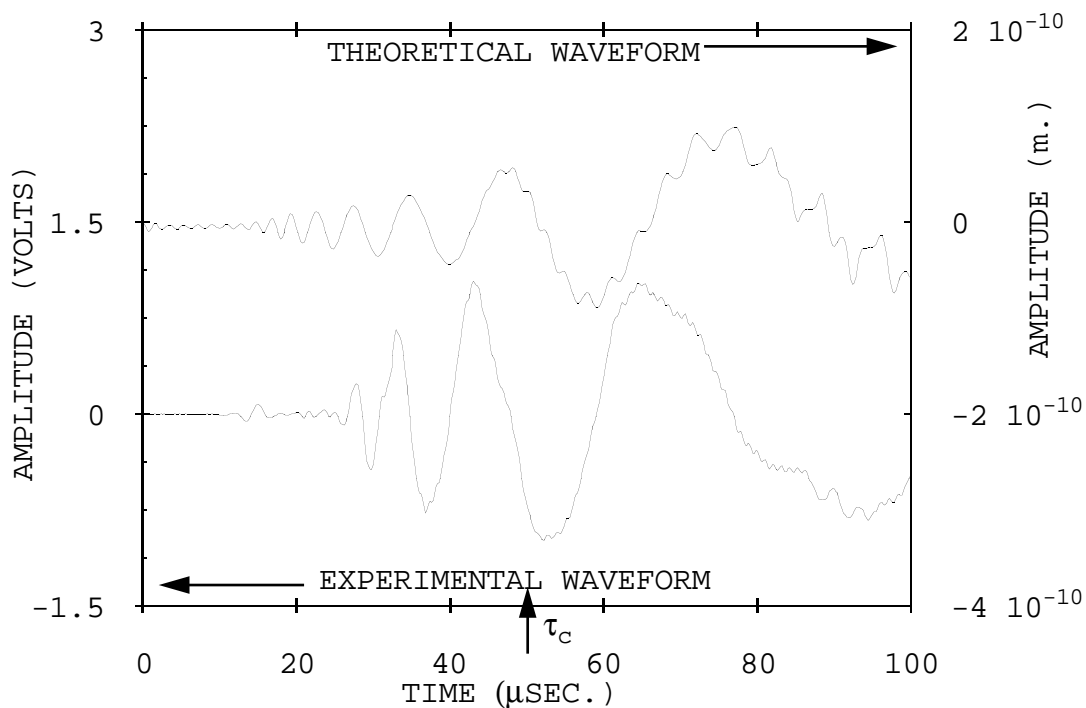
Figure 3.17   Theoretical normal mode and experimental wave-
forms for distance of propagation of 0.127 m. in
thin plate aluminum.
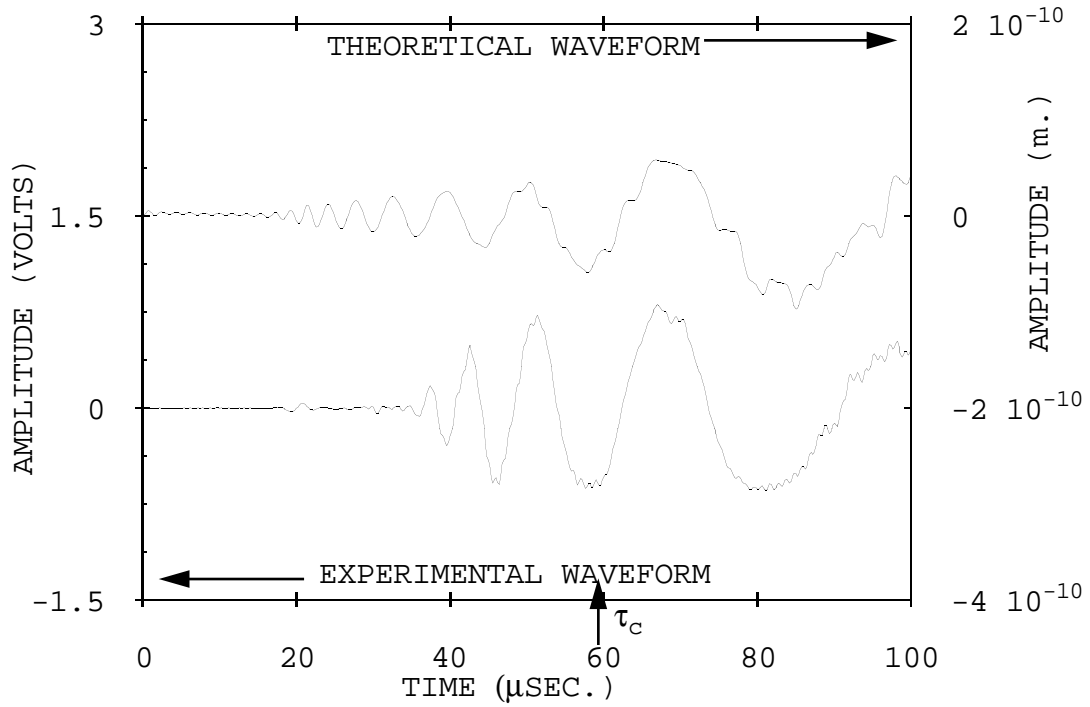
Figure 3.18   Theoretical normal mode and experimental wave-
              forms for distance of propagation of 0.1524 m.
              in thin plate aluminum.
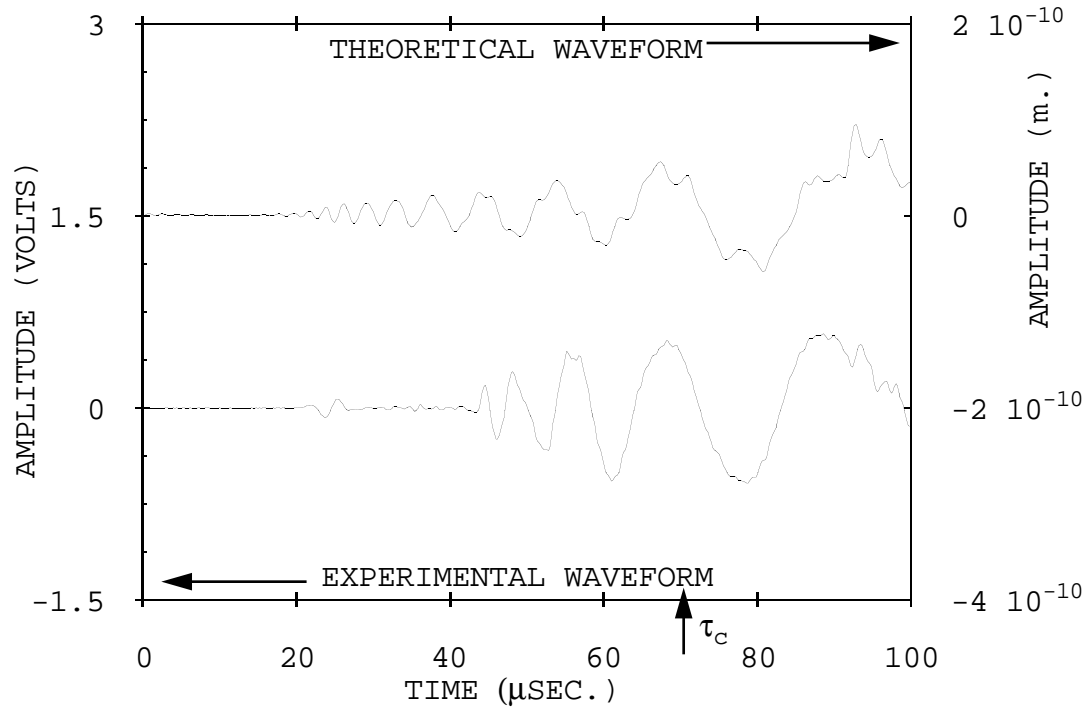
Figure 3.19   Theoretical normal mode and experimental wave-
              forms for distance of propagation of 0.1778 m.
              in thin plate aluminum.

tal waveform. This is as expected, since the classical flexural

wave dispersion relation predicts velocities that increase without

limit as the frequency increases. This caused the predicted veloci-

ties to be higher than the actual velocity at higher frequencies.

The experimental and theoretical waveforms for the propagation

distance of 0.1778 m. are replotted in Figure 3.20 for a longer peri-
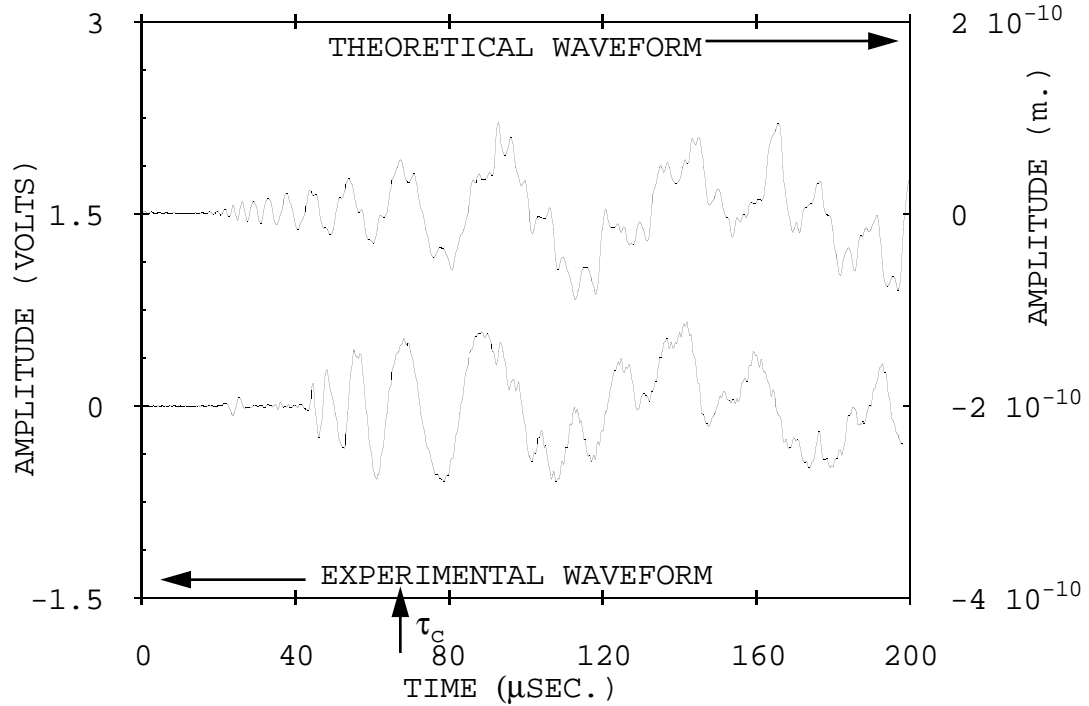
Figure 3.20   Theoretical normal mode and experimental wave-
              forms for distance of propagation of 0.1778 m.
              in thin plate aluminum for long times.

od of time. In this plot, the effects of finite dimensions of the

plate are observed as reflections in both the theoretical and experi-

mental waveforms. Again, because of the limitations of the applica-

bility of classical plate theory in the high frequency portion of the

reflections, absolute agreement is not obtained. However, qualita-

tively the reflection portion of the signals are similar.

In summary, the normal mode expansion technique has been shown

to be a feasible method for predicting flexural vibrations in

finite aluminum plates. Because of the high speed of modern personal computers, the solution obtained by the summation of 10,000 modes was accomplished in only a few minutes. With this number of modes, the frequency content of the theoretical signal was sufficient to allow comparisons with experimental AE signals created by pencil lead breaks. Good agreement was shown between theory and experiment over the range of frequencies for which classical plate theory remains a valid approximation. It is noted here that the normal mode expansion technique may be applicable to higher order plate theories which would allow better agreement with experiment at higher frequencies. Furthermore, the solution obtained by normal mode expansion was shown to be in agreement with that predicted by an integral transform technique for an infinite plate up until the time that reflections begin to occur in the normal mode solution.

IV. Plate Wave Propagation in Composites

IV.1 Introduction

The final area of investigation in this research was a study of AE propagation in anisotropic composite materials. Composite materials, because of their high strength and stiffness along with their low density, are becoming an increasingly important material in the aerospace industry. However, because of the inhomogeneous and anisotropic nature of these materials, their nondestructive evaluation (NDE) by conventional techniques such as ultrasonics, AE, and thermal analysis is much more difficult. In particular, AE signals in composites are more difficult to interpret than in isotropic metals not only because of the previously mentioned factors, but also because of the multiple AE sources that are active in composites. These may include fiber breakage, matrix cracking, fiber matrix debonding, and delamination. In order to begin to better interpret AE signals in composites to determine the locations and nature of the sources, it is first necessary to better understand the propagation of these signals in these materials.

Thus, this provided the motivation for this portion of the research. It was again shown that AE signals in composite plates propagated with plate wave characteristics. The applicability of classical plate theory was investigated for waves in these materials. In particular, classical anisotropic plate theory was evaluated for predicting the velocities of the extensional and flexural modes and the waveshape of the flexural mode.

Measurements of the extensional velocities at angles of propagation of 0, 45, and 90 degrees with respect to the plate coordinate

axes were made in graphite/epoxy (gr/ep) composite plates with several different fiber layups. These were compared with theoretical predictions based on classical plate theory for an anisotropic material. Similar measurements were also made for the flexural mode except that the velocities were determined at a number of frequencies to evaluate the dispersion behavior of this mode. Again, these were compared with theoretical predictions both for classical plate theory as well as a higher order plate theory. Then, the normal mode expansion technique used previously to predict the flexural wave shape in aluminum was extended to allow predictions in these composite materials. Comparisons between theoretical and experimental waveforms were then made.

Additionally, to demonstrate that the propagation of AE signals as plate modes is not limited to simple flat plates, an investigation of AE signals in a practical structure of interest was made. This structure was a thin walled gr/ep composite tube of a design proposed to be used on the strut structure holding together NASA's proposed Space Station Freedom (SSF). The velocities of the extensional and flexural modes were measured and compared with theoretical predictions.

IV.2 Theory

Before proceeding with the measurements in composites, the theoretical tools used to understand and predict the behavior of plate waves must be extended to account for the anisotropy of these materials. To accomplish this, the equations needed to predict the in-plane and bending elastic properties of a laminated orthotropic plate are first presented. These are based on well known laminated plate theory. Following this, classical plate theory is extended to include the

anisotropic elastic properties predicted by laminated plate theory. Using these equations of motion, the dispersion relations for the extensional and flexural modes of orthotropic composites are predicted. Then, the extension of the normal mode expansion technique to the case of special orthotropic symmetry is carried out.

It is pointed out in advance that experimental measurements of the flexural dispersion, to be presented later, were not in good agreement with classical plate theory predictions. This turned out to be due to the effects of shear and rotatory inertia which are neglected in classical plate theory. Subsequent calculations of the displacements also showed poor agreement with experimentally measured waveforms. Consequently, dispersion relations based on a higher order plate theory, which accounts for these effects, were derived and shown to be in agreement with the measured velocities. The results point the way to improved computations of displacement, however, this was not carried out in this work.

Laminated plate theory for composite materials has been treated by a number of authors. Two good references presenting a detailed treatment of this subject and which are the basis of the material presented here are Whitney [46] and Tsai and Hahn [47]. The assumptions on which laminated plate and classical plate theory are based were explicitly stated by Whitney [46]. They are reproduced here for clarity. The assumptions are:

"1. The plate is constructed of an arbitrary number or layers of orthotropic sheets bonded together. However, the orthotropic axes of material symmetry of an individual layer need not coincide with the x-y axes of the plate.

2. The plate is thin, i.e., the thickness h is much smaller than the other physical dimensions.

3. The displacements u, v, and w are small compared to the plate
   thickness.

4. In-plane strains ε_x, ε_y, and ε_{xy} are small compared to unity.

5. In order to include in-plane force effects, nonlinear terms
   in the equations of motion involving products of stresses and
   plate slopes are retained. All other nonlinear terms are ne-
   glected.

6. Transverse shear strains ε_{xz} and ε_{yz} are negligible.

7. Tangential displacements u and v are linear functions of the
   z coordinate.

8. The transverse normal strain ε_z is negligible.

9. Each ply obeys Hooke's law.

10. The plate has constant thickness.

11. Rotatory inertial terms are negligible.

12. There are no body forces.

13. Transverse shear stresses σ_{xz} and σ_{yz} vanish on the surfaces
    z=+/-h/2."

The first step in laminated plate theory is to show the stress-
strain relations for a single unidirectional orthotropic lamina.
For this, the x axis is designated to be along the fiber direction
and the y axis is perpendicular to the fiber direction in the plane
of the lamina. The relation between stress and strain for a lamina is
given by

$$
\begin{bmatrix} \sigma_{xx} \\ \sigma_{yy} \\ \sigma_{xy} \end{bmatrix} = \begin{bmatrix} Q_{xx} & Q_{xy} & 0 \\ Q_{yx} & Q_{yy} & 0 \\ 0 & 0 & Q_{ss} \end{bmatrix} \begin{bmatrix} \varepsilon_{xx} \\ \varepsilon_{yy} \\ \gamma_{xy} \end{bmatrix}
\qquad \text{Eq. 4.1}
$$

where the Q_{ij}'s are the elastic stiffness coefficients and the engi-

neering shear strain, γ_{xy}, is used. The engineering shear strain is twice the tensorial shear strain which was defined in Eq. 2.7. Since $Q_{xy}=Q_{yx}$, only four stiffness coefficients are needed to describe the elastic properties of an orthotropic lamina. These are related to the engineering properties of the lamina by

$$Q_{xx} = \frac{E_x}{1 - \nu_x \nu_y} \qquad \text{Eq. 4.2}$$

$$Q_{yy} = \frac{E_y}{1 - \nu_x \nu_y} \qquad \text{Eq. 4.3}$$

$$Q_{xy} = \frac{\nu_x E_y}{1 - \nu_x \nu_y} = \frac{\nu_y E_x}{1 - \nu_x \nu_y} \qquad \text{Eq. 4.4}$$

and

$$Q_{ss} = E_s \qquad \text{Eq. 4.5}$$

where E_x is the longitudinal Young's modulus, E_y is the transverse Young's modulus, E_s is the longitudinal shear modulus, and ν_x and ν_y are the longitudinal and transverse Poisson's ratios respectively.

The stiffness coefficients presented above are those relative to the designated axes where the x axis was along the fiber and the y axis was perpendicular to the fibers. The stiffness coefficients for a lamina relative to different axes, 1 and 2, in which 1 and 2 are still in the plane of the lamina, but have been rotated by an angle, θ, are also important. The angle θ is defined to be positive

when the 1-2 axes are rotated counterclockwise from the x-y axes. These are needed in the calculation of laminate stiffness properties in which all laminae are not aligned with their fiber direction along the same axes. The so-called off-axis stiffness coefficients are calculated by applying transformation relations which are given by

$$Q_{11} = m^4 Q_{xx} + n^4 Q_{yy} + 2m^2 n^2 Q_{xy} + 4m^2 n^2 Q_{ss} \qquad \text{Eq. 4.6}$$

$$Q_{22} = n^4 Q_{xx} + m^4 Q_{yy} + 2m^2 n^2 Q_{xy} + 4m^2 n^2 Q_{ss} \qquad \text{Eq. 4.7}$$

$$Q_{12} = m^2 n^2 Q_{xx} + m^2 n^2 Q_{yy} + (m^4 + n^4) Q_{xy} - 4m^2 n^2 Q_{ss} \qquad \text{Eq. 4.8}$$

$$Q_{66} = m^2 n^2 Q_{xx} + m^2 n^2 Q_{yy} - 2m^2 n^2 Q_{xy} + (m^2 - n^2)^2 Q_{ss} \qquad \text{Eq. 4.9}$$

$$Q_{16} = -m^3 n Q_{xx} + mn^3 Q_{yy} + (m^3 n - mn^3) Q_{xy} + 2 (m^3 n - mn^3) Q_{ss} \qquad \text{Eq. 4.10}$$

and

$$Q_{26} = -mn^3 Q_{xx} + m^3 n Q_{yy} + (mn^3 - m^3 n) Q_{xy} + 2 (mn^3 - m^3 n) Q_{ss} \qquad \text{Eq. 4.11}$$

where $m = \cos(\theta)$ and $n = \sin(\theta)$. Because of the symmetry of the stress and strain tensors, these coefficients are also symmetric with $Q_{ij} = Q_{ji}$. However, it is noted that now six coefficients are needed, in general, to describe the off-axis elastic behavior of the lamina.

Next, the in-plane and bending stiffnesses of a laminate are considered. The fiber direction of each orthotropic laminae is defined to be at an angle, θ, with respect to the x axis of the laminate.

The y axis of the laminate is orthogonal to the x axis and is also in the plane of the plate. The z axis is orthogonal to x and y and thus is perpendicular to the plate with its origin at the midplane of the plate. The stress and moment resultants for such a laminate are defined as

$$(N_x, N_y, N_{xy}) = \int_{-\frac{h}{2}}^{\frac{h}{2}} (\sigma_x^{(k)}, \sigma_y^{(k)}, \sigma_{xy}^{(k)}) \, dz \qquad \text{Eq. 4.12}$$

and

$$(M_x, M_y, M_{xy}) = \int_{-\frac{h}{2}}^{\frac{h}{2}} (\sigma_x^{(k)}, \sigma_y^{(k)}, \sigma_{xy}^{(k)}) \, z dz \qquad \text{Eq. 4.13}$$

where the superscript k indicates the k'th layer of the laminate and h is the thickness of the laminate.

The constituitive relations relate the stress and moment result-ants to the midplane strains, $(\varepsilon_x^0, \varepsilon_y^0, \gamma_{xy}^0)$, and the curvatures, $(\kappa_x, \kappa_y, \kappa_{xy})$ which are defined by

$$\kappa_x = -\frac{\partial^2 w}{\partial x^2} \qquad \text{Eq. 4.14}$$

$$\kappa_y = -\frac{\partial^2 w}{\partial y^2} \qquad\qquad \text{Eq. 4.15}$$

and

$$\kappa_{xy} = -2\frac{\partial^2 w}{\partial x \partial y} \quad . \qquad\qquad \text{Eq. 4.16}$$

They are given by

$$
\begin{bmatrix} N_x \\ N_y \\ N_{xy} \\ M_x \\ M_y \\ M_{xy} \end{bmatrix}
=
\begin{bmatrix}
A_{11} & A_{12} & A_{16} & B_{11} & B_{12} & B_{16} \\
A_{12} & A_{22} & A_{26} & B_{12} & B_{22} & B_{26} \\
A_{16} & A_{26} & A_{66} & B_{16} & B_{26} & B_{66} \\
B_{11} & B_{12} & B_{16} & D_{11} & D_{12} & D_{16} \\
B_{12} & B_{22} & B_{26} & D_{12} & D_{22} & D_{26} \\
B_{16} & B_{26} & B_{66} & D_{16} & D_{26} & D_{66}
\end{bmatrix}
\begin{bmatrix} \varepsilon_x^0 \\ \varepsilon_y^0 \\ \gamma_{xy}^0 \\ \kappa_x \\ \kappa_y \\ \kappa_{xy} \end{bmatrix}
\qquad \text{Eq. 4.17}
$$

where the A_{ij}'s are the in-plane stiffnesses, the D_{ij}'s are the bend-
ing stiffnesses, and the B_{ij}'s are the stiffnesses coupling in-plane
and bending effects. If the laminate is symmetric such that the upper
half of the laminate is the same as the lower half except the stack-
ing sequence is reversed in order to maintain the midplane
symmetry, then all of the B_{ij} are equal to zero.

The in-plane stiffness coefficients as a function of the
laminate stiffnesses are given by

$$A_{ij} = \int_{-\frac{h}{2}}^{\frac{h}{2}} Q_{ij}^{(k)} dz \qquad \text{Eq. 4.18}$$

while the bending coefficients are given by

$$D_{ij} = \int_{-\frac{h}{2}}^{\frac{h}{2}} Q_{ij}^{(k)} z^2 dz \qquad . \qquad \text{Eq. 4.19}$$

If the plate is symmetric, then $A_{16}=A_{26}=0$ and thus only four stiffness coefficients are needed. However, all six of the bending stiffness coefficients are nonzero for a general symmetric laminate. If the symmetric laminate contains only fiber orientations of 0 and 90 degrees (i.e. a cross ply laminate) then $D_{16}=D_{26}=0$. This is known as a "specially" orthotropic laminate.

The stiffness properties of the laminate transform to different axes in a similar fashion to those of an individual lamina. If the new axes are the x'-y' which are still in the plane of the plate but with the x' axis rotated by an angle θ from the x axis, then the in-plane stiffnesses for a symmetric laminate are given by

$$A'_{11} = m^4 A_{11} + n^4 A_{22} + 2m^2 n^2 A_{12} + 4m^2 n^2 A_{66} \qquad \text{Eq. 4.20}$$

$$A'_{22} = n^4 A_{11} + m^4 A_{22} + 2m^2 n^2 A_{12} + 4m^2 n^2 A_{66} \qquad \text{Eq. 4.21}$$

$$A'_{12} = m^2n^2A_{11} + m^2n^2A_{22} + (m^4 + n^4)\,A_{12} - 4m^2n^2A_{66} \qquad \text{Eq. 4.22}$$

$$A'_{66} = m^2n^2A_{11} + m^2n^2A_{22} - 2m^2n^2A_{12} + (m^2 - n^2)^2A_{66} \qquad \text{Eq. 4.23}$$

$$A'_{16} = -m^3nA_{11} + mn^3A_{22} + (m^3n - mn^3)\,A_{12} + 2\,(m^3n - mn^3)\,A_{66} \quad \text{Eq. 4.24}$$

and

$$A'_{26} = -m^3nA_{11} + mn^3A_{22} + (mn^3 - m^3n)\,A_{12} + 2\,(mn^3 - m^3n)\,A_{66} \quad \text{Eq. 4.25}$$

where again m=cos(θ) and n=sin(θ) and θ is positive if the rotation from the unprimed axes to the primed axes is in a counterclockwise direction. All six stiffness coefficients are now needed to describe the elastic behavior of the laminate.

   If the laminate is a symmetric cross-ply laminate, the bending stiffnesses transform in the exact same way as the in-plane stiffnesses. The appropriate equations can be obtained by replacing the A's with D's in Eq. 4.20 to Eq. 4.25. If the laminate is symmetric but has lamina with layup angles other than 0 or 90 degrees, the transformation relations are

$$D'_{11} = m^4D_{11} + n^4D_{22} + 2m^2n^2D_{12} + 4m^2n^2D_{66} + 4m^3nD_{16} + 4mn^3D_{26}$$

$$\text{Eq. 4.26}$$

$$D'_{22} = n^4D_{11} + m^4D_{22} + 2m^2n^2D_{12} + 4m^2n^2D_{66} - 4mn^3D_{16} - 4m^3nD_{26}$$

$$\text{Eq. 4.27}$$

$$D'_{12} = m^2n^2D_{11} + m^2n^2D_{22} + (m^4 + n^4)\,D_{12} - 4m^2n^2D_{66}$$

$$+ 2\,(mn^3 - m^3n)\,D_{16} + 2\,(m^3n - mn^3)\,D_{26} \qquad \text{Eq. 4.28}$$

$$D'_{66} = m^2n^2D_{11} + m^2n^2D_{22} - 2m^2n^2D_{12} + (m^2 - n^2)^2D_{66}$$

$$+ 2\,(mn^3 - m^3n)\,D_{16} + 2\,(m^3n - mn^3)\,D_{26} \qquad \text{Eq. 4.29}$$

$$D'_{16} = -m^3nD_{11} + mn^3D_{22} + (m^3n - mn^3)\,D_{12} + 2\,(m^3n - mn^3)\,D_{66}$$

$$+ (m^4 - 3m^2n^2)\,D_{16} + (3m^2n^2 - n^4)\,D_{26} \qquad \text{Eq. 4.30}$$

and

$$D'_{26} = -mn^3D_{11} + m^3nD_{22} + (mn^3 - m^3n)\,D_{12} + 2\,(mn^3 - m^3n)\,D_{66}$$

$$+ (3m^2n^2 - n^4)\,D_{16} + (m^4 - 3m^2n^2)\,D_{26} \;. \qquad \text{Eq. 4.31}$$

The derivation of the classical governing equations for in-plane motion in an orthotropic plate is essentially identical to that for the isotropic plate with the exception of substituting the orthotropic constituitive relations. The resulting equations of motion for an orthotropic plate are

$$A_{11}\frac{\partial^2 u_0}{\partial x^2} + A_{66}\frac{\partial^2 u_0}{\partial y^2} + (A_{12} + A_{66})\frac{\partial^2 v_0}{\partial x \partial y} = \rho h\frac{\partial^2 u_0}{\partial t^2} \qquad \text{Eq. 4.32}$$

and

$$A_{22}\frac{\partial^2 v_0}{\partial y^2} + A_{66}\frac{\partial^2 v_0}{\partial x^2} + (A_{12} + A_{66})\frac{\partial^2 u_0}{\partial x \partial y} = \rho h \frac{\partial^2 v_0}{\partial t^2} \qquad \text{Eq. 4.33}$$

where the subscript 0 indicates the displacements along the midplane of the plate.

As was the case for isotropic materials, these equations predict two modes of propagation. However, because of the anisotropy, the modes are not pure extensional and pure in-plane shear except when propagating along directions of material symmetry. Instead, they are, in general, quasi-extensional and quasi-in-plane shear. This means that each mode will have particle displacement components in the direction of propagation as well as perpendicular to the direction of propagation. The mode with the largest component of its particle displacement in the direction of propagation is the quasi-extensional wave. This is the in-plane mode of interest as again the quasi-in-plane shear has not been observed experimentally in AE signals created by pencil lead breaks.

The dispersion behavior of the quasi-extensional wave is much more complicated than the isotropic case. Because of the anisotropy, the velocity of this mode is dependent on the direction of propagation. The dispersion relations are again obtained by giving the displacement a plane wave form and substituting into the equations of motion. However, to consider the directional dependence, a general form for the displacements must be chosen which includes the direction of propagation. Thus, for a general direction of propagation, l_x is the direction cosine between the direction of propagation and the x axis and l_y is the direction cosine between the direction of propaga-

tion and the y axis. The displacements are then given by

$$u_0 = A_0 \alpha_x e^{i(\omega t - kx l_x - ky l_y)}$$ Eq. 4.34

and

$$v_0 = A_0 \alpha_y e^{i(\omega t - kx l_x - ky l_y)}$$ Eq. 4.35

where A_0 is the amplitude and the α_i's are the particle displacement direction cosines.

Substituting these displacements into the equations of motion and reducing terms yields

$$\begin{bmatrix} A_{11}l_x^2 + A_{66}l_y^2 - \rho h c^2 & (A_{12} + A_{66}) l_x l_y \\ (A_{12} + A_{66}) l_x l_y & A_{66}l_x^2 + A_{22}l_y^2 - \rho h c^2 \end{bmatrix} \begin{bmatrix} \alpha_x \\ \alpha_y \end{bmatrix} = 0$$ Eq. 4.36

where c is the phase velocity and is equal to ω/k. The nontrivial solution for this equation will be obtained when the determinant of the two by two matrix is equal to zero. Setting the determinant equal to zero will yield a quadratic equation in $\rho h c^2$. The two values for the velocity correspond to the quasi-extensional and the quasi-shear mode. In general, the quasi-extensional mode is the faster of the two modes and thus will be the root computed with the positive radical in the quadratic formula. This can be verified by computing the particle displacement direction cosines, α_i, which are the eigen vectors, for both velocities. These determine which mode is quasi-extensional and which is quasi-shear.

The solutions for several directions of propagation of interest

are now calculated. The first is for propagation along the x axis or the 0 degree direction of the laminate. In this case, $l_x=1$ and $l_y=0$. Thus, the problem reduces to

$$\det \begin{bmatrix} A_{11} - \rho hc^2 & 0 \\ 0 & A_{66} - \rho hc^2 \end{bmatrix} = 0 \qquad \text{Eq. 4.37}$$

which, of course, has the two solutions

$$c_1 = \sqrt{\frac{A_{11}}{\rho h}} \qquad \text{Eq. 4.38}$$

and

$$c_2 = \sqrt{\frac{A_{66}}{\rho h}} \quad . \qquad \text{Eq. 4.39}$$

The particle displacement direction cosines for c_1 are easily computed and are $\alpha_x=1$ and $\alpha_y=0$. Since $\alpha_x=l_x$ and $\alpha_y=l_y$, the particle displacements are along the direction of propagation. Therefore, it is a pure mode extensional wave. For the in-plane shear mode, $\alpha_x=0$ and $\alpha_y=1$. For this mode, $\alpha_x l_x=\alpha_y l_y=0$ which means that the particle displacements are perpendicular to the direction of propagation. Thus, it is a pure shear mode.

For propagation along the y axis or the 90 degree direction, the extensional mode velocity is given by

$$c_e = \sqrt{\frac{A_{22}}{\rho h}} \quad .$$

<div align="right">Eq. 4.40</div>

Since this is also a symmetry axis of the orthotropic laminate, both modes propagating in this direction are also pure mode. For propagation at 45 degrees between x and y, the direction cosines are given by $l_x = l_y = \frac{\sqrt{2}}{2}$. Both modes become quasi-modes and the quasi-extensional velocity is given by

$$c_e = \sqrt{\frac{(A_{11} + 2A_{66} + A_{22}) + \sqrt{R}}{4\rho h}}$$

<div align="right">Eq. 4.41</div>

where

$$R = (A_{11} + 2A_{66} + A_{22})^2 - 4(A_{11} + A_{66})(A_{22} + A_{66}) + 4(A_{12} + A_{66})^2$$

<div align="right">Eq. 4.42</div>

Thus, the calculation of the quasi-extensional velocity for off-axis propagation is much more complicated and is affected by all of the elastic moduli.

Another method for calculating the dispersion behavior as a function of angle in an orthotropic plate is to first rotate the axes so that the direction of propagation is along the x' direction. The rotated coordinate axes are x' and y' which remain orthogonal and in the plane of the plate. The angle between x and x' is θ and is positive if the rotation is counterclockwise from the unprimed axes. For such a coordinate transformation, the in-plane elastic stiffnesses, A_{ij}', are given in Eq. 4.20 to Eq. 4.25 where, in gener-

al, all six A_{ij}', are nonzero. The equations of motion are then red-
erived in terms of the x'-y' coordinate system to include all six
A_{ij}' and the u' and v' displacements. They become

$$A_{11}' \frac{\partial^2 u_0'}{\partial x'^2} + A_{66}' \frac{\partial^2 u_0'}{\partial y'^2} + (A_{12}' + A_{66}') \frac{\partial^2 v_0'}{\partial x' \partial y'}$$

$$+ \; A_{16}' \frac{\partial^2 v_0'}{\partial x'^2} + 2A_{16}' \frac{\partial^2 u_0'}{\partial x' \partial y'} + A_{26}' \frac{\partial^2 v_0'}{\partial y'^2} \; = \; \rho h \frac{\partial^2 u_0'}{\partial t^2} \qquad \text{Eq. 4.43}$$

and

$$A_{16}' \frac{\partial^2 u_0'}{\partial x'^2} + A_{26}' \frac{\partial^2 u_0'}{\partial y'^2} + (A_{12}' + A_{66}') \frac{\partial^2 u_0'}{\partial x' \partial y'}$$

$$+ \; A_{66}' \frac{\partial^2 v_0'}{\partial x'^2} + 2A_{26}' \frac{\partial^2 v_0'}{\partial x' \partial y'} + A_{22}' \frac{\partial^2 v_0'}{\partial y'^2} \; = \; \rho h \frac{\partial^2 v_0'}{\partial t^2} \qquad . \qquad \text{Eq. 4.44}$$

A plane wave propagating along x' which has displacements of the form

$$u_0' \; = \; A_0 \alpha_{x'} e^{i(\omega t - kx')} \qquad \text{Eq. 4.45}$$

and

$$v_0' \; = \; A_0 \alpha_{y'} e^{i(\omega t - kx')} \qquad \text{Eq. 4.46}$$

is then substituted into the equations of motion. The resulting dis-

person relation for the quasi-extensional mode is

$$c_e = \sqrt{\frac{A'_{11} + A'_{66} + \sqrt{(A'_{11} - A'_{66})^2 + 4A'^2_{16}}}{2\rho h}} \qquad . \qquad \text{Eq. 4.47}$$

The derivation of the equation of motion for flexural wave propa-
gation was presented by Graff [31] for an isotropic material. The
only change needed to extend this derivation to anisotropic media
is the use of the anisotropic constituitive relations which was in-
cluded by Whitney [46]. In these derivations, a differential volume
element of the plate is considered. The element has a thickness of
h which is also the thickness of the plate and has lateral dimensions
of dx by dy. As usual, the x and y axes are in the plane of the plate
and the z axis is normal to the plate with its origin at the midplane
of the plate. This differential element is shown in Figure 4.1 with
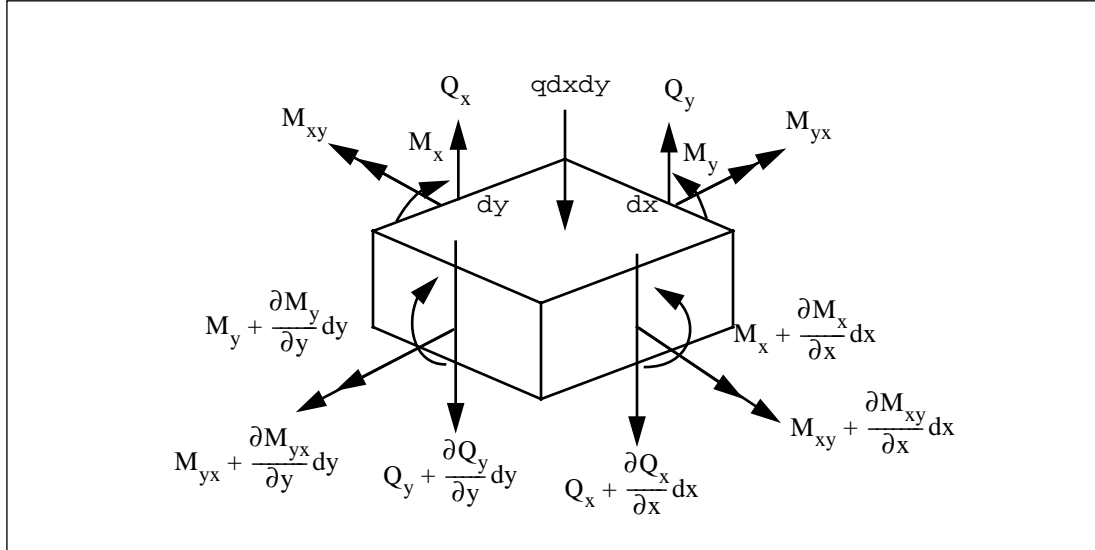
Figure 4.1   Differential element of thin plate exhibiting mo-
            ments and forces.

the bending and twisting moments, normal loading, and shear forces exhibtited. The bending moments per unit length, M_x and M_y, arise from distributions of normal stresses, σ_x and σ_y. The twisting moments per unit length, M_{xy} and M_{yx}, come about because of shearing stresses, τ_{xy} and τ_{yx} while the shear forces per unit length, Q_x and Q_y, are caused by the shear stresses, τ_{xz} and τ_{yz}.

The forces in the x, y, and z directions can now be balanced. This results in three equations of motion. Along z, the equation of motion is

$$(-Q_x)\,dy + \left(Q_x + \frac{\partial Q_x}{\partial x}dx\right)dy - Q_y\,dx + \left(Q_y + \frac{\partial Q_y}{\partial y}dy\right)dx$$

$$+ \; q\,dxdy = \rho h\,dxdy\frac{\partial^2 w}{\partial t^2} \qquad \text{Eq. 4.48}$$

where the term on the right side of the equation is the mass * acceleration restoring force. The displacement w is the displacement of the midplane of the plate. Higher order contributions to the moments caused by the normal loading q have been neglected. The equations along the x and y axes are

$$\left(M_y + \frac{\partial M_y}{\partial y}dy\right)dx - M_y\,dx + M_{xy}\,dy$$

$$- \left(M_{xy} + \frac{\partial M_{xy}}{\partial x}dx\right)dy - Q_y\,dxdy = 0 \qquad \text{Eq. 4.49}$$

and

$$\left(M_x + \frac{\partial M_x}{\partial x} dx \right) dy - M_x dy - M_{yx} dx$$

$$+ \left(M_{yx} + \frac{\partial M_{yx}}{\partial y} dy \right) dx - Q_x dx dy = 0 \qquad \text{Eq. 4.50}$$

where rotatory inertia effects have also been neglected. These equations are reduced by cancelling terms to

$$\frac{\partial Q_x}{\partial x} + \frac{\partial Q_y}{\partial y} + q = \rho h \frac{\partial^2 w}{\partial t^2} \quad , \qquad \text{Eq. 4.51}$$

$$\frac{\partial M_y}{\partial y} - \frac{\partial M_{xy}}{\partial x} - Q_y = 0 \quad , \qquad \text{Eq. 4.52}$$

and

$$\frac{\partial M_x}{\partial x} + \frac{\partial M_{yx}}{\partial y} - Q_x = 0 \quad . \qquad \text{Eq. 4.53}$$

Q_x and Q_y are then solved using the last two equations and substituted back into Eq. 4.51. This yields one equation of motion in terms of the moments and the normal loading as

$$\frac{\partial^2 M_x}{\partial x^2} + \frac{\partial^2 M_{yx}}{dx dy} - \frac{\partial^2 M_{xy}}{dy dx} + \frac{\partial^2 M_y}{\partial y^2} + q = \rho h \frac{\partial^2 w}{\partial t^2} \quad . \qquad \text{Eq. 4.54}$$

The relationships between the moments and the displacements are now considered. Assuming the plate is symmetric allows the moments to be written in terms of the curvatures from Eq. 4.17 as

$$\begin{bmatrix} M_x \\ M_y \\ M_{xy} \end{bmatrix} = \begin{bmatrix} D_{11} & D_{12} & D_{16} \\ D_{12} & D_{22} & D_{26} \\ D_{16} & D_{26} & D_{66} \end{bmatrix} \begin{bmatrix} \kappa_x \\ \kappa_y \\ \kappa_{xy} \end{bmatrix} \ . \qquad \text{Eq. 4.55}$$

The curvatures were given in terms of the displacements in Eq. 4.14 to Eq. 4.16 and can be substituted into Eq. 4.54. Reducing terms yields the classical flexural equation of motion for an orthotropic composite material as

$$D_{11}\frac{\partial^4 w}{\partial x^4} + 4D_{16}\frac{\partial^4 w}{\partial x^3 \partial y} + 2\left(D_{12} + 2D_{66}\right)\frac{\partial^4 w}{\partial x^2 \partial y^2}$$

$$+ \ 4D_{26}\frac{\partial^4 w}{\partial x \partial y^3} + D_{22}\frac{\partial^4 w}{\partial y^4} + \rho h \frac{\partial^2 w}{\partial t^2} = q \quad . \qquad \text{Eq. 4.56}$$

If the composite is symmetric and has only plies in the 0 and 90 degree directions, the composite is specially orthotropic and D_{16} and D_{26} are both zero. In this case the equation of motion reduces to

$$D_{11}\frac{\partial^4 w}{\partial x^4} + 2\left(D_{12} + 2D_{66}\right)\frac{\partial^4 w}{\partial x^2 \partial y^2} + D_{22}\frac{\partial^4 w}{\partial y^4} + \rho h \frac{\partial^2 w}{\partial t^2} = q \quad . \qquad \text{Eq. 4.57}$$

The dispersion behavior for the flexural mode is again determined by substituting the displacement for a plane wave propagating in an arbitrary direction into the equation of motion. This

displacement is of the form

$$w = A_0 e^{i(\omega t - kl_x x - kl_y y)} \quad .$$

Eq. 4.58

Substitution into Eq. 4.56 and reducing terms yields

$$c_f = \sqrt[4]{\frac{S}{\rho h}} \sqrt{\omega}$$

Eq. 4.59

for the dispersion relation for an orthotropic composite where

$$S = D_{11} l_x^4 + 4D_{16} l_x^3 l_y + 2(D_{12} + 2D_{66}) l_x^2 l_y^2 + 4D_{26} l_x l_y^3 + D_{22} l_y^4$$

Eq. 4.60

For the case of a specially orthotropic material, substitution into Eq. 4.57 yields

$$c_f = \sqrt[4]{\frac{D_{11} l_x^4 + 2(D_{12} + 2D_{66}) l_x^2 l_y^2 + D_{22} l_y^4}{\rho h}} \sqrt{\omega} \quad .$$

Eq. 4.61

The predicted dispersion is again a function of frequency as was the case for the isotropic material with the higher frequencies travelling with higher velocities.

It is noted that the dispersion can also be obtained by first rotating to a primed coordinate system with the direction of propagation along the x' axis as was done for the extensional mode dispersion equations. Solution in this manner yields

$$c_f = \sqrt[4]{\frac{D_{11}'}{\rho h}} \sqrt{\omega}$$

<div align="right">Eq. 4.62</div>

where D_{11}' is given in Eq. 4.26.

The solution for the displacement of the flexural mode created by a step function forcing function in a specially orthotropic finite plate can be obtained using the normal mode expansion technique. The approach is exactly the same as was demonstrated for the isotropic aluminum. Again, the plate dimensions are given by a thickness h, length along the x direction a, and width along the y direction b. The point loading source of amplitude P is at x=ξ and y=ζ while the receiver is located at x and y. The resulting solution,

$$w(x,y,t) = \frac{4P}{\rho hab} \sum_{n=1}^{\infty} \sum_{m=1}^{\infty} \frac{\sin\alpha_n x \sin\gamma_m y \sin\alpha_n \xi \sin\gamma_m \zeta (1 - \cos\omega_{nm}t)}{\omega_{nm}^2}$$

<div align="right">Eq. 4.63</div>

is of the same form as that for aluminum except that the frequency is now given by

$$\omega_{nm} = \sqrt{\frac{D_{11}\alpha_n^4 + D_{22}\gamma_m^4 + 2(D_{12} + 2D_{66})\alpha_n^2\gamma_m^2}{\rho h}}$$

<div align="right">Eq. 4.64</div>

where

$$\alpha_n = \frac{n\pi}{a}$$

<div align="right">Eq. 4.65</div>

and

$$\gamma_m = \frac{m\pi}{b} \ .$$

Eq. 4.66

Experimental measurements of the dispersion of the flexural mode in composites, which are presented in the next section, were not in good agreement with the predictions of classical plate theory, especially at higher frequencies. This is because of the effects of shear and rotatory inertia which are neglected by classical plate theory. These effects are more significant for the composites than they were for isotropic aluminum because of the relatively low transverse shear modulus in composites. This limitation on classical plate theory also leads to discrepancies between the normal mode solutions and experimental waveforms.

The dispersion behavior for composites based on a higher order theory which includes the effects of shear deformation and rotatory inertia was also calculated. This theory was put forth by Tang et al. [48] following earlier work by Yang et al. [49]. This was an extension of the work by Mindlin [50] on the effect of shear and rotatory inertia on the flexural motion of isotropic plates. The details of the derivation of this theory are not presented here. However, the predicted dispersion behavior for a symmetric orthotropic laminate predicted by this theory is presented. It is obtained when the determinant of the following matrix of coefficients is set equal to zero

$$\begin{vmatrix} M_{11} & M_{12} & M_{13} \\ M_{21} & M_{22} & M_{23} \\ M_{31} & M_{32} & M_{33} \end{vmatrix}$$

Eq. 4.67

where

$$M_{11} = D_{11}k^2l_x^2 + 2D_{16}k^2l_xl_y + D_{66}k^2l_y^2 + A_{55} - I\omega^2 \qquad \text{Eq. 4.68}$$

$$M_{12} = D_{16}k^2 + (D_{12} + D_{66})\,k^2l_xl_y \qquad \text{Eq. 4.69}$$

$$M_{13} = iA_{55}kl_x \qquad \text{Eq. 4.70}$$

$$M_{21} = D_{16}k^2 + (D_{12} + D_{66})\,k^2l_xl_y \qquad \text{Eq. 4.71}$$

$$M_{22} = D_{66}k^2l_x^2 + 2D_{16}k^2l_xl_y + D_{22}k^2l_y^2 + A_{44} - I\omega^2 \qquad \text{Eq. 4.72}$$

$$M_{23} = iA_{44}kl_y \qquad \text{Eq. 4.73}$$

$$M_{31} = -iA_{55}kl_x \qquad \text{Eq. 4.74}$$

$$M_{32} = -iA_{44}kl_y \qquad \text{Eq. 4.75}$$

and

$$M_{33} = A_{55}k^2l_x^2 + A_{44}k^2l_y^2 - \rho^*\omega^2 \quad . \qquad \text{Eq. 4.76}$$

In the previous equations,

$$(\rho^*,I) = \int_{z=-\frac{h}{2}}^{z=\frac{h}{2}} \rho\,(1,z^2)\,dz \qquad , \qquad \text{Eq. 4.77}$$

and

$$A_{ij} = k_i k_j \int_{z=-\frac{h}{2}}^{z=\frac{h}{2}} (Q_{ij})_k dz \qquad \text{for } i,j = 4,5. \qquad \text{Eq. 4.78}$$

In Eq. 4.78, the k_i are shear correction factors which were deter-
mined to yield the best agreement with exact theory when $k_i{}^2 = 5/6$.
The subscript k refers to the k'th layer of the laminate. Solving the
determinant for the wavenumber as a function of ω yields a cubic in
k^2. Only the root which approaches zero as the frequency approaches
zero is the correct root. Once k as a function of ω is known, the
phase velocity, c_f, is determined as a function of frequency using
the relation

$$c_f = \frac{\omega}{k} \qquad . \qquad \text{Eq. 4.79}$$

IV.3 Dispersion measurements in composite plates

Measurements of the extensional velocities and the flexural dis-
persion in four composite laminates are now presented. The measure-
ments were made along three directions in all of the laminates. These
were the 0 degree direction or along the x axis of the laminate,
the 90 degree direction or along the y axis of the laminate, and
along the 45 degree direction. The extensional velocities were com-
pared with predictions from classical plate theory. The flexural dis-
persion measurements were compared with predictions from both
classical plate theory and the higher order plate theory.

The composite laminates investigated were all manufactured from
prepregs consisting of AS4 fibers (Hercules) in a 3502 epoxy resin.

They were laid up and cured as per the manufacturers instructions. Each laminate consisted of 16 plies with a nominal thickness of 2.26 mm. The length along the x direction of each laminate was 0.508 m. while the width along the y direction was 0.381 m. The four layups were $[0_{16}]$, $[0_4,90_4]_s$, $[0,90]_{4s}$, and $[0,45,-45,90]_{2s}$.

In the measurement of the extensional velocities, the plate modes were generated by pencil lead breaks. The waves were detected with the 3.5 MHz ultrasonic transducer and preamplified by 40 dB with no filtering. A signal from a R15 transducer positioned next to the source was used to trigger the digitizer which recorded the waveforms at a 5 MHz sampling frequency. The captured waveforms were trans-ferred to a personal computer for storage and analysis. A block dia-gram of the experimental apparatus is shown in Figure 4.2.
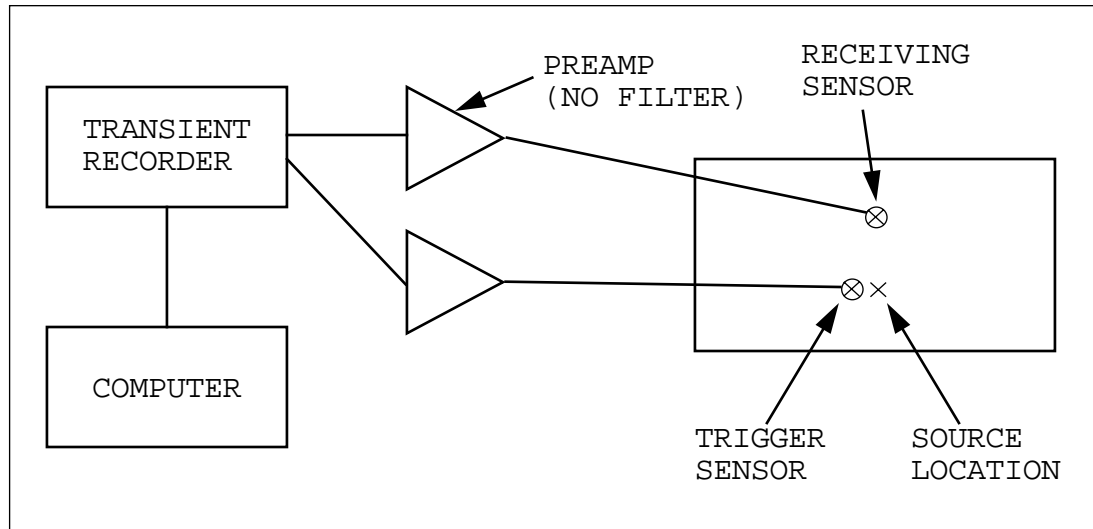
Figure 4.2   Block diagram of experimental apparatus used to measure extensional velocities in composite plates.

While the source position was maintained constant, the receiving transducer was moved back in increments of 2.54 cm. and the lead breaks repeated. Measurements were made over the source to receiver

distance range of 7.62 cm. to 17.78 cm. For all measurement direc-
tions, the source and receiving transducer were positioned as far
away from plate edges as possible to avoid complications from reflec-
tions. The earliest arrival of the extensional mode relative to the
trigger time was recorded at each distance. Then, for a given direc-
tion of propagation, the arrival times versus distances were
plotted and a least squares linear fit determined for the data. The
slope of the line provided the velocity for that direction of propa-
gation. A plot of the data and fit for propagation in the 90 degree
direction of the $[0_{16}]$ plate is exhibited in Figure 4.3 as a typical
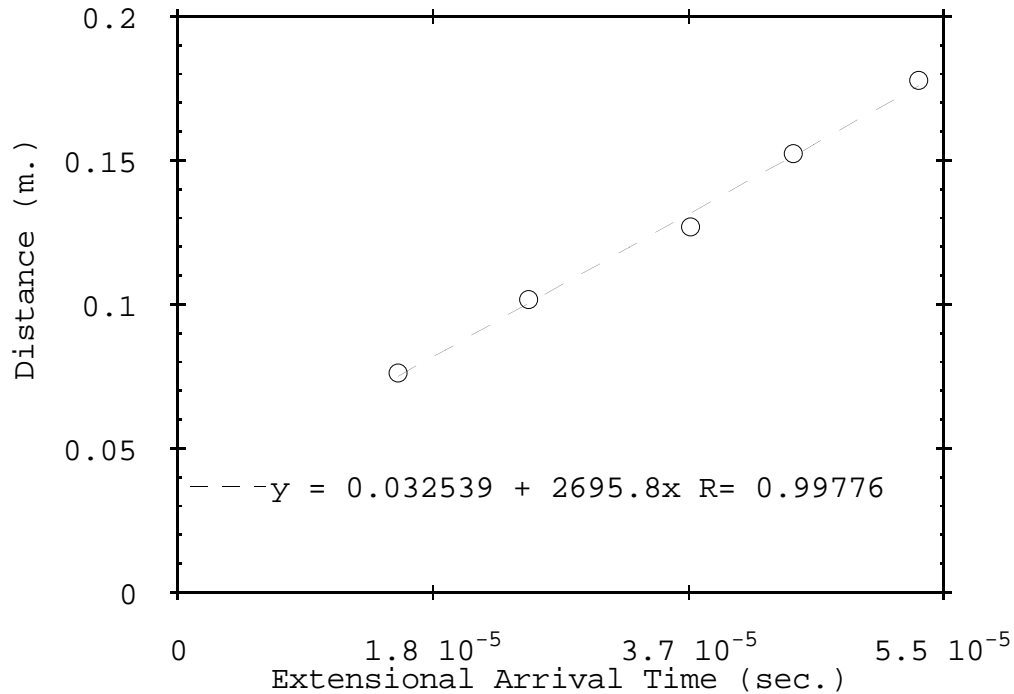
Figure 4.3   Plot of extensional arrival time versus distance
of propagation for 90 degree propagation in $[0_{16}]$
graphite/epoxy plate.

example. It is noted that the fitted line does not pass through zero.
This was because of the delay time in triggering the transient re-
corder for each measurement. This delay time was a constant and was
caused by the finite time required for the signal from the trigger

sensor to reach the trigger threshold voltage.

The nominal lamina material properties obtained from Dr. Doug Chairns [51] at the prepreg manufacturer (Hercules) used in the theoretical calculations are presented in Table 4.1. It was noted by him,

Lamina thickness = 1.413×10^{-4} m.

Density = 1550 kg/m^3

Fiber volume = 60%

Q_{xx} = 145.5 GPa. Q_{xy} = 2.91 GPa Q_{yy} = 9.69 GPa Q_{ss} = 5.97 GPa

Table 4.1   Lamina properties of AS4/3502 graphite epoxy.

however, that the actual properties of this material could vary significantly depending on cure conditions, length of time of prepreg storage before use, and minor variations in resin chemistry and fiber volume content. This has been observed by many researchers in composite materials. For example, Prosser [52] measured the complete set of linear elastic moduli T300/5208 graphite/epoxy. Several of the moduli were significantly less than the nominal properties for that material with one that was measured to be 30 percent less.

The measured and theoretical extensional velocities for all four laminates are shown in Table 4.2. The measured velocities were consistently lower than the predicted velocities with the exceptions of the 90 degree measurements in the $[0_{16}]$ and the $[0_4,90_4]_s$ plates and the 45 degree measurement in the $[0_{16}]$ laminate. With these exceptions, the measured velocities were all in the range of two to nine percent less than the theoretical velocities. This indicated that the manufacturer's properties used in the calculation were somewhat higher than those in the actual material. The 45 degree $[0_{16}]$

Laminate	Direction of Propagation	Measured Velocity (m/s)	Theoretical Velocity (m/s)
$[0_{16}]$	0	9020	9690
	45	3510	7004
	90	2700	2500
$[0_4, 90_4]_s$	0	6380	7087
	45	5210	5469
	90	7300	7087
$[0, 90]_{4s}$	0	6550	7087
	45	5020	5469
	90	6450	7087
$[0, 45, -45, 90]_{2s}$	0	6050	6321
	45	5990	6322
	90	5750	6321

Table 4.2   Measured and theoretical extensional velocities for AS4/3502 graphite/epoxy laminates.

measurement was much less than theoretically predicted. It is not known why this discrepancy occurred and further investigation is needed. The remaining two exceptions, propagation at 90 degrees in the $[0_{16}]$ and the $[0_4, 90_4]_s$ laminates, were only slightly higher than predicted values.

The velocity of the flexural mode was also measured in the four plates. Measurement of the first arrival time of this mode to calculate the velocity was inadequate because of its dispersive nature. Thus, a Fourier phase spectra technique was used which enabled measurements of the phase velocity over a range of frequencies. These measurements were then compared with predictions based on classical plate theory and higher order plate theory.

The Fourier phase technique for measuring velocities in dispersive

media has been used by a number of authors including Sachse and Pao [53], Pao and Sachse [54], Veidt and Sayir [55], Dean [56], and Alleyne and Cawley [57]. Sachse and Pao [53] used this technique to characterize the dispersion of ultrasonic bulk waves and extensional rod waves. Both Veidt and Sayir [55] and Dean [56] used this technique to characterize similar flexural waves in polymer and composite plates.

In the Fourier phase technique, the elastic wave is detected at two different distances away from the source of the wave along the direction of propagation of interest. The phase (φ) of the wave at each position at a given frequency is determined by performing a Fourier Transform on the signals and computing the phase. The phase difference ($\Delta\varphi$) over the distance between the two transducers (Δx) is then computed for each frequency. The wave number (k) and velocity (c) are then calculated at each frequency by

$$k(f) = \frac{\Delta\varphi(f)}{\Delta x} \qquad \text{Eq. 4.80}$$

and

$$c(f) = \frac{2\pi f}{k(f)} = \frac{2\pi f \Delta x}{\Delta\varphi(f)} \qquad . \qquad \text{Eq. 4.81}$$

The difficulty in this technique arises from the fact that there is a $2n\pi$ uncertainty, where n is an integer, in evaluating the phase of the wave at any given frequency. Thus, there is the same uncertainty in calculating the change in phase over the distance of propagation between the two sensors. This has been handled in different ways in past research. Sachse and Pao [53] unwrapped the phase by

starting at the lowest frequency and adding 2π to the phase value
each time a discontinuity in the slope of the phase occurred. Dean
[56] time shifted the record of the second transducer until a refer-
ence phase point on the second record was at the same point in time
as the same reference phase point on the record of the first trans-
ducer. The actual phase difference was then given by the measured
phase difference plus the time shift multiplied by $2\pi f$ where f is the
frequency. Since he was using an ultrasonic transducer with a
pulser as his source, he was able to monitor the reference point as
the transducer distance was gradually increased to the second mea-
surement distance.

In this research, a combination of two approaches was applied to
circumvent the problem of $2n\pi$ phase uncertainties. First, measure-
ment of the phase change along a given direction of propagation was
repeated for several different distances. If the velocity over
these different distances is a constant, the change in phase per unit
distance of propagation, $\frac{\Delta\varphi}{\Delta x}$, should be the same for all measure-
ments. Thus, a computer algorithm was developed which added integer
multiples of 2π to the measured phase differences, computed $\frac{\Delta\varphi}{\Delta x}$ for
each measurement, and then determined when they were most nearly
equal for all of the measurements. This does not fully eliminate
the problem as there will be various multiples of integers which will
satisfy the constraint that the change in phase per unit distance
be the same at all measured distances.

To determine which set of integers yields the correct phase
change, another constraint was applied. The constraint was based on
the assumption that the velocity of the flexural mode approaches zero
as the frequency approaches zero which is predicted by theory. Addi-

tionally, it was assumed that the velocity change with frequency is smooth with no discontinuity. Based on these assumptions, the phase change at the lowest frequency calculated will be with the lowest set of integers that meet the first condition of minimizing the differences of $\frac{\Delta\varphi}{\Delta x}$ for the measured values. At subsequent frequency values, the set of integers used are those that minimize the differences without allowing a large change in the phase change per distance which would mean a discontinuity in velocity versus frequency. The maximum allowed change in phase difference per unit distance between frequency points which were spaced at approximately 2 kHz intervals was approximately +/- 1 rad./cm. This value was chosen as it was much larger than any expected change per frequency point as predicted by theory, but it was small enough to prevent jumping to higher or lower sets of integers in which the calculated $\frac{\Delta\varphi}{\Delta x}$ values were also nearly equal.

This approach is essentially equivalent to limiting the amount that the phase can change from frequency to frequency which is the approach used to unwrap the phase by Sachse and Pao [53]. The corresponding limits on the velocity change per frequency point that this constraint allows is dependent on frequency.

The experimental setup used for these experiments is shown in Figure 4.4. The two receiving sensors were 3.5 MHz ultrasonic transducers while the trigger sensor was a R15. The preamplifiers were set at 40 dB amplification with no filtering. The source was a pencil lead break repeated with the transducers at separations of 1.91, 2.54, 3.18, 3.81, and 4.45 cm. along propagation directions of 0, 45, and 90 degrees for each plate. The source and receivers were kept as nearly in the center of the plate as possible to minimize reflec-
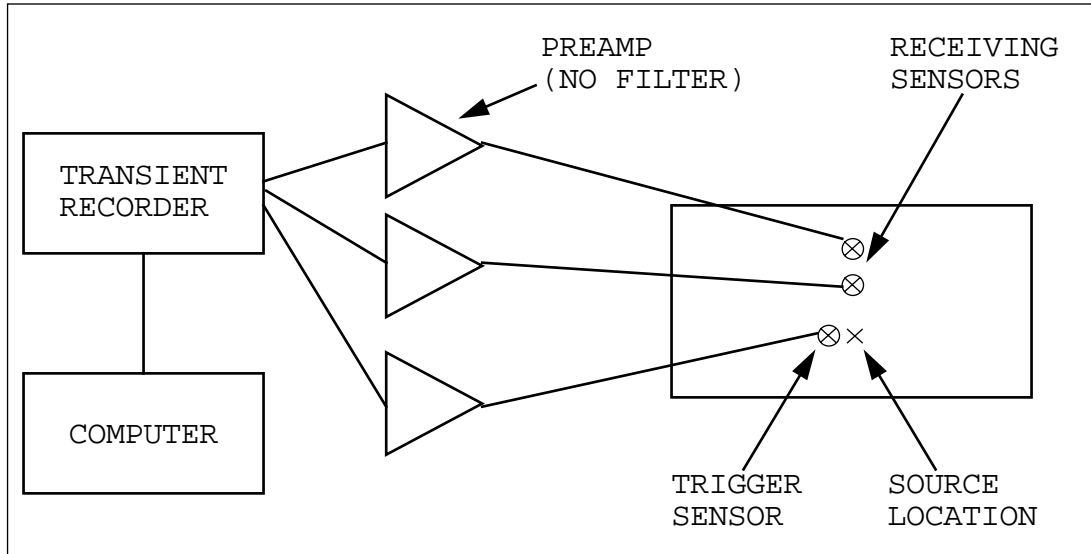
Figure 4.4   Experimental setup for flexural velocity measure-
ments in composite plates.

tions. The waveforms were digitized at a sampling frequency of 1

MHz and then transferred to the personal computer.

Prior to computing the FFT to determine the phase, the higher fre-

quency extensional mode and the reflections arriving later in the

flexural mode were zeroed out in the computer. Previous Fourier anal-

ysis of the flexural mode signals when digitized at much higher sam-

pling frequencies (100 MHz) showed that the maximum frequency

component in the flexural mode was about 200 kHz. Thus, aliasing

was not a concern even at the low sampling frequency of 1 MHz.

Initial processing of the waves consisting of computing the

phase after FFT Fourier Transforming the data was carried out on

the personal computer with the Asyst waveform processing package. The

phase values for each measurement at each frequency over the range of

2 to 160 kHz. were then transferred to another personal computer

(Macintosh IIfx) where the actual $\frac{\Delta \varphi}{\Delta x}$ values and the corresponding

velocities were calculated using a program written in C^{++}. The aver-

age velocity of the five measurements was taken to be the measured velocity while the standard deviation of the measurements was used as the error in the measured velocity.

The measured velocities for the 0, 45, and 90 degree directions in the $[0_{16}]$ graphite epoxy plate are plotted in Figure 4.5 to Figure
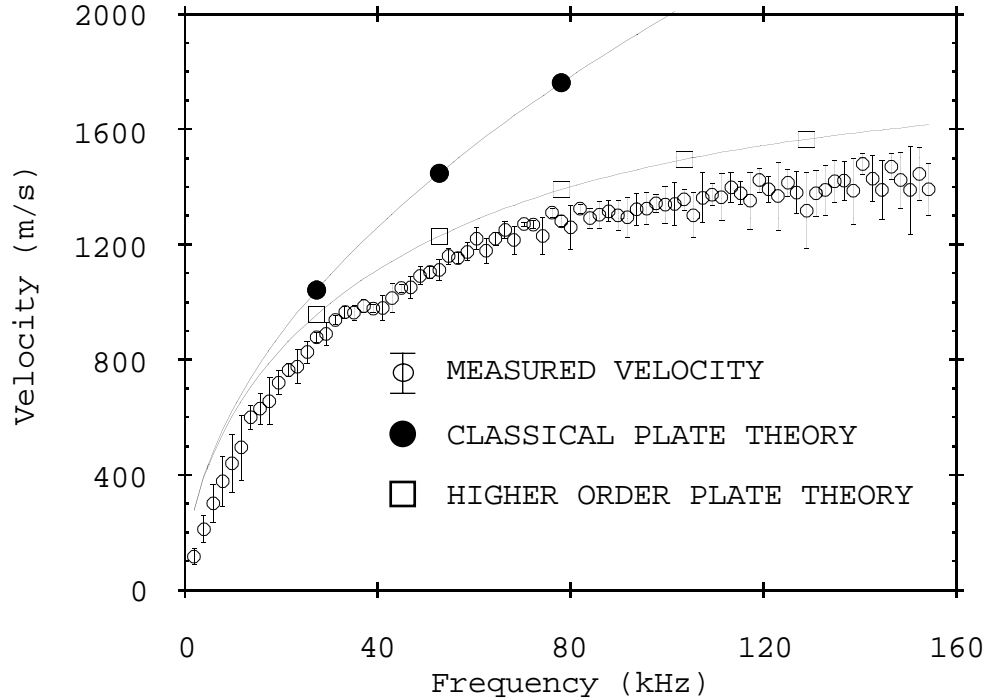
Figure 4.5   Measured and theoretical flexural dispersion for 0 degree propagation in $[0_{16}]$ graphite/epoxy

4.7. The predicted velocity dispersion curves for classical plate theory (CPT) and the higher order plate theory (HOPT) are also shown in these plots. The agreement between measurement and HOPT is excellent for the 90 degree propagation direction. For propagation at 45 and 0 degrees, the measured values are consistently less than those predicted by HOPT. This is consistent with the extensional velocity measurements which were less than theoretical predictions.

The effect of shear and rotatory inertia is clear when the CPT and the HOPT are compared in these plots. CPT and HOPT are in agreement

Figure 4.6   Measured and theoretical flexural dispersion for
45 degree propagation in [0$_{16}$] graphite/epoxy
plate.

Figure 4.7   Measured and theoretical flexural dispersion for
90 degree propagation in [0$_{16}$] graphite/epoxy
plate.

at low frequencies in all cases where the approximations of CPT are valid. The discrepancy between the two increases with increasing frequency as the velocity predicted by CPT increases without bound.

It is also apparent that the difference between HOPT and CPT is much greater for the 0 and 45 degree directions than for the 90 degree direction. This is expected since the shear modulus is much smaller in comparison to the Young's modulus in those directions. CPT is based on the assumption of no shear deformation which implies an infinite shear modulus. Thus, better agreement is provided by CPT when the shear modulus is large with respect to the Young's modulus. Even better agreement occurs in aluminum as is shown in Figure 4.8. This figure plots the difference between CPT and HOPT nor-
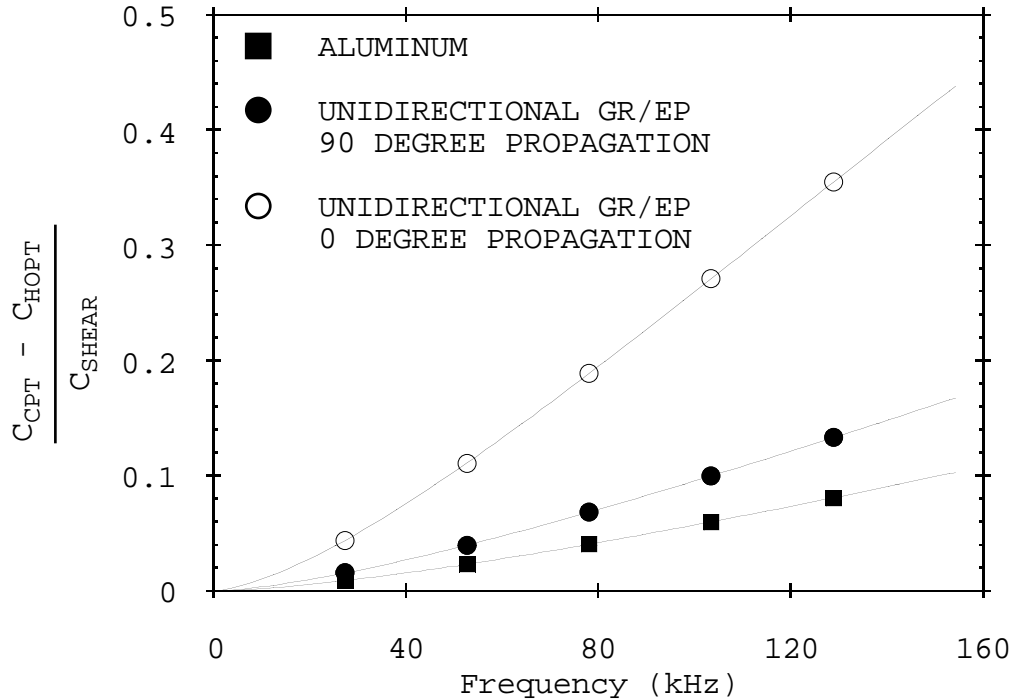
Figure 4.8   Normalized difference between CPT and HOPT flexural dispersion predictions for aluminum and unidirectional gr/ep composite.

malized by the shear velocity for both the aluminum (0.3175 cm. thickness) and the $[0_{16}]$ graphite/epoxy plates. The normalized dif-

ference for aluminum at 160 kHz is about 0.1. This is why such good
agreement was obtained between the CPT normal mode solution and ex-
periment in the last chapter.

Plots of the measured flexural velocity along with the
velocities predicted by CPT and HOPT for the remaining three lami-
nates are shown in Figure 4.9 to Figure 4.17. The measured flexural

Figure 4.9   Measured and theoretical flexural dispersion for
             0 degree propagation in $[0,90]_{4s}$ graphite/epoxy
             plate.

velocity for all three directions of propagation in all three lami-
nates follows the behavior predicted by HOPT except for having values
slightly less than theoretical predictions. This again, is consistent
with the possibility that the values of the material elastic proper-
ties obtained from the manufacturer and used in the theoretical cal-
culations may be somewhat larger than those of the actual material
studied in this research.

In summary, measurements were made of the extensional and flexural
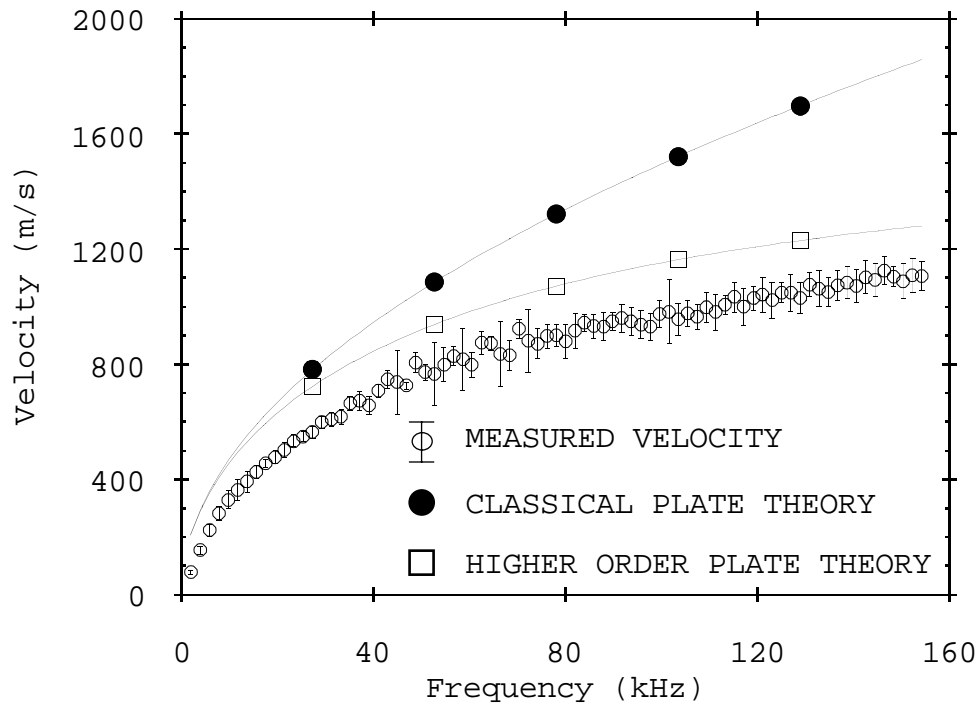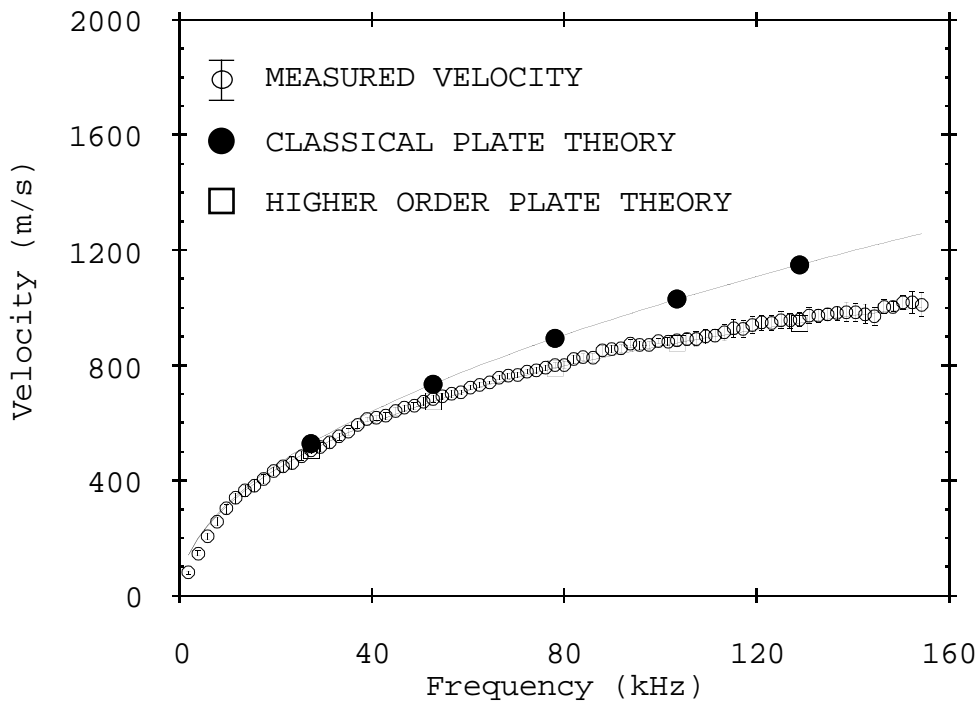
Figure 4.10   Measured and theoretical flexural dispersion for
              45 degree propagation in [0,90]$_{4s}$ graphite/epoxy
              plate.

Figure 4.11   Measured and theoretical flexural dispersion for
              90 degree propagation in [0,90]$_{4s}$ graphite/epoxy
              plate.

Figure 4.12 Measured and theoretical flexural dispersion for 0 degree propagation in $[0_4,90_4]_s$ graphite/epoxy plate.

Figure 4.13 Measured and theoretical flexural dispersion for 45 degree propagation in $[0_4,90_4]_s$ graphite/epoxy plate.
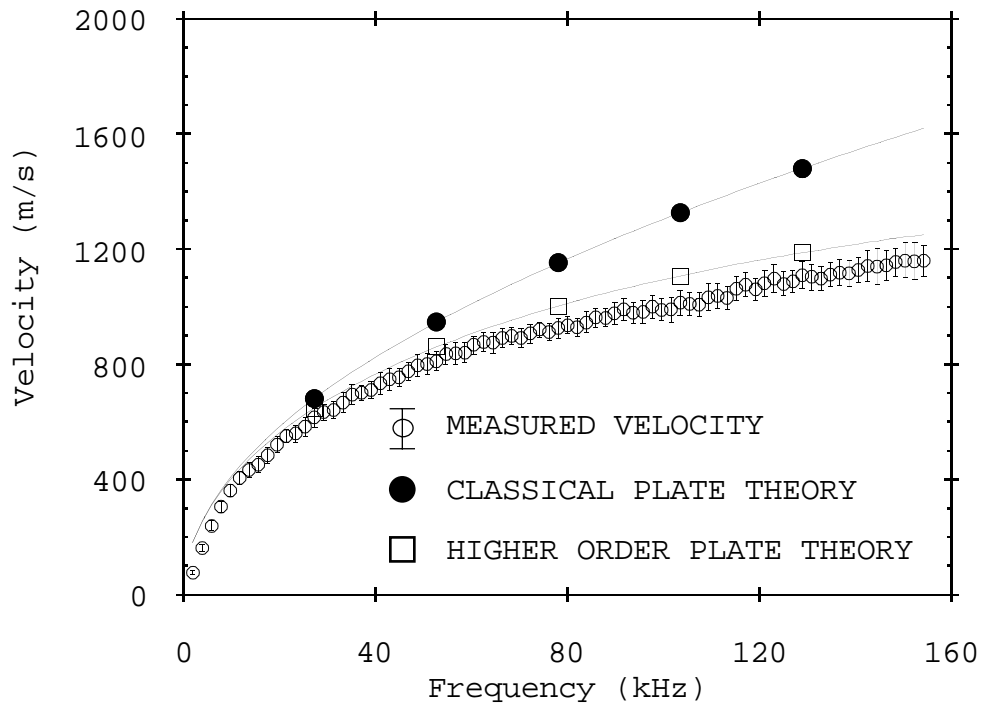
Figure 4.14   Measured and theoretical flexural dispersion for
              90 degree propagation in $[0_4,90_4]_s$ graphite epoxy/
              plate.
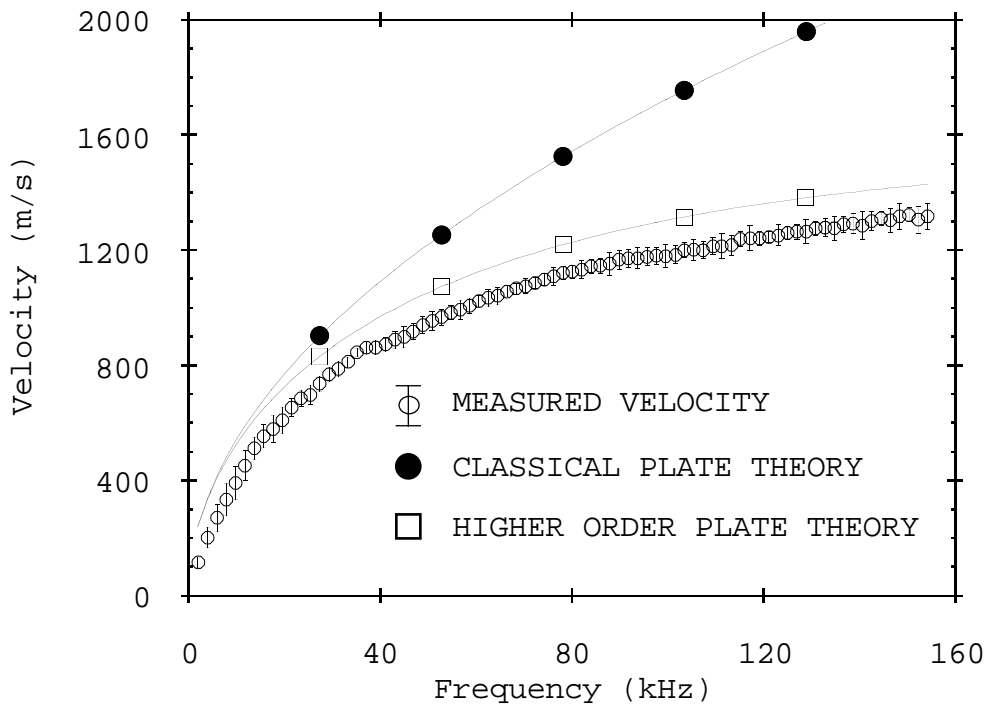
Figure 4.15   Measured and theoretical flexural dispersion for
              0 degree propagation in $[0,45,-45,90]_{2s}$ graphite/
              epoxy plate.
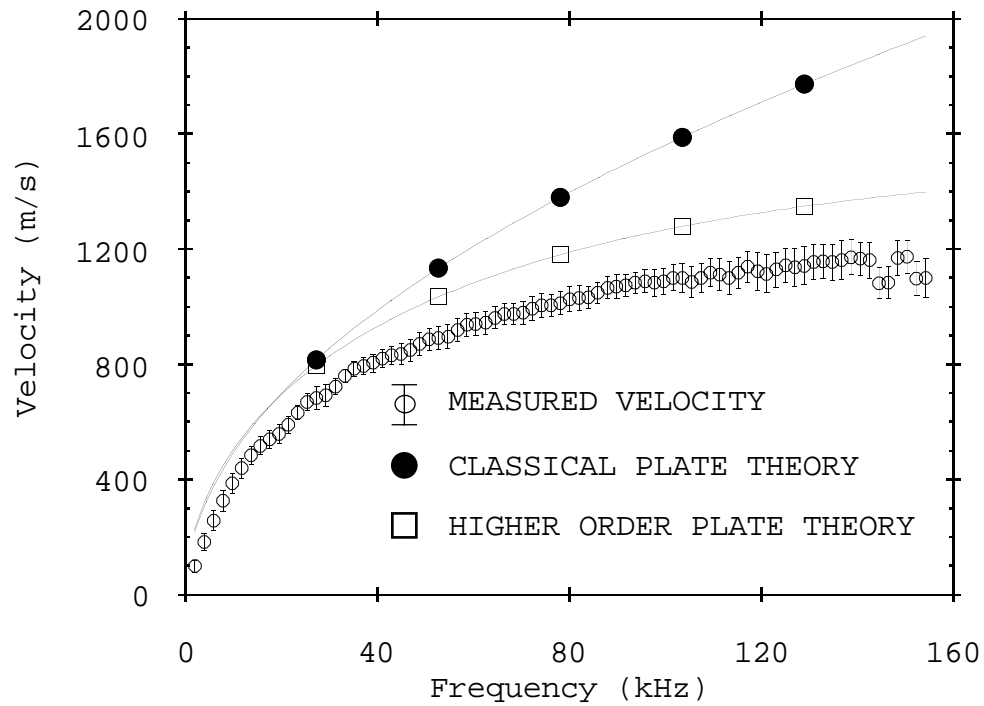
Figure 4.16   Measured and theoretical flexural dispersion for
              45 degree propagation in [0,45,-45,90]$_{2s}$ graphite/
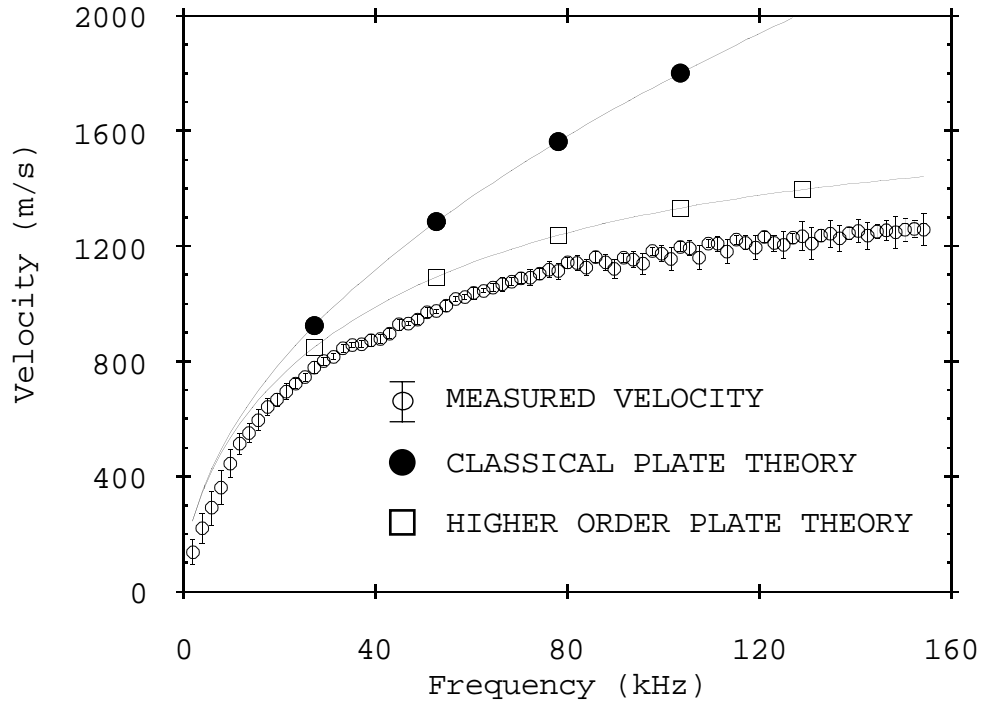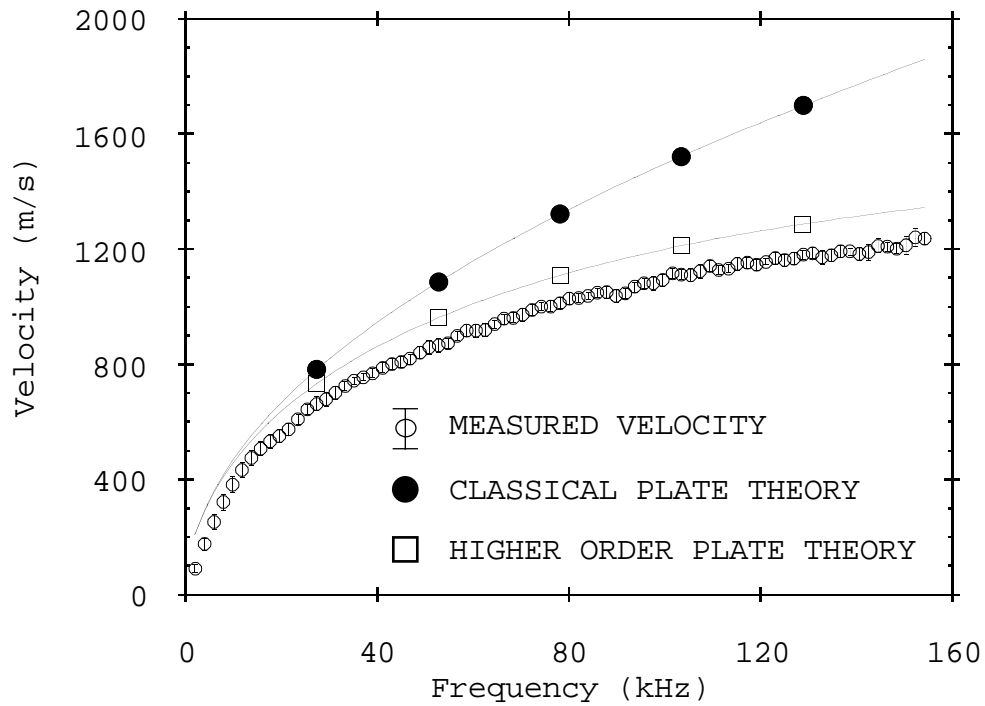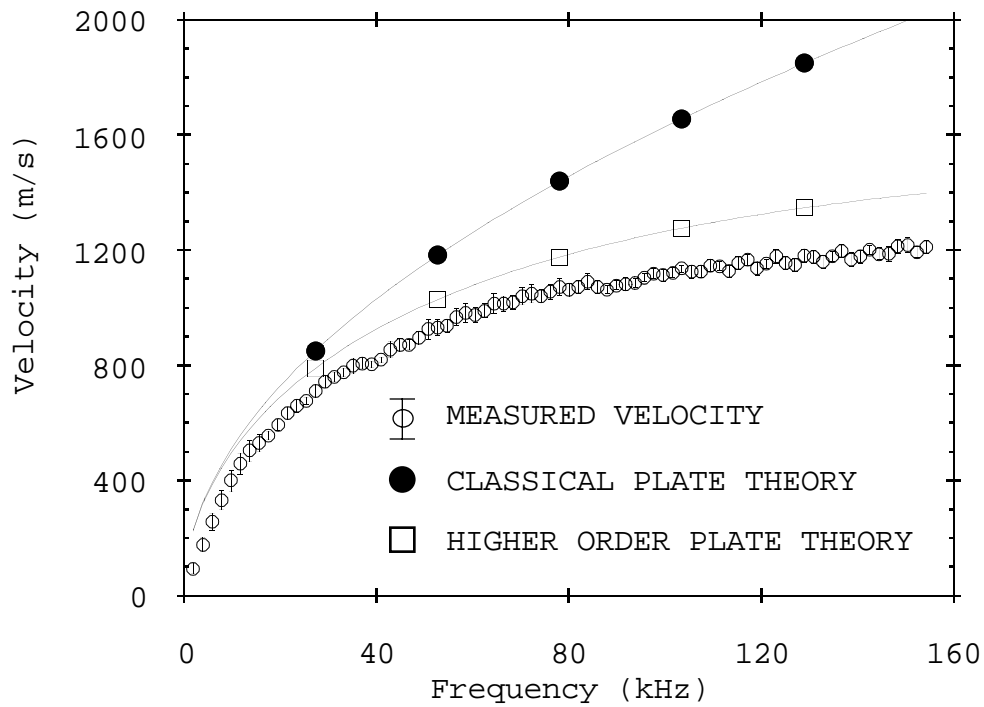   epoxy plate.
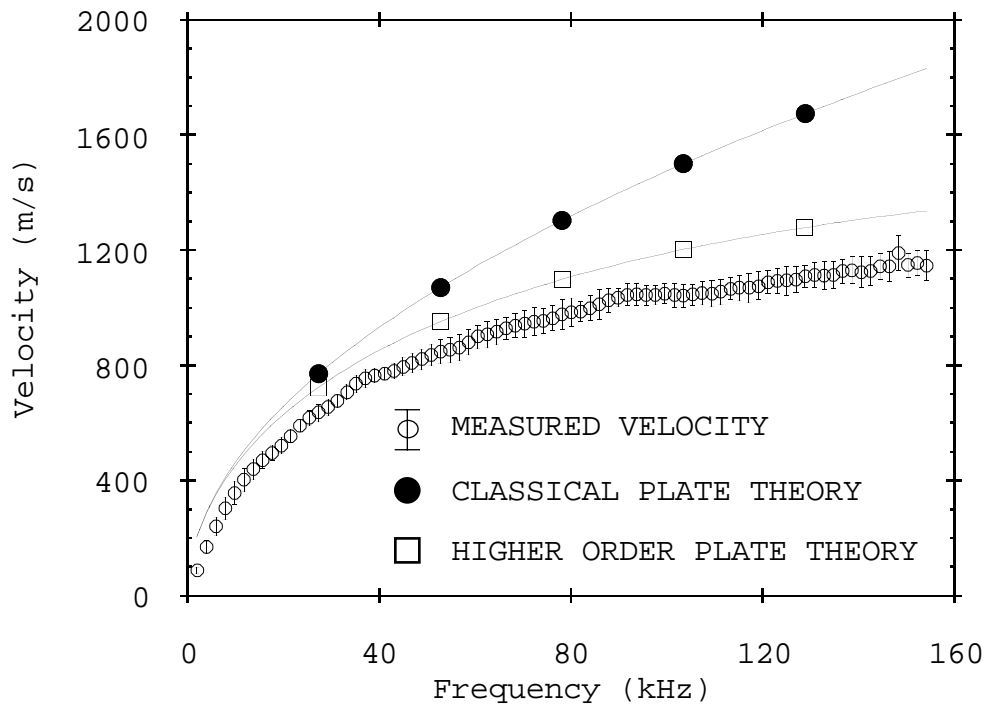
Figure 4.17   Measured and theoretical flexural dispersion for
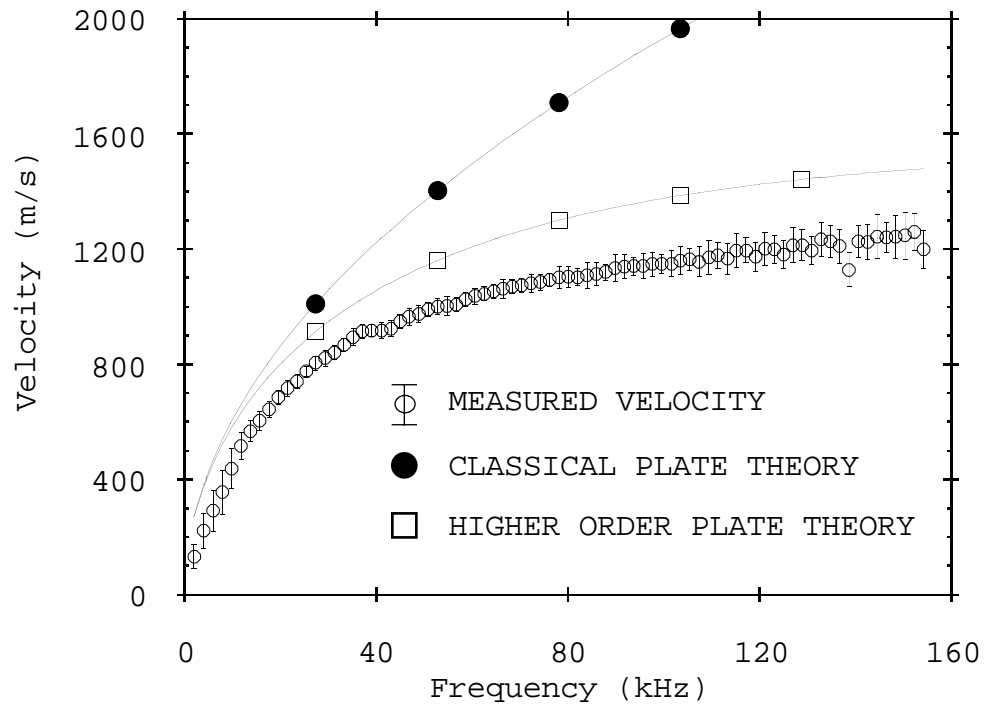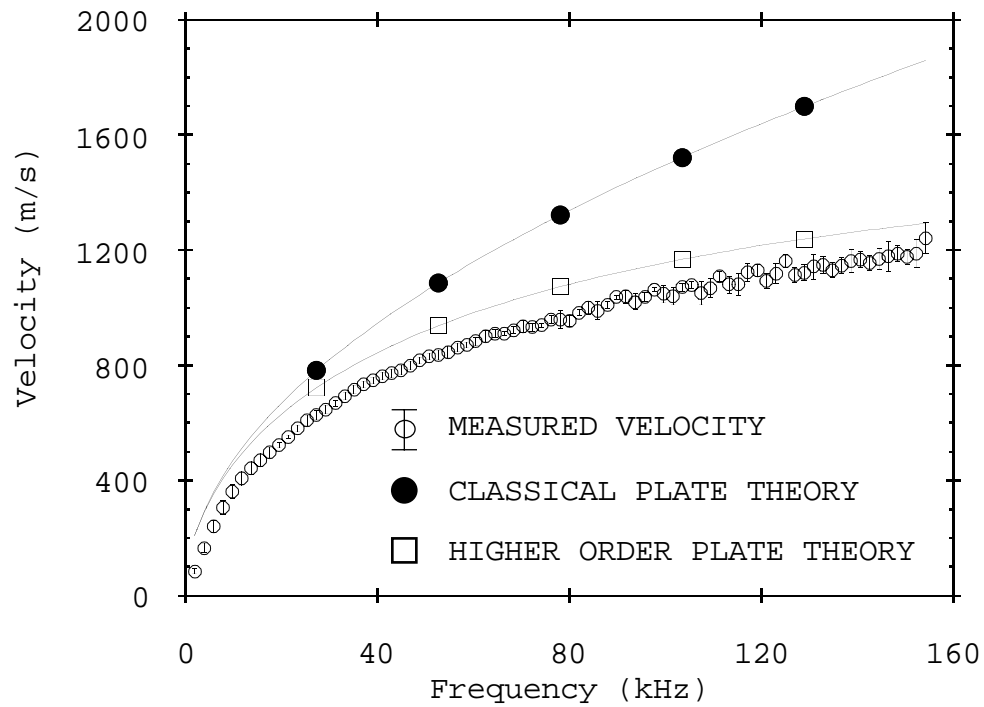   90 degree propagation in [0,45,-45,90]$_{2s}$ graphite/
              epoxy plate.

plate mode velocities in four different graphite epoxy laminates in three different directions. The extensional mode velocity was measured based on its first arrival time while the flexural mode velocity was measured over a range of frequencies up to 160 kHz. because of its dispersive nature. These measurements were compared with predictions based on classical plate theory. In the case of the flexural mode, a comparison was also made with a higher order plate theory which included corrections for the effects of shear deformation and rotatory inertia. These effects were shown to be considerable for the case of the composite materials while they were negligible for aluminum plates.

The measured extensional velocities were, with only a couple of exceptions, two to nine percent less than those predicted by theory. The measured flexural velocities were also consistently less than those predicted by higher order plate theory. The possibility that the material properties used in the calculations were higher than those of the actual material was discussed. This would account for the discrepancy between the measured and theoretical velocities. By making additional measurements along other directions of propagation, it should be possible to invert these measurements to determine the actual material properties.

IV.4 Flexural mode waveforms in composite plates and comparison with predictions based on the normal mode solution technique

In this section, measurements of the flexural mode waveforms generated by pencil lead break sources in composite plates are presented. These measured waveforms are compared with predictions based on the normal mode expansion solution technique to classical plate theo-

ry for a specially orthotropic material. This is an identical experiment to that carried out on isotropic aluminum plates which was discussed in III.4. As the limitations of CPT have already been demonstrated in the flexural dispersion measurements, good agreement between theory and experiment is not expected. Therefore, only two measurement comparisons will be presented which further prove this point. These will be measurements along the 0 and 90 degree directions of propagation for the $[0_{16}]$ composite plate.

The computer program used for the theoretical predictions was similar to that used for the isotropic aluminum calculations with modifications made to account for the anisotropy. The program was based on the theory derived in IV.2 for a specially orthotropic material. The code was written and compiled in the Pascal language and executed on a personal computer (Macintosh IIfx). The filtering of the theoretical waveforms to account for the transducer frequency response was carried out in the same way as discussed previously in III.4. The time needed to compute each theoretical waveform was only marginally slower than that for the isotropic case with a 2048 point waveform requiring 1280 seconds for computation.

The normal mode program revised for special orthotropy was checked by comparing its output to the isotropic program when the input material coefficients obeyed the symmetry laws for an isotropic material. These are

$$D_{11} = D_{22} = D \ , \qquad\qquad \text{Eq. 4.82}$$

$$D_{12} = \nu D \ , \qquad\qquad \text{Eq. 4.83}$$

and

$$D_{66} = \frac{(1-\nu)}{2}D$$

<div align="right">Eq. 4.84</div>

where ν and D are the Poisson's ratio and bending modulus respective-
ly for an isotropic material (aluminum). The outputs of the two pro-
grams were found to be identical as expected.

The experimental apparatus and method was the same as that used in
the aluminum plate experiments. The waveforms were detected with
the ultrasonic transducer and digitized at a 5 MHz sampling frequency
with the transient recorder. The transient recorder was triggered
by the signal from a R15 sensor positioned next to the lead break
source. The signal was preamplified 40 dB without any filtering.
The signal was stored on a personal computer (IBM PC-AT) and then
later transferred to another personal computer (Macintosh IIfx) for
comparison with the theoretical waveforms.

The experimental waveform and the normal mode solution for propa-
gation along the 90 degree direction are shown in Figure 4.18. The
dimensions of the plate were 0.508 m. in length along the fibers
and 0.381 m. in width transverse to the fibers. The source position
was at the center length (0.254 m.) at a distance of 0.127 m. from
the edge. The receiver position was also at the center length at a
distance of 0.127 m. from the source position or 0.254 m. from the
plate edge as demonstrated in Figure 4.19. Agreement between theory
and experiment is not bad along this direction since CPT remains a
good approximation as demonstrated by the dispersion measurements.
However, the agreement is not nearly as good as occurred for the alu-
minum plate where CPT is an even better approximation. Since the nor-
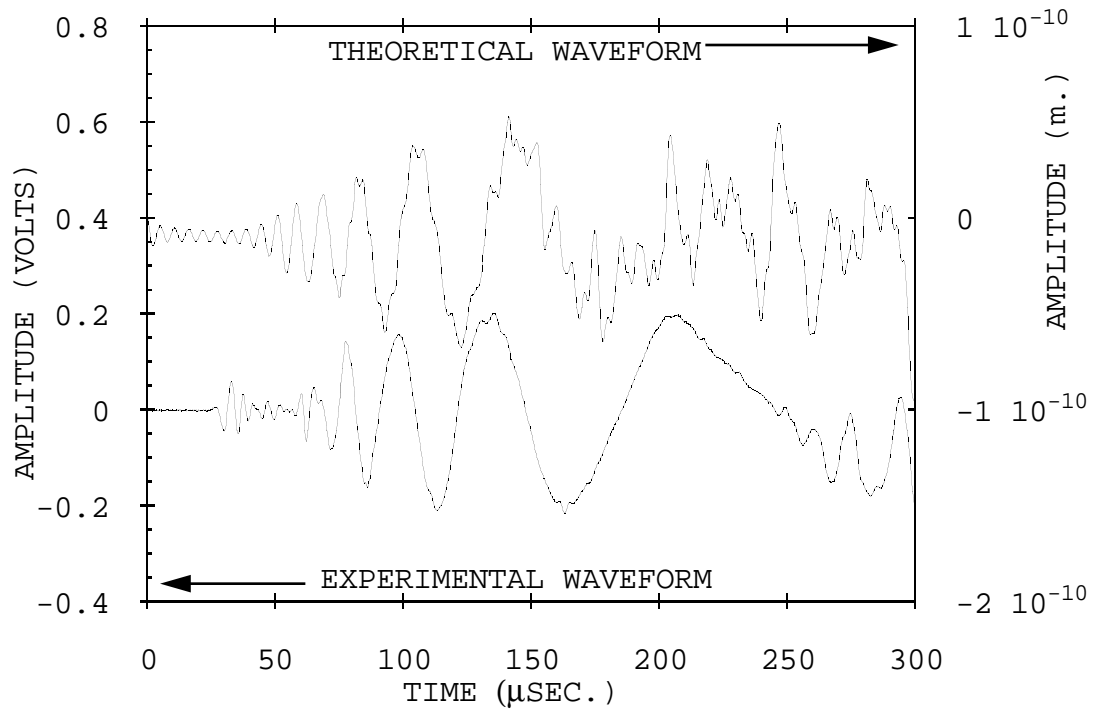
Figure 4.18   Theoretical normal mode and experimental wave-
forms for distance of propagation of 0.127 m.
along the 90 degree direction in $[0_{16}]$ graphite/
epoxy.
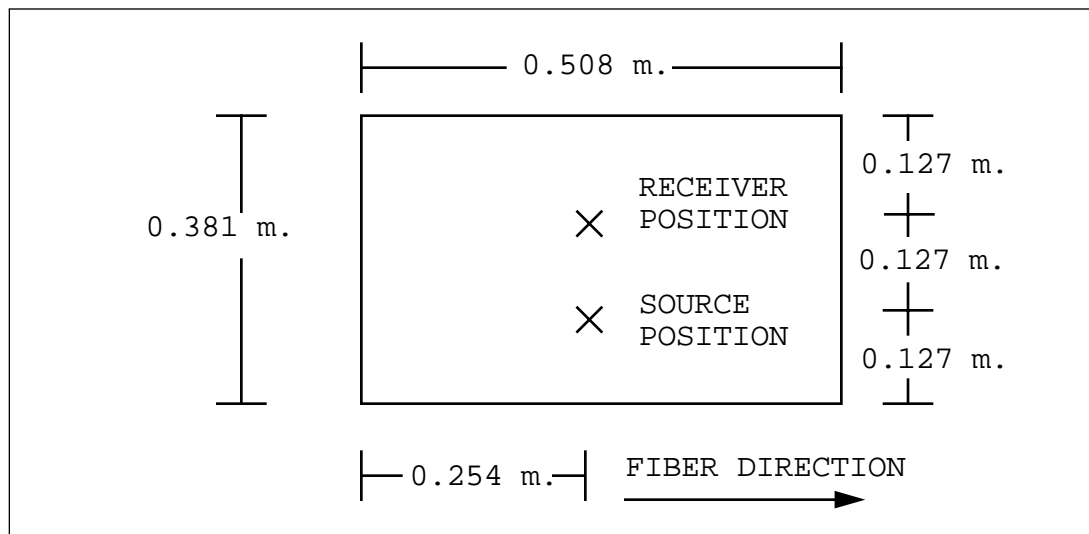
Figure 4.19   Source and receiver positions on $[0_{16}]$ graphite/
epoxy plate for measurement of flexural mode
waveform along 90 degree propagation direction.

mal mode approach treats the finite plate problem, it includes the
effects of the 0 degree properties even for the 90 degree propagation
solution. This further degrades the theoretical solution and is espe-
cially evident in the premature reflections which occur in the theo-
retical waveform.

The theoretical and experimental waveforms for propagation along
the 0 direction in the unidirectional graphite/epoxy plate are
shown in Figure 4.20. In this case, the source position was at the
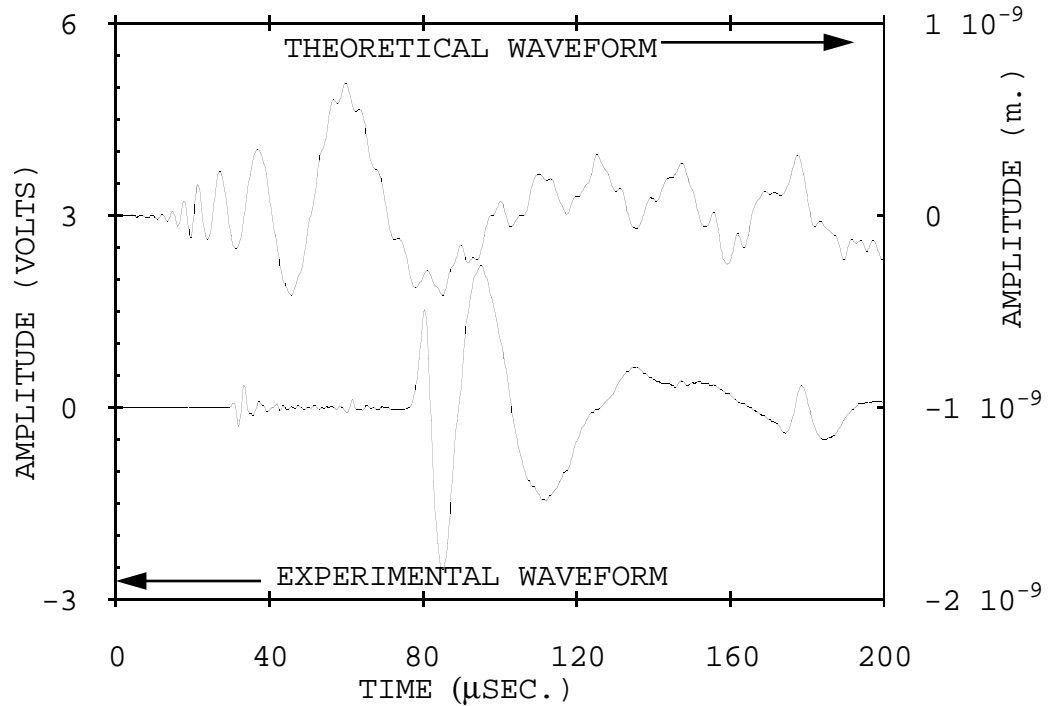
Figure 4.20   Theoretical normal mode and experimental wave-
              forms for distance of propagation of 0.127 m.
              along the 0 degree direction in [0_{16}] graphite/ep-
              oxy.

center width of the plate (0.1905 m.) and at a distance of 0.127 m.
from the edge along the fiber direction. The receiver position was
also at the center width and an additional 0.127 m. from the source
position along the fiber direction as demonstrated in Figure 4.21. As
to be expected from the dispersion measurements along this direction,
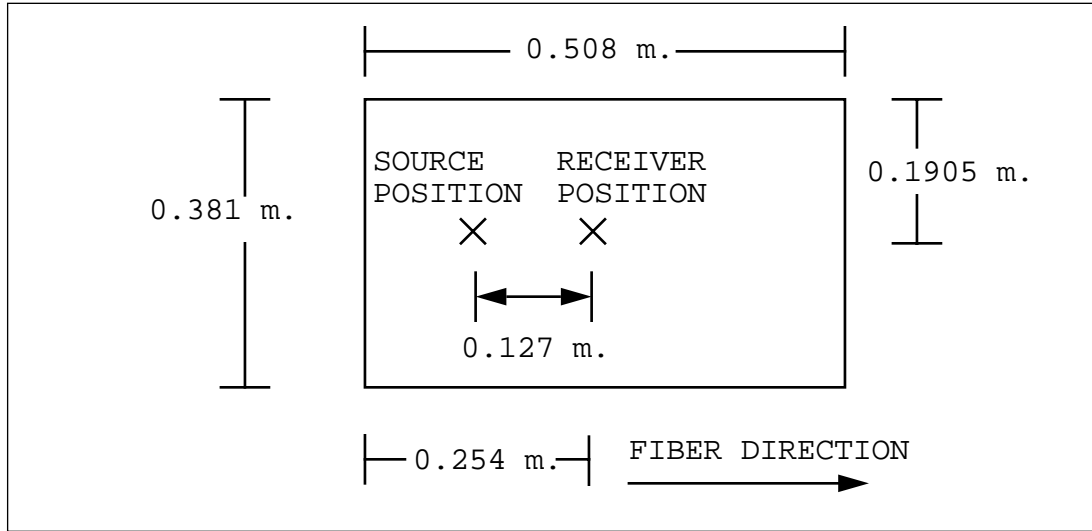
Figure 4.21   Source and receiver positions on $[0_{16}]$ graphite/
epoxy plate for measurement of flexural mode
waveform along 0 degree propagation direction.

the agreement between theory and experiment is nonexistent. This

again shows the limitations of CPT for graphite/epoxy composites.

In summary, the normal mode solution technique has been extended

to the case of a specially orthotropic composite material. This ap-

proach remains valid for these materials. However, the classical

plate theory to which the solution technique was applied is of limit-

ed applicability to gr/ep composites because of the effects of

shear and rotatory inertia which are neglected. This was demonstrated

previously by the dispersion measurements and again is demonstrated

by the lack of agreement particularly in the 0 degree direction.

The next logical step would be to attempt to implement the normal

mode solution technique to the higher order plate theory. This has

been done by Chow [58] for the case of an impulse load. He was inter-

ested in the dynamic response (low frequency vibrations) of composite

plates subjected to impact. The application of the normal mode solu-

tion to the higher order plate theory for the interpretation of

acoustic emission will be investigated in future research.

IV.5 Plate wave propagation in a graphite/epoxy Space Station Freedom (SSF) strut tube.

   In the final experimental section of this work, an investigation of the propagation of simulated AE waves in a medium with a geometry other than a simple flat plate was carried out. The material investigated was again graphite/epoxy composite. However, the geometry was of a long circular cylindrical thin-walled tube. The design and layup of this tube was identical to that to be used in the proposed Space Station Freedom (SSF) and thus is a practical structure of importance and interest. The purpose of this experiment was to determine if AE signals in thin media other than flat plates propagated with plate mode characteristics. Also, the applicability of classical plate theory to predicting the velocity of the modes of propagation was of interest.

   In the experiment, the out-of-plane components of AE signals produced by lead breaks on a graphite/epoxy tube of dimensions and design to be used on SSF were measured using broad band transducers as discussed by Prosser et al. [59]. The signals were shown to consist of plate modes. The amplitudes of the modes were again shown to be affected by source orientation by creating lead breaks on the edge as well as the surface of the tube. Since the specimen being tested is actually a tube geometry, the plate wave predictions are only an approximation. However good agreement might be expected at the frequencies measured since the wavelengths are smaller than the radius of curvature. Measurements of the velocities of both modes were made for propagation along the tube (0 degrees), around the tube

circumference (90 degrees), and at 45 degrees. These velocities

were then compared with velocities predicted from classical plate

theory using stiffness coefficients predicted by laminated plate the-

ory and good agreement was demonstrated.

The tube studied in this research was AS4/976 (Fiberite) graphite/

epoxy with a wall laminate stacking sequence of [+/-10, +/-30, +/-

10]$_s$. The tube had dimensions of 4.5 meters in length, 0.0508 m. in

inner diameter, and 0.0035 m. in wall thickness. The predicted mate-

rial properties for a single lamina of this material obtained from

the manufacturer are shown in Table 4.3. Also given in Table 4.3

SINGLE LAMINA PROPERTIES

Ex (GPa)	Ey(GPa)	Es(GPa)	nx	ny	ρ (Kg/m^3)
147.6	9.65	3.2	0.30	0.02	1560

LAMINATED PLATE PROPERTIES

Laminate thickness h = 3.528x10^{-3} m

In-plane stiffness (MPa-m)

A11	A22	A12	A66
433	44.6	50.8	51.6

Bending stiffness (Pa-m^3)

D11	D22	D12	D66	D16	D26
463	43.9	46.7	47.6	27.9	4.96

Table 4.3   Properties of AS4/976 single lamina and laminat-
             ed plate with layup the same as the tube wall
             layup.

are the predicted properties for a plate with a layup the same as
that of the tube wall.

Pencil lead breaks were used to simulate acoustic emission signals
in the tube. The waves were detected using a 3.5 MHz ultrasonic
transducer while a R15 narrowband sensor was used to trigger the
transient recorder. The detected signals were amplified and
filtered with a preamplifier which had a 20 kHz high pass filter. The
digitized signals were stored on a personal computer for later analy-
sis. A block diagram of the experimental setup is shown in Figure
4.22.
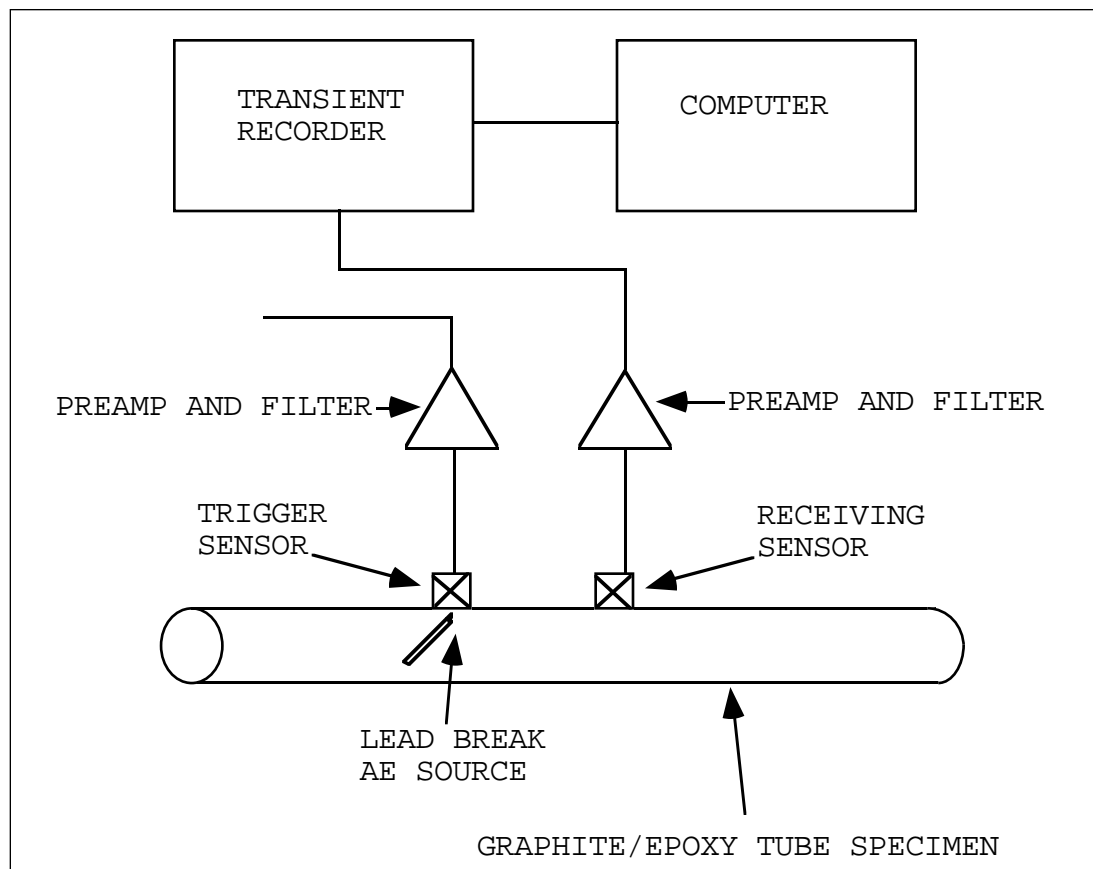
Figure 4.22   Experimental setup for measurements of simulated
             AE waveforms in graphite/epoxy SSF tube.

For measurement of the velocity along a given direction, the transient recorder was triggered by the R15 sensor which was positioned next to the source. The arrival times of the extensional and flexural modes were recorded for a given distance of propagation. The receiving transducer was then moved by a preselected distance along the desired propagation direction and the lead break repeated. Four to six data points were taken for each mode and direction of propagation. The values of arrival time were then plotted against the trigger sensor to receiving sensor separation. A linear least squares fit was applied to the data and the slope was taken to be the velocity.

As in the composite plate measurements, the earliest detected deviation of the wave from zero was used for the arrival time of the extensional wave. Velocity measurements for the flexural mode, however, were more difficult. This was because of multiple paths of propagation for waves which would arrive at the sensor location and interfere with the directly propagating wave of interest. These waves were reflections and waves that propagated around the tube at other angles. This prevented the phase velocity technique used previously on the plates from being used.

A much simpler approach was used to determine the arrival time of a particular frequency component of the flexural mode. The approach was to pick out the half-cycle of the wave which had a half-period which corresponded to the frequency of interest. The arrival time of this half-cycle of wave was chosen to be the center point of the half-period and was designated the arrival time of the frequency of interest. This was accomplished using movable cursors on the personal computer display of the waveform using software (LeCroy Catalyst program) supplied with the digitizer. This is only

an approximation since there are multiple frequency components contained within the half-cycle of wave which was measured. Furthermore, these frequencies are not linearly spaced in arrival time because of the nonlinear dispersion behavior. However, this gives a rough estimate of the arrival time of a frequency component of interest.

Since classical plate theory is applicable only at low frequencies, the flexural measurements were made at the lowest frequency possible. The lowest frequency in the data which was unperturbed by refections was at about 50 kHz. At 50 kHz. in the worst case of the unidirectional composite plate (i.e. the 0 degree propagation direction), the normalized difference between CPT and HOPT was only about 10%. Thus, for a layup with multiple ply angles, CPT should yield agreement to better than 10% at this low frequency. For 50 kHz., the time for the arrival of the portion of the wave with a half cycle time of 10 msec. was used. These arrival times were then used to compute the flexural mode velocity.

The measured and theoretically predicted extensional and flexural velocities for all three directions of propagation are presented in Table 4.4. Good agreement was obtained for both the extensional and flexural velocities with two exceptions. The measured 45 degree extensional velocity was much less than predicted which also occurred in the composite plate measurements. The measured 90 degree flexural velocity was much higher than predicted. Further investigation is needed to explain these discrepancies.

To investigate the effects of source orientation of plate mode amplitudes in the tube, lead breaks were positioned on the surface of the tube and on the end of the tube. Thus the source motion was either normal to the tube surface or in-the-plane of the tube. A wave-

EXTENSIONAL WAVES		
Angle (degrees)	Theoretical c_e (km/s)	Experimental c_e (km/s)
0	8.87	8.89
45	5.97	4.13
90	2.85	3.12

FLEXURAL WAVES	
Angle (degrees)	Theoretical c_f dispersion relation (m/s) (f = frequency in Hz)
0	$7.61 \, (f)^{1/2}$
45	$6.67 \, (f)^{1/2}$
90	$4.22 \, (f)^{1/2}$

Angle (degrees)	Theoretical c_f (km/s at 50 kHz)	Experimental c_f (km/s at 50 kHz)
0	1.70	1.82
45	1.49	1.46
90	0.94	1.41

Table 4.4   Theoretical and experimental plate mode veloci-
ties in graphite/epoxy composite SSF tube.

form due to lead break on the surface of the tube with a source to

receiver distance of 0.1524 m. is presented in Figure 4.23. A compar-

ison with Figure 4.24, which shows a waveform for an identical dis-

tance of propagation but with the lead break on the end of the

tube, demonstrates the effect of source orientation on the amplitudes

of the plate waves. The edge break produces an extensional wave

with a large out-of-plane displacement component. The surface break

also produces a large out-of-plane displacement component, but in the

flexural mode. As discussed previously, this fact may be useful in

obtaining source information for actual sources in composites.
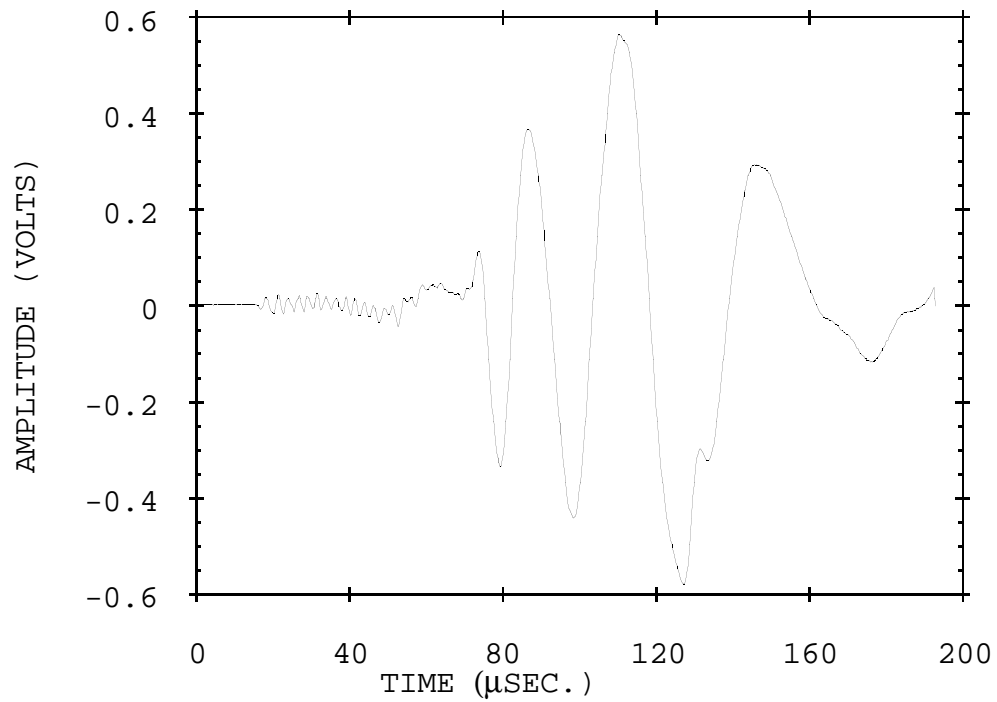
Figure 4.23 AE waveform on SSF graphite/epoxy tube generated
by pencil lead break on surface of the tube with
source to receiver distance of 0.1524 m.
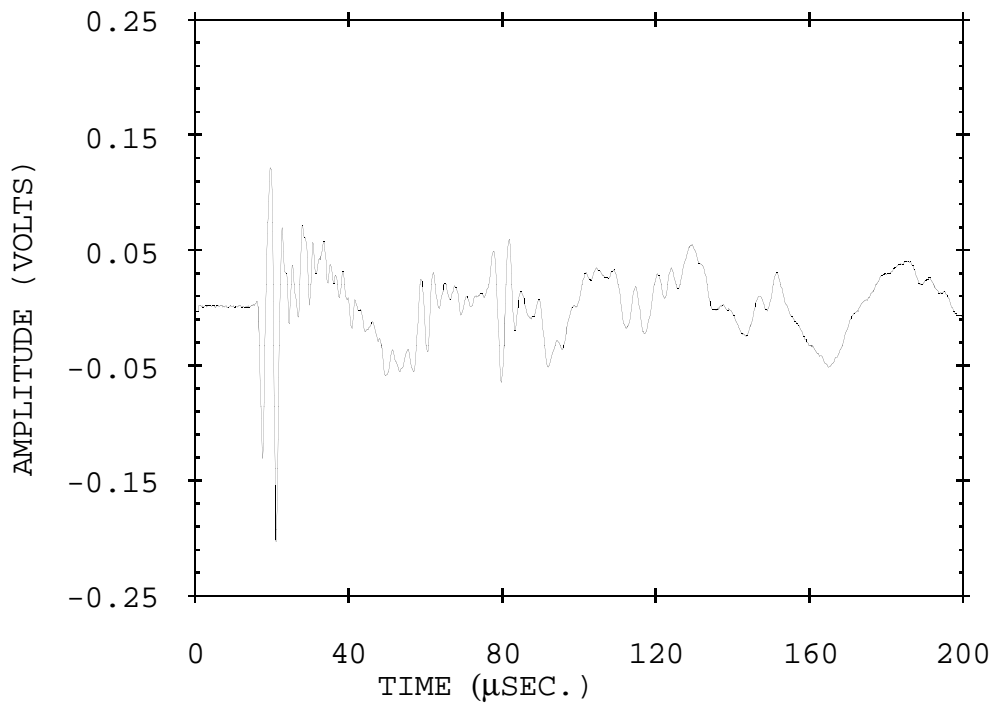
Figure 4.24 AE waveform on SSF graphite/epoxy tube generated
by pencil lead break on end of the tube with
source to receiver distance of 0.1524 m.

In summary, acoustic emission signals from simulated source events in a graphite/epoxy thin-walled composite tube have been captured and analyzed. These waves contained the extensional and flexural modes. The velocities of these modes were measured and compared favorably with predictions based on classical plate theory. The effect of source orientation on the amplitudes of the two modes was documented for sources normal to the tube and in-the-plane of the tube. As before, the normal source created a wave with a larger flexural mode amplitude while the in-plane source created one with a larger extensional mode amplitude. This work demonstrates that AE signals propagate in practical thin-walled structures of interest with plate mode characteristics. Additionally, it demonstrates that classical plate theory is useful in some cases where the geometry is not that of a simple flat plate.

V. Summary and Conclusions

The propagation characteristics of the plate modes of acoustic emission waves in thin aluminum plates and thin graphite/epoxy composite plates and tubes have been studied in this research. Prior to these measurements, however, the effects of the transducer on the measurement of these waves were considered. This was necessary so that transducer artifacts could be accounted for when comparing measured waveforms with theoretical predictions.

Evaluation of the transducer response was accomplished by three techniques. In each technique, the response of the broad band ultrasonic transducer (Panametrics 3.5 MHz) used in the plate wave measurements was compared to those from three other conventional piezoelectric AE sensors. The three sensors were a 150 kHz resonant sensor (Physical Acoustics Corporation model R15), a conventional broad band AE sensor (Physical Acoustics Corporation model S9208), and a broad band, small area, velocity sensitive pinducer (Valpey-Fisher). The first evaluation technique consisted of comparing the output responses of the sensors when they were stimulated by another transducer which was driven with a swept sine tone burst over the frequency range of interest. The second technique compared their responses when the input was a simulated AE signal generated by a pencil lead break (Hsu-Neilsen) source on a thick aluminum plate. In this case, the responses were also compared with theoretical predictions. The final method compared the responses when the input source was again a simulated AE signal generated by a lead break which in this case propagated to the sensor in a thin aluminum plate. The output of a displacement sensitive optical interferometer was used for comparison in the third evaluation method.

In all three methods, the ultrasonic transducer proved to be the best for quantitative measurements of AE waveforms because of its flatter frequency response characteristics. This means that it yielded a higher fidelity reproduction of the actual signal that it was attempting to measure. The peak sensitivity of this sensor was not as great as that of the resonant sensor, but it compared favorably with the other two broad band transducers. Comparison with an optical interferometer demonstrated that the output of the ultrasonic transducer was proportional to the normal surface displacement. Although the frequency response curve generated by the swept sine input technique was not useful for absolute calibration in terms of meters of displacement per volt of transducer output, it was used to remove the transducer frequency response allowing relative comparisons of theoretical waveforms with experimental predictions.

Two experiments on the propagation of plate modes in aluminum plates were carried out. These were measurements of the effect of source orientation on the amplitudes of the two plate modes and the comparison of theoretically predicted flexural mode waveforms with experimental measurements. In the first experiment, the in-plane and the out-of-plane displacement amplitudes of the extensional and flexural modes were measured for lead break simulated AE sources with varying orientations. The lead was broken normal to the surface of the plate (90 degrees), normal to the edge of the plate (0 degrees), and at angles of 30 and 60 degees. The later two source angles were accomplished using specially machined slots in the plate. Measurements of the waveforms at equal distances of propagation demonstrated that the amplitudes of the two plate modes were dependent on the source orientation. As the out-of-plane component of the

source motion decreased from its peak when the source was at 90 degrees to its minimum when the source was at 0 degrees, the flexural amplitudes of the waveforms decreased. Simultaneously, the extensional wave amplitude increased since the in-plane component of source motion was increasing as the source motion moved toward 0 degrees. These measurements may be a first step toward the solution of an important problem in AE testing, that is, the problem of determining the source type and orientation from measured AE waveforms.

The second experiment in the thin aluminum plates compared experimentally measured flexural mode waves with theoretical predictions for a finite plate based on a normal mode expansion solution technique for classical plate theory. The experimental waveforms were again generated by pencil lead breaks to simulate an AE source. Agreement between theory and experiment was excellent over the lower frequency regime for which classical plate theory is valid. One advantage of this solution technique is that it can handle the case of a finite plate which has never been solved by previous solutions of exact elasticity theory. Additionally, it is computationally much less intensive than solutions to the exact theory for propagation in an infinite plate and it is easily extended to include the anisotropy of composite materials. The importance of this research is that the propagation of an AE waveform from a known source must be well understood before the more difficult problem of determining the source characteristics of an unknown source based on the measured waves can be handled.

Numerous experiments were carried out to investigate the propagation of plate modes in anisotropic laminates of graphite/epoxy. The velocity of the extensional mode along the 0, 45, and 90 degree prop-

agation directions was measured in four plates, each having different ply layups. The measured velocities were compared with those predicted by classical plate theory. In general, the measured velocities were slightly lower than those predicted from theory. A possible explanation for this was that the elastic properties used in the calculations which were obtained from the manufacturer were larger than those of the actual material. Variation in the elastic properties caused by variations in the resin chemistry, cure cycle conditions, and fiber volume are common for this material.

The flexural velocity was also measured along the same three directions of propagation in these laminates. However, because of the dispersive nature of this mode, it was measured over a range of frequencies with a differential phase technique. These measurements were also compared with predictions based on classical plate theory. Lack of agreement was exhibited even at low frequencies and this was demonstrated to be caused by the effects of shear and rotatory inertia which are neglected by classical plate theory. These effects are much more significant in materials such as graphite/epoxy composites where the shear modulus is much smaller than the Young's modulus.

A higher order plate theory was described which takes these effects into account. Much better agreement was obtained between the measured flexural dispersion and that predicted by HOPT. Again, however, the measured values were consistently less than those predicted by HOPT using elastic properties obtained from the manufacturer. This is consistent with the extensional measurements and the theory that the properties used in the calculations were higher than those of the actual material. It may be possible to make additional measurements

at other angles of propagation and invert them to determine the actu-
al elastic properties of the material. Since the actual properties of
the material are critical for engineers in applications of this mate-
rial, this nondestructive method of determining them is of great im-
portance and will be investigated in the future.

The normal mode solution technique of classical plate theory for
the specially orthotropic composite material was presented. Experi-
mental measurements of the flexural mode waveform were compared
with theoretical predictions for the 0 and 90 degree directions of
propagation in the unidirectional laminate. The lack of agreement for
this particular case was expected because of the limitations of
CPT, especially for propagation along the 0 degree direction. In this
direction, the ratio of the shear modulus to the Young's modulus is
at its minimum for this material. Better agreement might be
obtained by extending the normal mode solution to the HOPT. It was
pointed out that this has been done previously for the case of impact
loading of a composite plate. The application to the step function
loading problem for AE propagation is another area to be investigated
in the future. This research is an important component in providing a
better understanding of the problem of AE signal interpretation and
will help in the effort to extract information about real AE sources.

The final experimental investigations were of AE waveforms propa-
gating in a thin-walled graphite/epoxy tube. This tube was of the
proposed design to be used on the strut elements of the proposed
Space Station Freedom. Because of the thin-walled nature of this
structure, the AE signals propagated as plate modes even though the
geometry was not that of a simple flat plate. Thus, the understanding
of these modes of propagation is important for the monitoring of AE

in important practical structures. The extensional and flexural velocities were again measured and shown to compare favorably with theory. The effect of source orientation was also demonstrated for sources normal to the tube surface and normal to the end of the tube.

In summary, a detailed study of the propagation of plate waves in AE signals has been carried out. This is of great importance due to the thin-walled nature of many practical structures of interest such as the SSF tube. Other examples include the external skins of air and space craft and pressure vessel walls. In order to obtain quantitative information about the sources of emission in these structures from measured AE waves, the propagation of these modes must be well understood and characterized.

Several important future research directions became apparent during the course of this research and are pointed out here. The first is to investigate further the cases where anomalous measurements were present or where theory and experiment were not in agreement in this work. These cases include the unexpected behavior of the flexural mode amplitudes for the source orientations of 60 and 90 degrees in the aluminum plates. Also, the extensional velocity in the 45 degree direction of propagation in the unidirectional plate which was much lower than predicted needs further study.

Another research direction is the applicability of plate wave measurements for the characterization of material properties. This is especially important for composite materials where there can be significant variations from sample to sample. The applicability to AE of the normal mode solution technique to higher order plate theory for composite materials also needs investigation. Another area of great importance is the study of source orientation effects on the plate

mode amplitudes for real sources of emission such as matrix cracking, fiber breakage, and delamination in composites. Finally, a research area that should be studied is the application of the knowledge of plate mode AE propagation toward more accurate AE source location, again, especially in composites.

References

[1]   R. G. Liptai, D. O. Harris, R. B. Engle, and C. A. Tatro, "Acoustic Emission Techniques in Materials Research," *International Journal of Nondestructive Testing*, **3** (1971) pp. 215-275.

[2]   R. E. Green, Jr., Treatise on Materials Science and Technology, Volume 3: Ultrasonic Investigation of Mechanical Properties, (Academic Press, New York, 1973) p. 1.

[3]   B. A. Auld, Acoustic Fields and Waves in Solids, Volume II, (Robert E. Drieger Publishing Co., Malabar, Florida, 1990) p. 2.

[4]   A. T. Green, C. S. Lockman, and R. K. Steele, "Acoustic Verification of Structural Integrity of Polaris Chambers," *Modern Plastics*, **41** (1964) p. 137.

[5]   E. Votava and P. Jax, "Inspection of Nuclear Reactors by Means of Acoustic Emission During Hydrostatic Test," *Acoustic Emission Monitoring of Pressurized Systems, ASTM STP 697* (1979) pp. 149-164.

[6]   C. Le Floc'h, "Acoustic Emission Monitoring of Composite High-Pressure Fluid Storage Tanks," *NDT International*, **19** (1986) pp. 259-262.

[7]   P. G. Bentley, D. G. Dawson, and D. W. Prine, "An Evaluation of Acoustic Emission for the Detection of Defects Produced During Fusion Welding of Mild and Stainless Steels," *NDT International*, **15** (1982) p. 243.

[8]   M. S. Lan and D. A. J. Dornfeld, "In-Process Tool Fracture Detection," *Journal of Engineering Materials and Technology*, **106** (1984) p. 111-118.

[9]   J. C. Spanner, *Advances in Acoustic Emission*, (Dunhart, USA, 1981).

[10]   T. J. Fowler and E. Gray, "Development of an Acoustic Emission Test for FRP Equipment," Preprint 3583, Presented at the American Society for Civil Engineers Convention, Boston, MA (April 2-6, 1979).

[11]   M. A. Hamstad, "A Review: Acoustic Emission, a Tool for Composite-Materials Studies," *Experimental Mechanics*, **26** (1986) pp. 7-13.

[12] R. Hill and S. M. A. El-Dardiry, "The Effect of Geometry on Acoustic Emission," *in Proceedings of the Institute, Fundamental Aspects and Application of Acoustic Emission*, (London: Chelsea College, 1976).

[13] D. G. Eitzen, F. R. Breckenridge, R. B. Clough, E. R. Fuller, N. N. Hsu, and J. A. Simmons, "Fundamental Developments for Quantitative Acoustic Emission Measurements," Interim Report for Electric Power Research Institute NP-2089 (1981).

[14] F. R. Breckenridge, C. E. Tschieff, and M. Greenspan, "Acoustic Emissions: Some Applications of Lamb's Problem," *J. Acoust. Soc. Am.*, **57** (1975) pp. 626-631.

[15] H. Lamb, "On the Propagation of Tremors over the Surface of an Elastic Solid," *Phil Trans. R. Soc.*, **A203** (1904) pp. 1-42.

[16] C. L. Pekeris, "The Seismic Surface Pulse," *Proc. Nat. Acad. Sci.*, **41** (1955) pp. 469-480.

[17] T. M. Proctor Jr., "An Improved Piezoelectric Acoustic Emission Transducer," *J. Acoust. Soc. Am.*, **71** (1982) pp. 1163-1168.

[18] T. M. Proctor Jr., "A High Fidelity Piezoelectric Tangential Displacement Transducer for Acoustic Emission," Journal of Acoustic Emission, 7 (1988) pp. 41-47.

[19] Y. H. Pao, R. R. Gajewski, and A. N. Ceranoglu, "Acoustic Emission and Transient Waves in an Elastic Plate," *J. Acoust. Soc. Am.*, **65** (1979) pp. 96-105.

[20] N. N. Hsu, "Dynamic Green's Functions of an Infinite Plate - A Computer Program," *NBSIR 85-3234*, (1985).

[21] Y. Fukunaga and T. Kishi, "Dynamic Green's Function of Finite Media by Finite Difference Method," *Progress in Acoustic Emission III, The Japanese Society of NDI*, (1986) pp. 722-731.

[22] C. B. Scruby, G. R. Baldwin, and K. A. Stacey, "Characterization of Fatigue Crack Extension by Quantitative Acoustic Emission," *International Journal of Fracture*, **28** (1985) pp. 201-222.

[23] K. Y. Kim and W. Sachse, "Characteristics of an Acoustic Emission Source from a Thermal Crack in Glass," *International Journal of Fracture*, **31** (1986) pp. 211-231.

[24] M. Enoki and T. Kishi, "Theory and Analysis of Deformation Moment Tensor Due to Microcracking," *International Journal of Fracture*, **38** (1988) pp. 295-310.

[25] M. Ohtsu and K. Ono, "AE Source Location and Orientation Determination of Tensile Cracks from Surface Observation," *NDT International*, **21** (1988) PP. 143-150.

[26] H. N. G. Wadley and C. B. Scruby, "Elastic Wave Radiation from Cleavage Crack Extension," *International Journal of Fracture*, **21** (1983) pp. 111-128.

[27] C. P. Hsiao, "The propagation of Acoustic Emission Signals in Polymeric Media," Ph.D. Thesis, University of Oklahoma, Norman Oklahoma 1988.

[28] Z. Yu and P. C. Clapp, "Quantitative Analysis of Acoustic Emission Signals," *J. Appl. Phys*., **62** (1987) pp. 2212-2220.

[29] H. Lamb, "On Waves in an Elastic Plate," *Proc. R. Soc.*, **A93** (1917) pp. 114-128.

[30] J. W. S. Rayleigh, The Theory of Sound, Volumes I and II, (Dover Publications, New York, 1945).

[31] K. F. Graff, Wave Motion in Elastic Solids, (Universities Press, Belfast, 1975).

[32] A. A. Pollock, "Classical Wave Theory in Practical AE Testing, *Progress in Acoustic Emission III, The Japanese Society of NDI*, (1986) pp. 708-721.

[33] F. Press and J. Oliver, "Model Study of Air-Coupled Surface Waves," *J. Acoust. Soc. Am.*, **27** (1955) pp. 43-46.

[34] M. A. Medick, "On Classical Plate Theory and Wave Propagation," *J. Appl. Mech.*, **28** (1961) pp. 223-228.

[35] M. R. Gorman, "Plate Wave Acoustic Emission," *J. Acoust. Soc. Am.*, **90(1)** (1990) pp. 358-364.

[36] M. R. Gorman and S. M. Ziola, "Plate Waves Produced by Transverse Matrix Cracking," *Ultrasonics*, **29** (1991) pp. 245-251.

[37] M. R. Gorman, private communication, (1991).

[38] H. Dunegan, "Acoustic Emission, Past, Present and Future", panel discussion at the Fourth World Meeting of the Acoustic Emission Working Group, Boston, (1991).

[39] Y. H. Pao and R. R. Gajewski, "The Generalized Ray Theory and Transient Response of Layered Elastic Solids," in Physical Acoustics, Principles and Methods, Volume XIII, Editors W. P. Mason and R. N. Thurston, (Academic Press, New York, 1977) pp. 183-265.

[40] Y. H. Pao, "Theory of Acoustic Emission," in Elastic Waves and Nondestructive Testing, AMD-29, Am. Soc. Mech. Engr., (New York, 1978) pp. 107-128.

[41] S. Majerowicz, "The Influence of Specimen Geometry on Acoustic Emission Signal Propagation," Masters Essay, Johns Hopkins University, (1983).

[42] J. B. Spicer, J. W. Wagner, and J. B. Deaton, Jr., private communication, (1990).

[43] R. J. Dewhurst, C. E. Edwards, A. D. W. McKie, and S. B. Palmer, "Comparative Study of Wide-Band Ultrasonic Transducers," *Ultrasonics*, **25** (1987) pp. 315-321.

[44] M. R. Gorman and W. H. Prosser, "AE Source Orientation by Plate Wave Analysis," *Journal of Acoustic Emission*, In press, (1991).

[45] M. R. Gorman and W. H. Prosser, "Application of Normal Mode Expansion to AE Waves in Finite Plates," Submitted to *Transactions of the ASME: Journal of Applied Mechanics*, (1990).

[46] J. W. Whitney, Structural Analysis of Laminated Anisotropic Plates, (Technomic Publishing Co., Lancaster, Pennsylvania, 1987).

[47] S. W. Tsai and H. T. Hahn, Introduction to Composite Materials, (Technomic Publishing Co., Lancaster, Pennsylvania, 1980).

[48] B. Tang, E. G. Henneke II, and R. C. Stiffler, "Low Frequency Flexural Wave Propagation in Laminated Composite Plates," *Proceedings on a Workshop on Acousto-Ultrasonics: Theory and Applications*, Blacksburg Virginia, (1987) pp. 45-65.

[49] P. C. Yang, C. H. Norris, and Y. Stavsky, "Elastic Wave Propagation in Heterogeneous Plates, *International Journal of Solids and Structures*, **2** (1966) pp. 665-684.

[50] R. D. Mindlin, "Influence of Rotatory Inertia and Shear on Flexural Motions of Isotropic, Elastic Plates," *Journal of Applied Mechanics*, **2** (1951) pp. 31-38.

[51] D. Chairns, private communication, (1990).

[52] W. H. Prosser, "Ultrasonic Characterization of the Nonlinear Elastic Properties of Unidirectional Graphite/Epoxy Composites," NASA Contractor Report 4100, (1987).

[53] W. Sachse and Y. H. Pao, "On the Determination of Phase and Group Velocities of Dispersive Waves in Solids," *J. Appl. Phys.*, **49(8)** (1978) pp. 4320-4327.

[54] Y. H. Pao and W. Sachse, "Ultrasonic Phase Spectroscopy and the Dispersion of Elastic Waves in Solids," *Proceedings of the Ninth International Congress on Acoustics*, Madrid Spain, (1977) p. 734.

[55] M. Veidt and M. Sayir, "Experimental Evaluation of Global Composite Laminate Stiffnesses by Structural Wave Propagation," *Journal of Composite Materials*, **24** (1990) pp. 688-706.

[56] G. D. Dean, "The Use of Plate Bending Waves for Elastic Property Determination of Polymers," National Physical Laboratory Report DMA(A)166, (Teddington, Middlesex, UK, 1988).

[57] D. Alleyne and P. Cawley, "A Two-Dimensional Fourier Transform Method for the Measurement of Propagating Multimode Signals," *J. Acoust. Soc. Am.*, **89(3)** (1991) pp. 1159-1168.

[58] T. S. Chow, "On the Propagation of Flexural Waves in an Orthotropic Laminated Plate and Its Response to an Impulsive Load," *Journal of Composite Materials*, **5** (1971) pp. 306-319.

[59] W. H. Prosser, M. R. Gorman, and J. Dorighi, "Extensional and Flexural Waves in a Thin-Walled Graphite/Epoxy Tube" *Journal of Composite Materials*, In press.

Vita

The author was born in Milledgeville, GA on September 14, 1962. He graduated from Georgia Military College (High School Division) in Milledgeville, GA, in 1980. In May, 1984 he received the Bachelor of Science degree from the College of William and Mary in Virginia after satisfying the degree requirements of both the Department of Mathematics and the Department of Physics, graduating with Departmental Honors in Physics. He received a NASA NDE Fellowship to attend graduate school in the Department of Materials Science and Engineering at the Johns Hopkins University where he received the Master of Science in Engineering degree in May, 1987. Since that time, he has been employed full time at the NASA Langley Research Center in the Nondestructive Evaluation Sciences Branch where this research was performed as a nonresident graduate student of Johns Hopkins. He is a student member of the Acoustical Society of America and the American Society for Composites.